UNIVERSITY OF CALIFORNIA,
IRVINE

Nanoscale Biosensing: Fabrication and Characterization of Electrochemically Deposited Nanostructured Arrays and Single Nanoparticle Surface Plasmon Resonance Microscopy

DISSERTATION

submitted in partial satisfaction of the requirements
for the degree of

DOCTOR OF PHILOSOPHY

in Chemistry

by

Kyunghee Cho

Dissertation Committee:
Professor Robert M. Corn, Chair
Professor Reginald M. Penner
Professor A. J. Shaka

2015

DEDICATION

To my mother and father.

TABLE OF CONTENTS

LIST OF FIGURES

LIST OF TABLES

LIST OF SYMBOLS

θ: Angle from normal incidence at which the photoresist was exposed through the nanohole film for lithography.

φ: Polarization of light used for FT-NIR measurement; $\varphi = 0°$ indicates that the light was polarized perpendicular to the openings in the split nanorings.

$\Delta\%R_{NP}$: The single nanoparticle surface plasmon resonance microscope reflectivity change.

ACKNOWLEDGMENTS

My graduate school journey has certainly not been easy, and I am grateful for the many people who helped me to not only get through it, but made it one filled with tremendous growth both academically and personally.

I am extremely fortunate to have had Professor Robert Corn as my graduate research advisor. Rob, thank you for your guidance, patience, discussions, and encouragement over the past five years. Thank you for providing your students the freedom and generous support to pursue our own passions and projects, even if that means having to learn through failures. I am also grateful for the many culinary adventures over the years; I think I can say finally after five years of being in the Corn Research Group that I appreciate good Chinese food, pho, and wine, and I have you to thank for it.

I would also like to thank the other members of my Ph.D. committee, Professor Reg Penner and Professor A.J. Shaka, for their support and encouragement. I am grateful to the many professors from UCI's chemistry and physics departments who taught the too many to count ChaMP courses for helping me to become a more well-rounded scientist. I am appreciative of the world-class facilities available to UCI researchers, especially the Laboratory for Electron and X-ray Instrumentation (LEXI) where all of the SEM and XRD data presented here were obtained. I thank Dr. Jian-Guo Zheng and Dr. Qiyin Lin for training me to use so many of LEXI's cool instruments.

The work presented in this dissertation would not have been possible without the many past and present members of the Corn Research Group. I must especially thank Dr. Aaron Halpern, whose contributions to the group laid the foundation for much of the work presented here. I thank him showing me the ropes around the Corn lab and UCI and for his generosity and

friendship. I am also grateful to Dr. Megan Szyndler for her encouragement and support over the years, even after she moved to the other side of the country. I will always fondly remember the 10 PM Taco Bell/In-N-Out runs. I am thankful to have worked with Jennifer Fasoli, who has read and edited way too many of my manuscripts and is reading the introduction of this dissertation as I type this out. I will miss her company, our lunches, and the Starbucks/MJ's/302 runs. I am also lucky to have worked with many other great past and present graduate students in the Corn Group who have all been friendly and supportive and helped make the lab run smoothly every day. I have been fortunate to have worked with and learned from several fantastic post-doctoral researchers while at UCI, specifically Dr. Gabriel Loget, Dr. Mana Toma, and Dr. (soon to be Professor) Keiichi Yoshimatsu. This dissertation would not have been possible without their knowledge, contributions, and support.

I must thank my family and relatives who have encouraged and supported me my entire life. My parents inspire me every day and I thank them for their unconditional love. I would like to especially thank Aunt Cho Wilson for always having my back.

Graduate school takes a good amount of perseverance, and, without my support network of brother, aunts, uncles, cousins, roommates, and friends from UCI, UCLA, and Ventura, successfully finishing this journey would have been difficult.

Finally, I am extremely thankful to my soon to be wife Jean Bak, the best lawyer in town. Thank you for your patience and support. Olive juice.

The work presented in this dissertation was made possible by funding from the National Institutes of Health (through grant R01-GM059622) and the National Science Foundation (through grant CHE-1057638).

CURRICULUM VITAE

Kyunghee (Mike) Cho
mrmikecho@gmail.com

Education

Ph.D., Chemistry, University of California, Irvine (Irvine, CA), 2015
Concentration: Chemical and Materials Physics
Dissertation: Nanoscale Biosensing: Fabrication and Characterization of Electrochemically Deposited Nanostructured Arrays and Single Nanoparticle Surface Plasmon Resonance Microscopy
Advisor: Professor Robert Corn

M.S., Chemistry, University of California, Irvine (Irvine, CA), 2014
Concentration: Chemical and Materials Physics
Thesis: Lithographically Patterned Nanoscale Electrodeposition of Plasmonic Split Nanoring Arrays for the Fabrication of Near Infrared Dichroic Polarizing Filters
Advisor: Professor Robert Corn

B.S., Chemistry, University of California, Los Angeles (Los Angeles, CA), 2005
Minor: English

Professional Experience

Gradute Student Researcher, 2009 – 2014
University of California, Irvine (Irvine, CA)

Teaching Assistant, 2009 – 2011
University of California, Irvine (Irvine, CA)

Lead Associate Scientist, 2006 – 2009
ZPower, LLC (Camarillo, CA)

AmeriCorps Mentor, 2001 – 2003
UCLA BruinCorps (Los Angeles, CA)

Publications and Patents

1. Cho, K., Wood, J.B., Yoshimatsu, K., Shea, K. J., Corn, R.M. Measuring Melittin Uptake in Single Hydrogel Nanoparticles with Near Infrared Surface Plasmon Resonance Microscopy, *submitted for publication*.
2. Cho, K., Loget, G., Corn, R.M. Lithographically Patterned Nanoscale Electrodeposition of Plasmonic, Bimetallic, Semiconductor, Magnetic, and Polymer Nanoring Arrays, *J. Phys. Chem. C*, **2014**, *118*, 28993-29000.
3. Toma, M., Cho, K., Wood, J.B., Corn, R.M. Gold Nanoring Arrays for Near Infrared Plasmonic Biosensing, *Plasmonics*, **2014**, *9*, 765-772.
4. Loget, G., Wood, J.B., Cho, K., Halpern, A.R., Corn, R.M. Electrochemical Deposition of Polydopamine Thin Films and Nanostructured Surfaces for DNA Microarrays and Surface Patterning, *Anal. Chem.*, **2013**, *85*, 9991-9995.
5. Wood, J.B., Szyndler, M.W., Halpern, A.R., Cho, K., Corn, R.M. Fabrication of DNA Microarrays on Polydopamine-Modified Gold Thin Films for SPR Imaging Measurements, *Langmuir*, **2013**, *29*, 10868-10873.
6. Wang, Y., Liu, X., Halpern, A.R., Cho, K., Corn, R.M., Potma, E.O. Wide-field, Surface-Sensitive Four-Wave Mixing Microscopy of Nanostructures, *Appl. Opt.*, **2012**, *51*, 3305-3312.
7. Adamson, G., Zhou, H., Cho, K. 2015. Cathode Active Material (Higher Oxides of Silver). Publication No. US8936775 B2, filed Oct 29, 2009 and granted Jan 20, 2015.

Presentations

1. August 2014, Single Nanoparticle Surface Plasmon Resonance Microscopy of DNA Hybridization Adsorption and Surface Polymerization. Talk given at the ACS National Meeting in San Francisco, CA.
2. September 2013, Plasmonic Nanorings for Biosensing and Materials Applications. Talk given at the SciX Conference in Milwaukee, WI.

Professional Affliations

American Chemical Society
Southern California Society for Microscopy and Microanalysis

ABSTRACT OF THE DISSERTATION

Nanoscale Biosensing: Fabrication and Characterization of Electrochemically Deposited Nanostructured Arrays and Single Nanoparticle Surface Plasmon Resonance Microscopy

By

Kyunghee Cho

Doctor of Philosophy in Chemistry

University of California, Irvine, 2015

Professor Robert Corn, Chair

The work presented in this dissertation covers two types of nanomaterials (nanostructured arrays on surfaces and nanoparticle suspensions) with a unified focus on biosensing applications utilizing surface plasmon resonance (SPR), a surface sensitive phenomenon that occurs at the nanoscale. The first part of the dissertation describes the fabrication of lithographically patterned and electrochemically deposited large-scale arrays of nanorings and split nanorings. The fabrication and characterization of nanoring arrays made from a host of materials such as Ni, Au, Co, and polydopamine are discussed. Additionally, the fabrication of split nanoring arrays with potential applications as a tunable dichroic is explained. The application of plasmonic gold nanoring arrays as a biosensor to detect DNA hybridization with detection capabilities down to 50 pM of DNA follows. The next part of this dissertation shifts focus from nanostructured surfaces to the detection of nanoparticles in suspension using surface plasmon resonance microscopy (SPRM). Specifically, polymeric hydrogel nanoparticles that have been engineered to bind the hexacosa peptide melittin is studied. Point diffraction patterns in sequential real-time SPRM differential reflectivity images are counted to create digital adsorption binding curves of single 220 nm diameter hydrogel nanoparticles from picomolar nanoparticle solutions onto

alkanethiol-modified gold surfaces. The SPRM responses from the adsorption of hundreds of individual hydrogel nanoparticles are quantified to measure the loading of melittin, a potential therapeutic compound, into the nanoparticles. Additional bulk fluorescence measurements of melittin uptake into the hydrogel nanoparticles are used to correlate the maximum signal observed by SPRM to the incorporation of approximately 65,000 molecules into each 220 nm hydrogel nanoparticle, corresponding to roughly 4% of its volume.

Chapter 1

Introduction

1.1 Dissertation Overview

Nanomaterials have become ubiquitous in the modern world, yet they still offer the promise of great advancements in fields as diverse as healthcare and renewable energy.[1,2] In biotechnology and, more specifically, biosensing, the use of nanomaterials have become important in the development of ultrasensitive sensor platforms and signal amplification.[1,3] One area of tremendous growth in recent years has been biosensing technologies based on surface plasmon resonance (SPR), a surface sensitive phenomenon that occurs at the nanoscale.[4,5] One of the most notable advantages of SPR-based biosensing over other biosensing methods such as those based on fluorescence is that it is label-free; thus, SPR-based techniques are not subject to such problems as fluorescent labeling and photobleaching. However, fluorescence-based biosensing offers sensitivity down to single molecule detection,[6,7] which is a level of detection that requires a great deal of research to develop with SPR based methods.

The development and characterization of nanoscale materials for biosensing encompass the three main sections of this dissertation: (1) First, the fabrication and characterization of a variety of nanoring arrays on glass substrates is described. (2) Next, the use of gold nanoring arrays as a plasmonic biosensor is demonstrated. (3) The last part of the dissertation shifts focus from nanostructured surfaces to the measurement of therapeutics-loading into hydrogel nanoparticles in suspension by surface plasmon resonance microscopy.

1.2 Nanoring and Split Nanoring Arrays

Nanoring arrays have been an area of particular interest in nanomaterials development. In biosensing, the strong localized surface plasmon resonance (LSPR) arising from nanoring arrays fabricated with plasmonic materials have been utilized for refractive index based sensing.[8,9] Beyond biosensing, magnetic nanoring arrays have been explored as a potential material for use as high capacity random access memory devices due to their well-defined magnetic states.[10,11] Additionally, split nanoring arrays have been explored as an optical metamaterial with potentially unique and important properties in the development of negative refractive index materials and perfect lenses.[12]

While nanoring arrays have interesting properties with potential uses in a variety of fields, their fabrication costs can be prohibitive. Electron-beam lithography (EBL), a common technique in nanoscale material fabrication, can consume hours of beam time for an array fabrication. An alternative to EBL is a technique developed at the University of California, Irvine for the production of large (cm^2 scale) arrays of parallel nanowires called lithographically patterned nanowire electrodeposition (LPNE).[13] As its name indicates, LPNE involves a number of fabrication steps involving photolithography and electrochemical deposition. First, a thin

sacrificial film is thermally evaporated onto the substrate; the thickness of this film controls the final thickness of the nanowires created. Next, a layer of photoresist is spin-coated and patterned on the sacrificial layer; the photomask pattern determines the nanowire spacing and orientation. In the next step, the exposed part of the sacrificial film is chemically etched away, leaving trenches under the photoresist. The nanowires are then electrodeposited onto the side-walls that have been created in the sacrificial layer (underneath the photoresist); the choice of the electrodeposited material determines the makeup of the nanowires. Lastly, the photoresist and remaining sacrificial layer are removed. The beauty of LPNE is that it allows for the tuning of many different parameters (various nanoscale dimensions and choice of material) while also being relatively fast and cost-efficient. The versatility of LPNE nanowires has been demonstrated in their use as gas sensors, biosensors, thermophones, field-effect transistors, and more.[14-17] The work discussed in the next two chapters of this dissertation adapts this strategy to fabricate densely packed arrays of nanorings and split nanorings.

In this dissertation, large-area arrays of magnetic, semiconducting, and insulating nanorings were created by coupling colloidal lithography with nanoscale electrodeposition. This versatile nanoscale fabrication process allows for the independent tuning of the spacing, diameter, and width of the nanorings and was used to form nanorings from a host of materials: Ni, Co, bimetallic Ni/Au, CdSe, and polydopamine. These nanoring arrays have potential applications in memory storage, optical materials, and biosensing. A modified version of this nanoscale electrodeposition process was also used to create arrays of split gold nanorings. The size of the split nanoring opening was controlled by the angle of photoresist exposure during the fabrication process, and could be varied from 50% down to 10% of the ring circumference. The large area (cm^2 scale) gold split nanoring array surfaces exhibited strong polarization dependent

plasmonic absorption bands for wavelengths from 1 to 5 μm. Plasmonic nanoscale split ring arrays are potentially useful as tunable dichroic materials throughout the infrared and near infrared spectral regions.

1.3 Biosensing with Nanostructured Arrays

In Chapter 3 of this dissertation, Au nanoring array surfaces that exhibit strong LSPR at near-infrared wavelengths from 1.1 to 1.6 μm were used as highly sensitive real-time refractive index biosensors. The bulk refractive index sensitivity of the Au nanoring arrays was determined to be up to 3,780 cm^{-1}/refractive index unit by monitoring shifts in the LSPR peak by FT-NIR transmittance spectroscopy measurements. As a first application, the surface polymerization reaction of dopamine to form polydopamine thin films on the nanoring sensor surface from aqueous solution was monitored with the real-time LSPR peak shift measurements. To demonstrate the utility of the Au nanoring arrays for LSPR biosensing, the hybridization adsorption of DNA-functionalized Au nanoparticles onto complementary DNA-functionalized Au nanoring arrays was monitored. The adsorption of DNA-modified Au nanoparticles onto nanoring arrays modified with mixed DNA monolayers that contained only 0.5% complementary DNA was also detected; this relative surface coverage corresponds to the detection of DNA by hybridization adsorption from a 50 pM solution.

1.4 Single Nanoparticle Imaging with SPR Microscopy

Chapter 4 of this dissertation moves from the study of nanostructured surfaces to the study of the adsorption of nanoparticles in solution onto surfaces using surface plasmon resonance microscopy (SPRM). In principle, SPRM is an extension of conventional surface plasmon resonance imaging (SPRI) methods, which utilize reflectivity changes at dielectric – metal interfaces caused by changes in refractive index at the surface upon adsorption of a biological marker. A diagram of an SPR imager is shown in Figure 1.1.

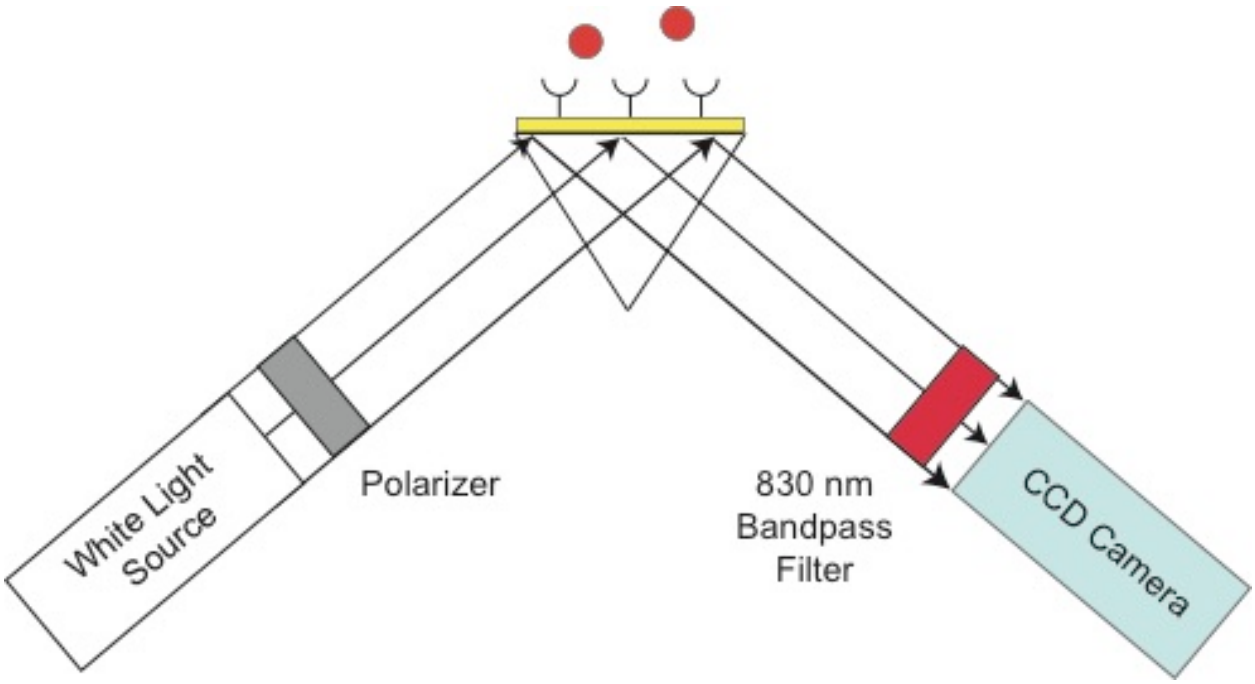

Figure 1.1: Schematic of conventional SPRI. Collimated white light passes through a polarizer to generate *p* polarized light. The light is reflected from a 45 nm Au thin film coupled to a high refractive index prism to achieve a desired incidence angle. The reflected image is passed through an 830 nm bandpass filter to a CCD camera.

Briefly, collimated *p* polarized light impinges onto a high refractive index prism coupled to a thin Au film. The opposite side of this Au film is modified with a biological molecule with specific affinity for the target biomarker and is generally attached to a microfluidic chamber through which the target (shown in red circles) solution is flowed. The light is reflected from a 45 nm Au thin film coupled to a high refractive index prism to achieve a desired incidence angle. The reflected light is passed through an 830 nm bandpass filter to a CCD camera.

The angle of incidence is set at the steepest point of the reflectivity curve, which is plotted in Figure 1.2. The red curve in the Figure is the theoretical reflectivity from *p* polarized 813 nm light incident onto the high refractive index glass SF10 (n = 1.73) with 45 nm Au in water. The resonance arises from the propagation of surface plasmon polaritons (SPPs), which are generated when the frequency of incident light matches that of the conduction electrons in the thin Au film. The dashed line is where the angle of incidence is set and is denoted as θ_{SPRI}. Upon the adsorption of the target compound, the minimum of the reflectivity (denoted as the SPR angle, θ_{SPR}) shifts to a higher angle. The blue curve in Figure 1.2 models the reflectivity curve for SF10 with 45 nm Au with a 3 nm film of material with refractive index of 1.50 (comparable to many biological molecules such as DNA, peptides, and proteins or organic polymers in general) in water. Even though the resonance shifts by less than a quarter of a degree, the change in reflectivity, $\Delta\%R$, is drastic due to the steepness of the curve at θ_{SPRI}. This SPRI signal is tracked and measured in real time from difference images. SPRI has been utilized for detection of biomarkers down to the attomole range.[19]

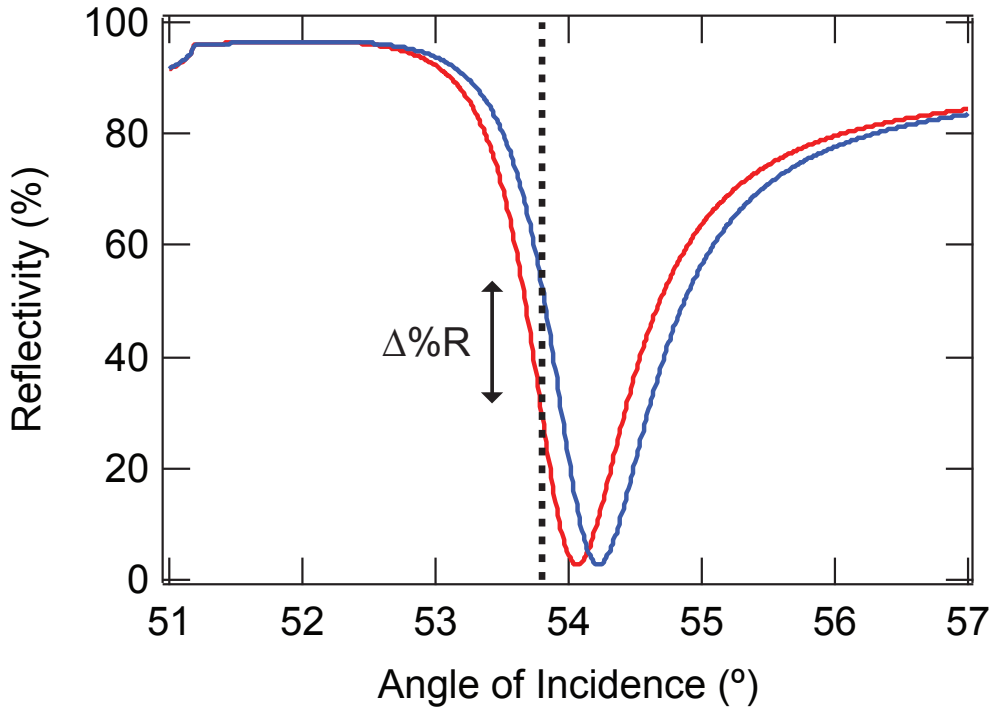

Figure 1.2: SPR reflectivity calculated for a 45 nm Au film on SF10 glass substrate in water (red) with *p* polarized 814 nm light. The adsorption of a biomarker onto the Au film results in an increase in the SPR angle (at the reflectivity minimum). When the incidence angle is set at a steep part of the resonance curve, even an increase of only 0.2° (blue curve) can result in a signal (the change in reflectivity denoted as Δ%R) of 20%.

Single nanoparticle SPRM applies SPRI to the nanoscale by magnifying the incident light through a high numerical aperture objective. Figure 1.3 is a schematic of the SPR microscope used in this dissertation and is very similar to the schematics of the SPR imaging apparatus shown in Figure 1.1. Instead of the collimated white light source and a bandpass filter to set the light wavelength, the SPRM uses a near-infrared (814 nm) laser, which is *p* polarized and focused onto the Au substrate through a 100x objective. A micrometer controlled translation stage attached to a knife-edge mirror directs the laser to the objective and also determines the incidence angle. Typically, 10 μL or less of the target solution is pipetted onto the substrate for imaging.

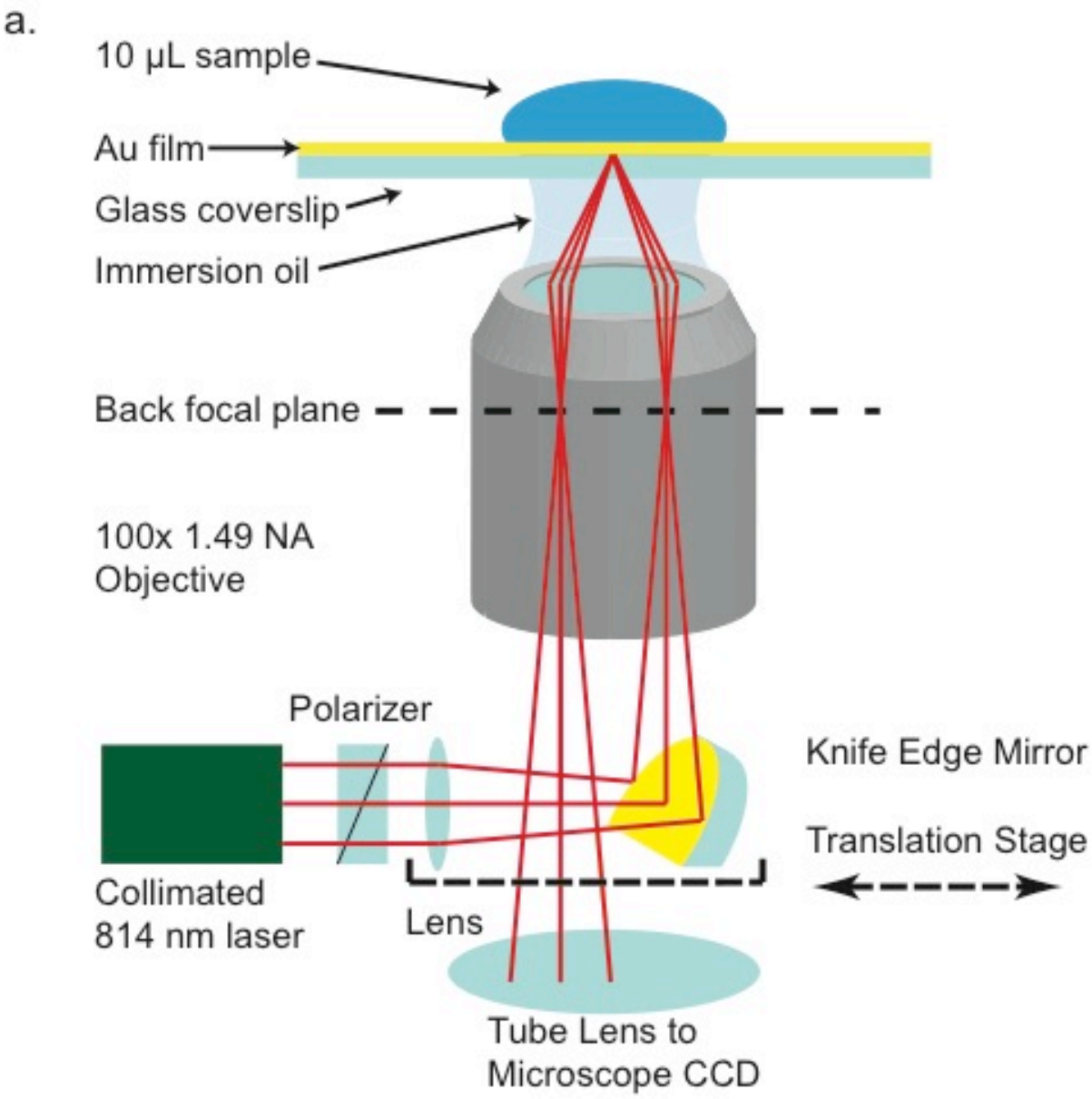

Figure 1.3: Optical setup of the SPR microscope. A 1 mW 814 nm diode laser beam was polarized and focused with a lens (f = 200 mm) onto the back focal plane of a 100x 1.49 NA oil objective. The focused beam was directed up to the objective using a Au-coated knife-edge mirror attached to a translation stage to control the angle of incidence. The reflected image was passed to a CMOS camera.

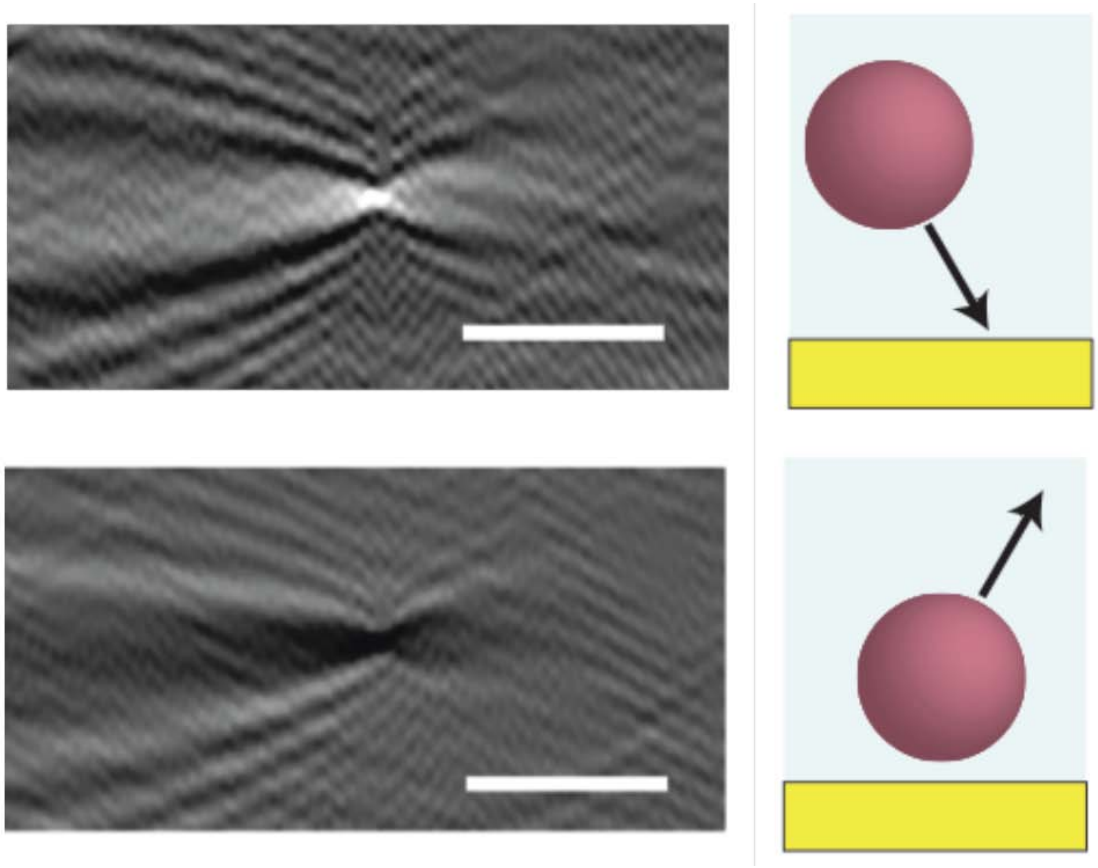

Figure 1.4: Fourier-filtered differential SPRM reflectivity images of the adsorption (top) and desorption (bottom) of a 40 nm Au nanoparticle onto and from a single stranded DNA-functionalized Au surface. The adsorption or desorption of a nanoparticle from a surface results in the generation of a large point diffraction pattern from the propagation of SPPs. Scale bars are 5 μm.

Single nanoparticle SPRM offers several advantages over conventional SPRI, which can only give inofrmation on bulk ensemble measuremnts. By recording a time series of reflectivity images and then generating a series of frame to frame difference images, minute changes (i.e., the adsorption or desorption of an individual nanoparticle) at the Au/buffer interface can be detected by SPRM. In these SPRM differential reflectivity images, the adsorption or desorption of a nanoparticle from the Au surface can be detected by point diffraction patterns arising from the interferences of propagating SPPs upon the minute change at the Au surface. Figure 1.4 shows typical SPRM differential reflective images for the adsorption (top) and desorption

(bottom) of a 40 nm Au nanoparticle from the surface. For these experiments, the Au nanoparticles were functionalized via Au-thiol chemistry with single stranded DNA. The Au surface was also functionalized with a self-assembled monolayer of thiolated-DNA that was complementary to the DNA on the Au nanoparticles. Thus, the nanoparticles were expected to adsorb specfically to the surface by DNA-DNA hybridization.

By counting the number of adsorption and desoprtion events over a course of time, digital binding curves plotting kinetics at the single nanoparticle level can be generated. Previously, the rates of adsorption as monitored by SPRM were reported to be proportional to the nanoparticle concentration.[19] Additionally, the exact locations of where nanoparticles adsorb or desorb from the surface can be tracked over time to create cumulative adsorption maps. By patterning the Au surface, the adsorption of individual nanoparticles can be localized. Figure 1.5 demonstrates this localization onto alternating 5 μm and 10 μm stripes of undecane-amine and polyethylene glycol, respectively. In the Figure, the electrostatic adsorption of 220 nm carboxylated polystyrene nanoparticles onto amino-functionalized 5 μm stripes is clearly visible.

In addition to tracking binding events over time, the SPRM differential reflectivity response to nanoparticle adsorption can be quantified. Previously, this signal was shown to be dependant on both the nanoparticle size and composition.[19] The size dependance of the signal is apparent in the SPRM differential image shown in Figure 1.6. In the Figure, the adsorption of a mixture of 405 nm and 220 nm hydrogel nanoparticles are visible. The imaging and distinguishing of such a mixture of nanoparticles is not possible by ensemble measurements where only average results can be tracked.

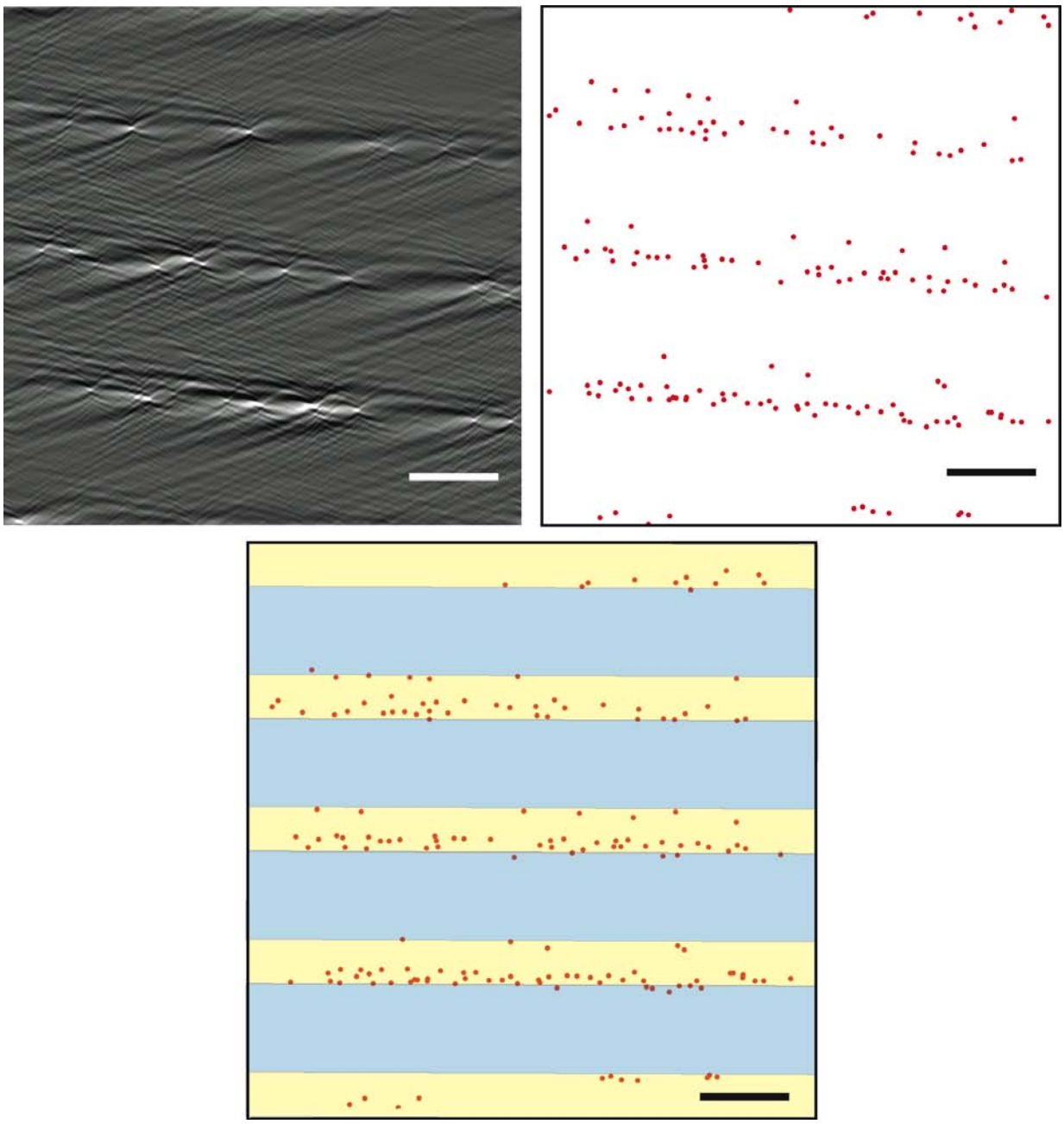

Figure 1.5: (clockwise from top left) A 58.5 μm x 58.5 μm Fourier-filtered SPRM differential reflectivity image (three second exposures) showing the adsorption of 200 nm carboxylated polystyrene nanoparticles onto a surface consisting of alternating 5 μm stripes of amino-functionalized Au and 10 μm stripes of polyethylene glycol; cumulative adsorption map after 10 minutes of the same surface with red dots indicating the locations of adsorbed nanoparticles; the same map rotated and overlaid with alternating 5 μm and 10 μm stripes. Scale bars: 10 μm.

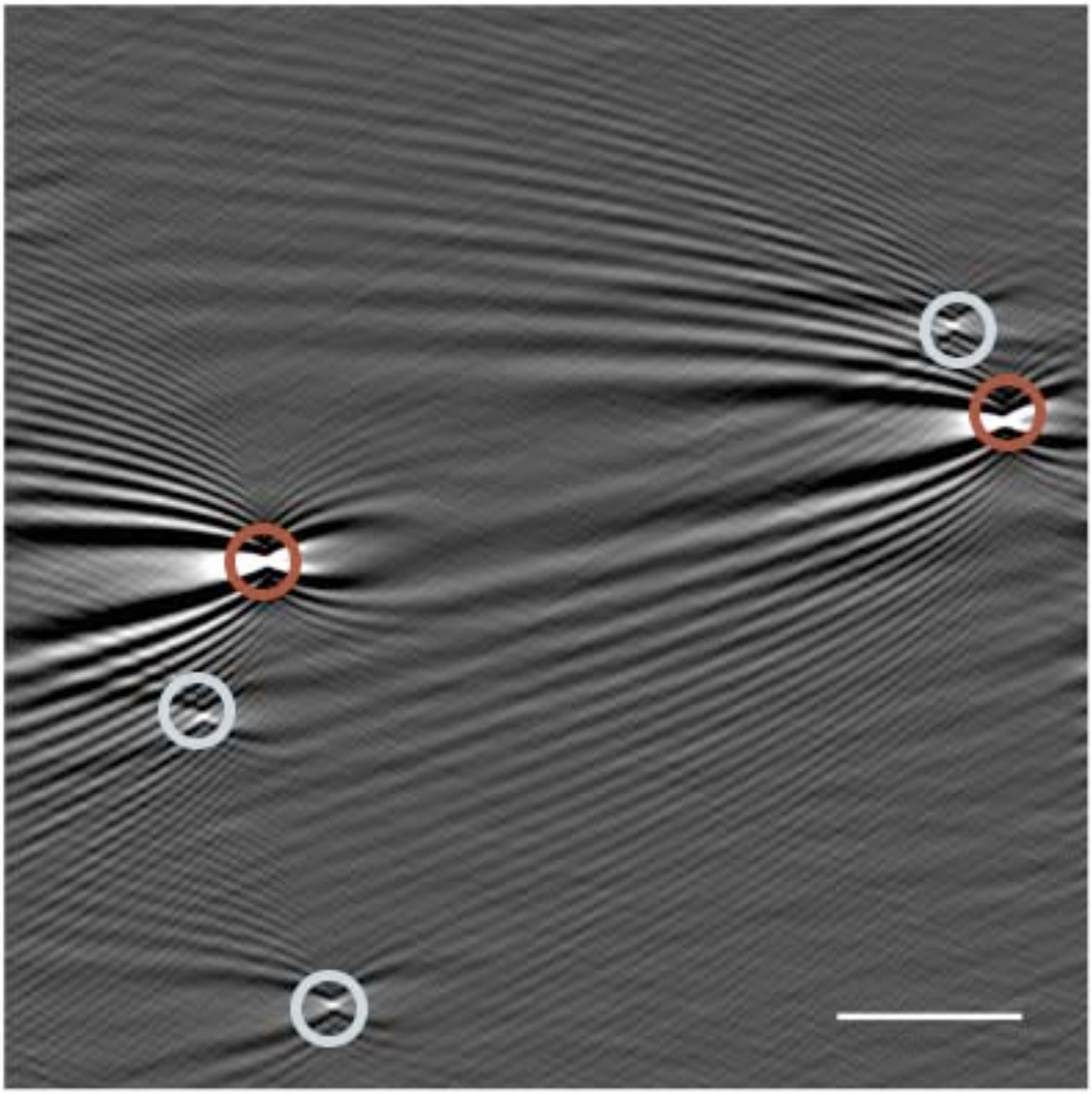

Figure 1.6: Mixture of 220 nm and 405 nm hydrogel nanoparticles adsorbing onto undecane functionalized Au visualized in a Fourier-filtered SPRM differential reflectivity image. Red circles denote the adsorption of 405 nm nanoparticles and the blue circles denote the observation of 220 nm nanoparticles. Scale bar: 10 μm.

In Chapter 4 of this dissertation, the specific uptake of the bioactive peptide melittin into *N*-isopropylacrylamide (NIPAm) hydrogel nanoparticles (HNPs) that contain a mixture of hydrophobic and negatively charged side groups is measured with near-infrared single

nanoparticle surface plasmon resonance microscopy (SPRM). Point diffraction patterns in sequential real-time SPRM differential reflectivity images are counted to create digital adsorption binding curves of single 220 nm HNPs from picomolar nanoparticle solutions onto hydrophobic alkanethiol-modified Au surfaces. The intensity of hundreds of point diffraction features observed in the adsorption binding curves is also measured; the average of these single nanoparticle SPRM reflectivity changes, $<\Delta\%R_{NP}>$, is found to increase linearly with concentration from 1.04 ± 0.04% to 2.10 ± 0.10% for HNPs in zero to 2.5 μM melittin solutions. The increase in $<\Delta\%R_{NP}>$ is attributed to an increase in the refractive index of the HNPs due to the uptake of melittin. No change in the average HNP size in the presence of melittin is observed with dynamic light scattering measurements, and no increase in $<\Delta\%R_{NP}>$ is observed in the presence of either FLAG octapeptide or bovine serum albumin. Additional bulk fluorescence measurements of melittin uptake into HNPs are used to estimate that a 1% increase in $<\Delta\%R_{NP}>$ observed in SPRM corresponds to the incorporation of approximately 65,000 molecules into each 220 nm HNP, corresponding to roughly 4% of its volume. The lowest detected amount of melittin loading into the 220 nm HNPs was an increase in $<\Delta\%R_{NP}>$ of 0.15%, corresponding to the absorption of 10,000 molecules.

1.5 References

(1) Dykman, L.; Khlebtsov, N. *Chem. Soc. Rev.* **2012**, *41*, 2256-2282.

(2) Pumera, M. *Energy Environ. Sci.* **2011**, *4*, 668-674.

(3) Holzinger, M; Le Goff, A; Cosnier, S. *Front Chem.* **2014**, *2*, 63.

(4) Mayer, K.M.; Hafner, J.H. *Chem. Rev.* **2011**, *111*, 3828-3857.

(5) Homola, J.; Yee, S.S.; Gauglitz, G. *Sens. Actuators, B* **1999**, *54*, 3-15.

(6) Ha, T.; Tinnefeld, P. *Ann. Rev. Phys. Chem.* 2012, 63, 595-617.

(7) Gebhardt, J.C.M.; Suter, D.M.; Roy, R.; Zhao, W.Z.; Chapman, A.R.; Basu, S.; Maniatis, T.; Xie, X.S. *Nat. Methods*, 2013, 10, 421-426.

(8) Huang, C.; Ye, J.; Wang, S.; Stakenborg, T.; Lagae, L. *Appl. Phys. Lett.* **2012**, *100*, 173114.

(9) Jiang, H.; Li, T.; Yang, J.; Mittler, S.; Sabarinathan, J. *Nanotech.* **2013**, *24*, 465502.

(10) Metlushko, V.; Welp, U.; Vlasko-Vlasov, V.; Crabtree, G.; Zaluzec, N.; Hiller, J.; Grimsditch, M.; Ilic, B.; Bekaert, J.; Moshchalkov, V.V.; Bruynseraede, Y.; Das, J.; De Boeck, J.; Borghs, G.; Zhu, X.; Grutter, P. *Nanotech*. **2002**, *1*, 63-66.

(11) Castano, F.J.; Ross, C.A.; Frandsen, C.; Eilez, A.; Gil, D.; Smith, H.I.; Redjdal, M., Humphrey, F.B. *Phys. Rev. B.* **2003**, *67*, 184425.

(12) Plum, E.; Liu, X.-X.; Fedotov, V.A.; Chen, Y.; Tsai, D.P., Zheludev, N.I. *Phys. Rev. Lett.* **2009**, *102*, 113902.

(13) Menke, E.J.; Thompson, M.A.; Xiang, C.; Yang, L.C.; Penner, R.M. *Nat. Mater.* **2006**, *5*, 914-919.

(14) Li, X.; Liu, Y.; Hemminger, J.C.; Penner, R.M. *ACS Nano* in press.

(15) Arter, J.A.; Diaz, J.E.; Donavan, K.C.; Penner, R.M.; Weiss, G.A. *Anal. Chem.* 2012, 84, 2924-2930.

(16) Dutta, R.; Albee, B.; van der Veer, W.E.; Donovan, K.C.; Papamoschou, D.; Penner, R.M. *J. Phys. Chem. C* 2014, 118, 29101-29107.

(17) Ayvazian, T.; Xing, W.; Yan, W.; Penner, R.M. *ACS Appl. Mater. Interfaces* **2012**, *4*, 4445-4452.

(18) Gifford, L.K.; Sendroiu, I.E.; Corn, R.M.; Lupták, A. *J. Am. Chem. Soc.* **2010**, *132*, 9265-9267.

(19) Halpern, A.R.; Wood, J.B.; Wang, Y.; Corn, R.M. *ACS Nano*, **2014**, *8,* 1022-1030.

Chapter 2

Lithographically Patterned Nanoscale Electrodeposition of Plasmonic, Bimetallic, Semiconductor, Magnetic, and Polymer Nanoring Arrays

2.1 Introduction

The unique physical properties attributed to nanoscale materials have led to a rise of nanomaterials research in recent years. For example, nanopatterned magnetic structures have been studied for applications as varied as high-density data storage to biomarker sensing.[1-4] Semiconducting nanostructures have been developed for quantum confined materials and devices.[5-7] Additionally, plasmonic nanomaterials have received much attention due to their

unique optical and electronic properties as well as their potential implementation in a variety of applications including ultra-sensitive biosensors, enhanced surface-sensitive spectroscopy, and optical metamaterials.[8-14] Optical metamaterials, defined as periodic structures whose features are smaller than the wavelength of light, can be used to create a variety of unique optical effects: negative refractive index materials, cloaking devices, and perfect lenses.[11, 15]

The fabrication of nanoring arrays has been of particular interest in nanomaterials research. Magnetic nanorings have been proposed as an ideal candidate for use in random access memory devices due to their well-defined magnetic remnant states, which would be suitable for data storage of multiple bits for each ring.[1, 16] Also, the strong plasmonic resonance arising from Au nanorings have been used for detecting polymer film growth and for DNA biosensing.[10] In addition to nanorings, an optical metamaterial that has been the focus of much interest is arrays of split ring resonators, which have been exploited to create materials with negative permeability and negative refractive index in the near infrared (NIR), infrared (IR), and microwave spectral regions.[17-19] Plasmonic split nanoring arrays exhibit a strongly polarization dependent absorption spectrum and can be employed for nanophotonic biosensors and plasmonic NIR dichroic polarizing filters.[12, 20] In addition, electromagnetic hot spots in the closely related nanocrescent structures have been used in localized surface plasmon resonance (LSPR)-based sensing and surface-enhanced spectroscopies (e.g., Raman and infrared absorption).[21-25] Composite plasmonic and magnetic nanocrescents have been employed as surface-enhanced Raman scattering substrates that are capable of being controlled by external magnetic fields.[26]

This recent growth in nanotechnology has necessitated the development of facile, inexpensive, and high throughput processes for the fabrication of nanoscale periodic arrays that are made of a large number of materials. While electron beam lithography (EBL) can be used to

generate such nanostructures on the scale of tens to hundreds of microns,[12, 18, 20, 27, 28] the time and cost required to fabricate arrays over larger areas using EBL is prohibitive. Alternatively, patterned nanostructures have been fabricated using such methods as nanochannel glass replica membranes,[29, 30] colloidal lithography,[31] and evaporative self assembly.[32] We have recently described a novel method for the fabrication of plasmonic nanoring arrays over large areas (cm^2) that combines colloidal lithography with lithographically patterned nanoscale electrodeposition (LPNE). [33]

In this paper, we expand the use of this nanofabrication method to make large-scale arrays of nanorings and split nanorings from a wide range of materials, including magnetic materials (nickel and cobalt), semiconductors (cadmium selenide), and insulating polymers (polydopamine). Additionally, we present bimetallic (nickel/gold) and split gold nanoring arrays as examples of extending our fabrication strategy to create more complex nanostructured surfaces. The large area fabrication method described here provides a high degree of control over nanoscale features such as spacing, radii, thickness, and (in the case of split nanorings) the ring opening size.

2.2 Experimental Section

2.2.1 Materials

Carboxylate coated polystyrene beads solutions (2.6% w/v, 1 μm diameter) were purchased from Polysciences (Warrington, PA). Shipley S1808 photoresist, Thinner P, and MF-319 developer were purchased from Microchem (Newton, MA). Clean Earth Chemicals 24K gold plating solution (Grobet USA, Carlstadt, NJ) was used as received. Fisher Premium glass microscope slides (1 mm thick) were used as substrates. 20 nm magnetite nanoparticles (20

mg/mL in citrate buffer) were purchased from nanoComposix (San Diego, CA) and diluted 1000 fold in water prior to use.

2.2.2 Nanoring and split nanoring array fabrication

A densely-packed monolayer of polystyrene beads was formed by spin coating polystyrene beads (concentrated to 5.2% in 3:1 methanol: water) on hydrophilic oxygen plasma cleaned microscope glass slides cut to 2.5 cm x 2.5 cm pieces. Upon drying, the beads were etched in oxygen plasma (200 mTorr, 50 W, − 400 VDC, South Bay Technologies, San Clemente, CA) for 5 minutes. A 70 nm layer of Ag (over a 1 nm Cr adhesion layer) was vapor deposited on top of the etched beads by thermal evaporation. To remove the beads, the samples were sonicated sequentially in toluene and acentone. Shipley S1808 photoresist (diluted 1:1 with Thinner P) was spin coated on the nanohole arrays (80 s, 2500 rpm) and baked for 20 min at 90 °C. The photoresist was backside exposed through the nanohole array with 20 mW/cm^2. For split nanoring arrays, the angle of exposure was controlled by mounting the samples onto triangular blocks cut to achieve the desired angles. A potentiostat (PGSTAT12, Metrohm, Riverview, FL) was used for electrodeposition. Ni, Co, CdSe and Au were deposited by potentiostatic electrodeposition using the following plating conditions: Ni: -0.85 V for 9 minutes using a Ni plating solution (5 mM $NiCl_2$, 5 mM boric acid, 0.1 M KCl); Co: -1.2 V for 2.5 minutes using a Co plating solution (0.14 M $CoSO_4$ and 0.65 M boric acid); CdSe: -0.64 V for 7 minutes using a CdSe plating solution (0.30 M $CdSO_4$, 0.70 mM SeO_2, and 0.25 M H_2SO_4); Au: -0.85 V for 10 minutes using a commercial gold plating solution. Polydopamine was deposited by cyclic voltammetry (20 scans at a rate of 20 mV/s; vertex potentials of -0.6 V and 0.66 V) in a dopamine solution (5mM dopamine in phosphate buffer (pH 6.5)). All potentials were measured

versus a Ag/AgCl reference electrode; a Pt foil was used as the counter-electrode. After electrodeposition, the photoresist was washed off with acetone. The Ag sacrificial electrode was removed with a 5% NH_4OH and 1% H_2O_2 etching solution.

2.2.3 Sample Characterization

SEM: The samples were imaged on a FEI Magellan scanning electron microscope. XRD: Grazing incidence x-ray diffraction measurements were performed on a Rigaku SmartLab X-ray Diffractometer. FT-NIR Absorption Spectra: A Mattson RS-1 FTIR with a halogen source, CaF_2 beamsplitter and InSb detector was used to capture NIR spectra from 2000–10000 cm^{-1}. The beam was focused to 3 mm in diameter to interrogate different areas of the sample. A bare glass slide was used as the background reference spectrum.

2.3 Results and Discussion

2.3.1 Nanoring and Split Nanoring Array Fabrication

Our method to fabricate of magnetic, semiconducting, bimetallic, and insulating nanoring arrays and plasmonic split nanoring arrays (illustrated in Figure 2.1) is an extension of our previous methodology for lithographically patterned electrodeposition of plasmonic nanoring arrays.[33] First, carboxylate functionalized polystyrene beads dispersed in a mixture of ethanol and water are spin cast onto an oxygen plasma treated glass substrate to form a tightly packed monolayer. The beads are then etched to the desired size in oxygen plasma (Fig. 2.1a). A sacrificial metal film (70 nm silver) is then formed by evaporation deposition over the etched beads, which are subsequently dissolved in toluene, yielding a nanohole array (Fig. 2.1b).

Positive photoresist is then spin coated over the nanohole array (Fig. 2.1c). For closed nanoring fabrication, exposure of the photoresist at normal incidence (Fig. 2.1d) results in complete opening of the nanoholes. In contrast, for split nanoring arrays, exposure at an angle θ from the surface normal (Fig. 2.1h) leaves part of the photoresist unexposed; thus, the holes do not completely open upon photoresist development (Fig. 2.1i). During the electrodeposition step (Fig. 2.1f and 2.1j), with the nanohole array acting as the working electrode, the desired material can only be deposited on the exposed metal. This process results in fully closed nanoring arrays when θ = 0° (Fig. 2.1g) or split nanorings when exposed at an angle (Fig. 2.1k) after removal of photoresist and sacrificial metal material.

This fabrication method combination offers complete control over all size parameters of the array. As discussed previously,[33] the periodicity of individual split nanorings is determined by the initial size of the polystyrene beads; the outer diameter is controlled by the time exposed to oxygen plasma; and the nanoring thickness and inner diameter are controlled by amount of charge passed during the electrodeposition process. Finally, the nanoring opening size is determined by the exposure angle θ (θ = 0° for closed rings). The described method produces square centimeter scale arrays of nanoscale structures while avoiding relatively expensive and time-consuming sequential fabrication processes such as EBL. In addition to size and dimensional control, we are able to form nanoring arrays from a broad range of materials available for electrodeposition.

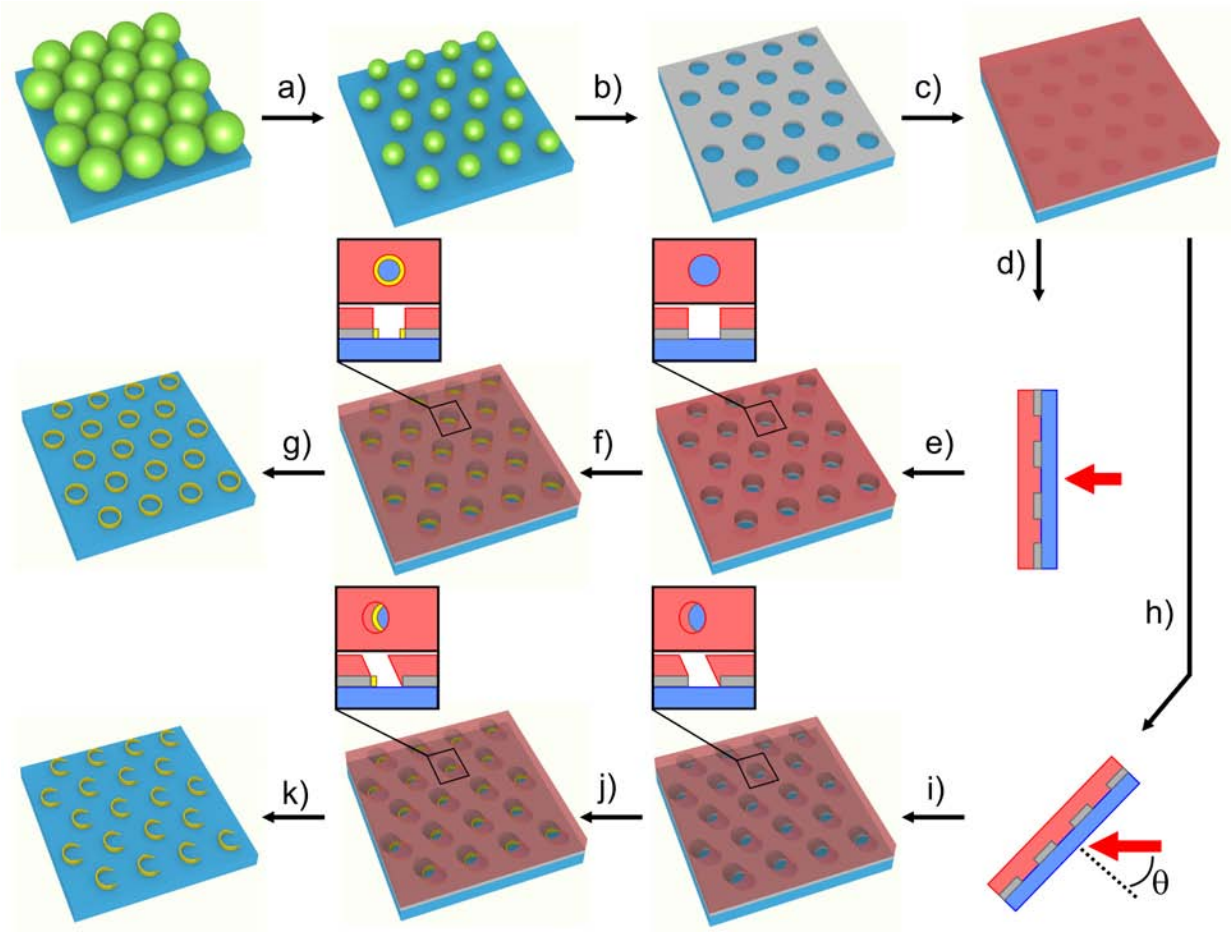

Figure 2.1: Nanoring and split nanoring array fabrication scheme: (a) polystyrene beads self-assembled in a monolayer are etched to size in an oxygen plasma; (b) nanohole mask is formed by vapor depositing silver over the etched beads and removing the beads; (c) positive photoresist is spin coated onto the nanohole mask. For nanorings: (d) photoresist is backside exposed at normal incidence through the nanoholes; (e) holes are formed in the photoresist upon development; (f) nanorings are electrodeposited onto the exposed silver; and (g) photoresist and silver are removed to reveal nanorings. For split nanorings: (h) exposure at an angle θ leaves part of the nanohole covered by photoresist after (i) development; (j) split nanoring is electrodeposited through the holes formed in the photoresist to the exposed silver; and (k) split nanorings arrays are completed upon photoresist and silver removal.

2.3.2 Magnetic Nanorings and Nanomushrooms

Using our combined colloidal lithography and nanoscale electrodeposition process, we have fabricated nanoring arrays of nickel, a well-known ferromagnetic material. A top-down scanning electron microscope (SEM) image of a Ni nanoring array formed from 1 μm diameter

polystyrene beads is shown in Figure 2.2a. In addition to simply nickel nanorings, we have formed composite magnetic and plasmonic nanorings by sequential electrodeposition of nickel and gold (step "g" in Fig. 2.1). By this process, the resulting bimetallic nanorings have a core of nickel and a shell of gold; the shell does not completely envelope the nickel because the outer part of the nickel rings is not available for gold electrodeposition. We confirmed this core-shell structure by etching away exposed nickel in nitric acid; when compared to the bimetallic structure before etching (Fig. 2.2c), a distinct gold lip over where the nickel had been is visible (Fig. 2.2d). Fourier transform near infrared (FT-NIR) absorbance spectra of nickel and nickel/gold nanoring arrays are depicted in Figure 2.2b. The nickel spectrum shows a resonance at 5000 cm^{-1} and a weaker higher order resonance at 9000 cm^{-1}. As expected, the addition of a gold shell greatly enhances the resonant response of the nanoring arrays. Interestingly, we see a strong and distinct double resonance for our bimetallic nanorings, which likely corresponds to two resonances from nickel and gold.

In addition to nickel, we have also fabricated magnetic nanostructures with cobalt. The cobalt deposition was performed by potentiostatic electrodeposition in an electrolyte containing cobalt sulfate and boric acid.[34] Successful deposition of cobalt was confirmed by XRD (Fig. 2.3d). While a top-down view (Fig. 2.3a.) of the cobalt structures makes the array appear as tightly packed rings, a tilted view (Fig. 2.3b) on the SEM reveals mushroom like structures. These "nanomushrooms" are a result of electrodeposition out of the photoresist hole to the top of the photoresist layer. We tested the ferromagnetism of the nanomushrooms by immersing the array into a solution of 20 nm magnetite nanoparticles. After thorough rinsing in water and ethanol, followed by drying under a nitrogen stream, the studding of the nanomushrooms by the nanoparticles was confirmed by SEM (Fig. 2.3c). The physical anisotropy present in these

nanomushrooms is difficult to replicate using traditional nanofabrication strategies and opens the door to facile production of similar structures made with magnetic or nonmagnetic materials.

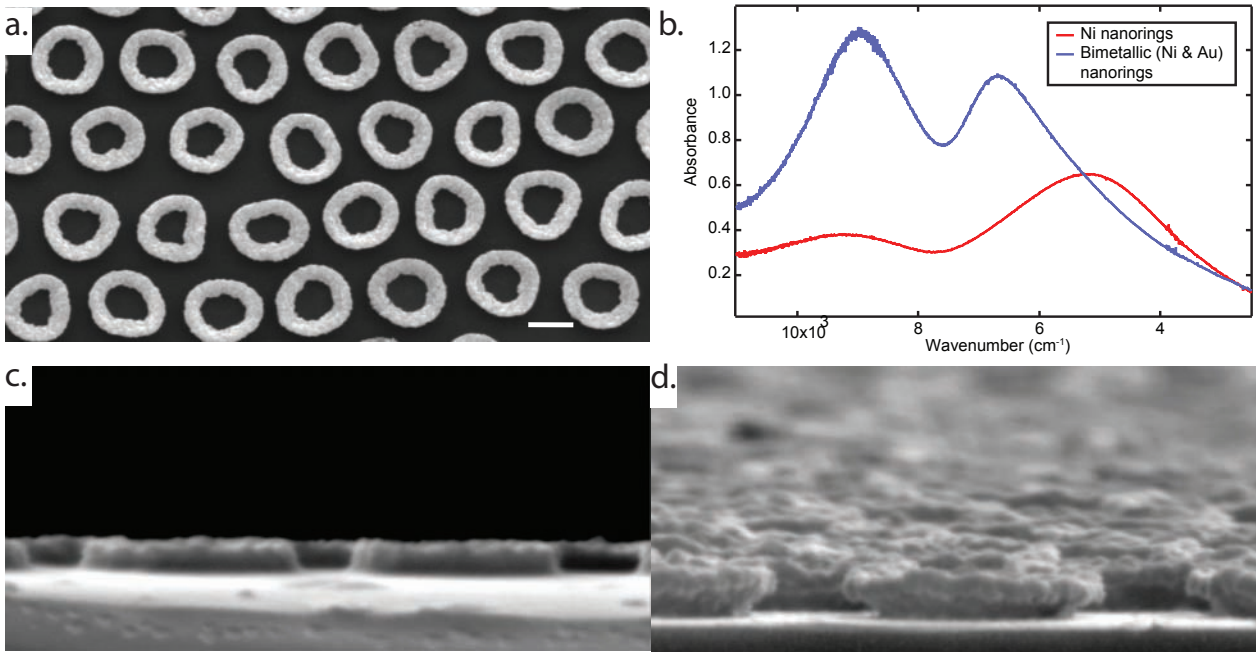

Figure 2.2: (a) Top-down SEM image of nickel nanoring array. (b) FT-NIR absorbance spectra of nickel (red) and core-shell nickel/gold (blue) nanoring arrays. (c,d) Cross-sectional views of nickel/gold rings before (c) and after (d) etching of nickel in nitric acid. Scale bars: 500 nm.

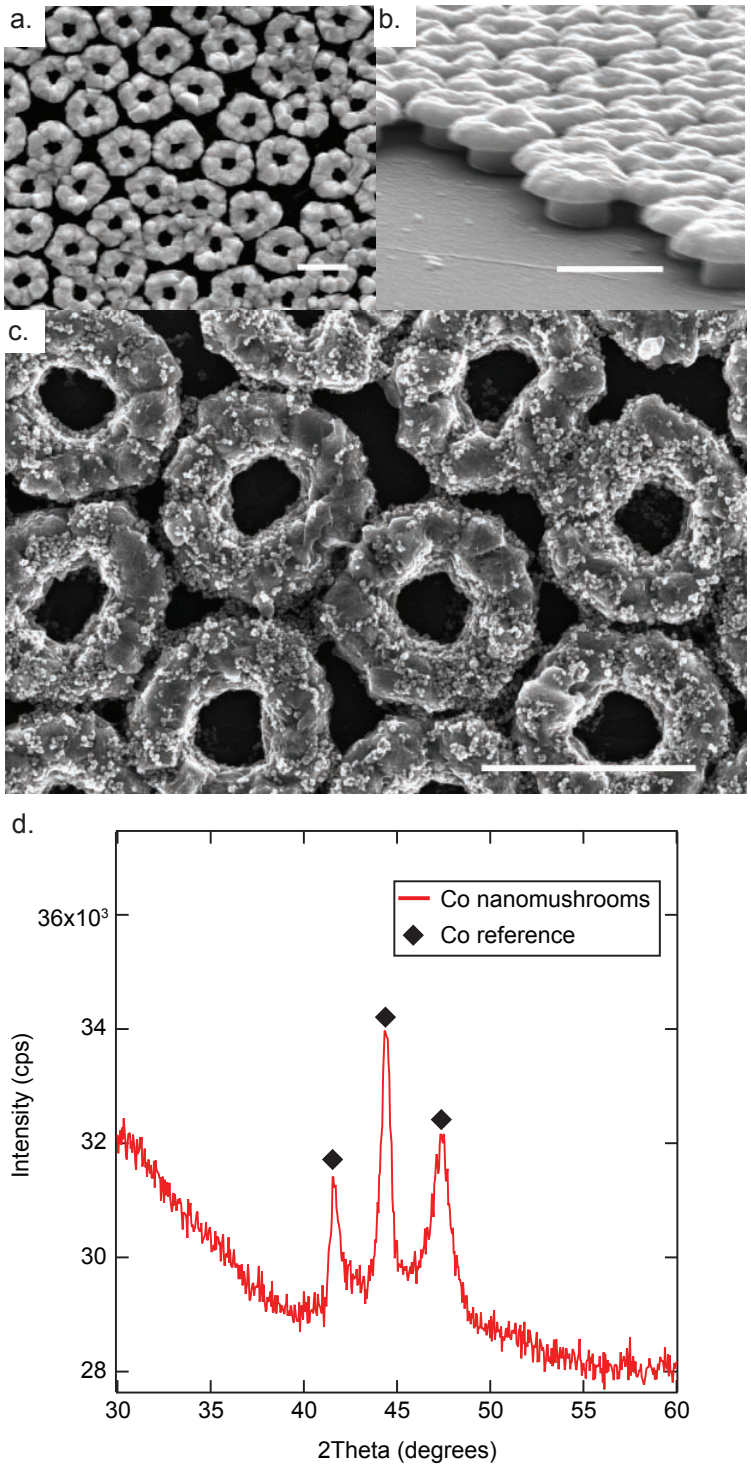

Figure 2.3: (a,b) Top-down (a) and tilted (b) SEM images of cobalt nanomushrooms. (c) Cobalt nanomushrooms after immersion in a solution of magnetite nanoparticles. (d) Confirmation by XRD of cobalt electrodeposition. Scale bars: 1 μm.

2.3.3 Semiconducting and Insulating Nanorings

Along with metallic nanoring arrays, we are also able to fabricate nanorings of semiconducting and insulating materials. As an example of nanoring arrays of a semiconductor material, we electrodeposited cadmium selenide by potentiostatic deposition (SEM image shown in Fig. 2.4a) and confirmed the structure by XRD analysis (Fig. 2.4b). Our fabrication method could provide a facile and high throughput route for production of quantum rings.

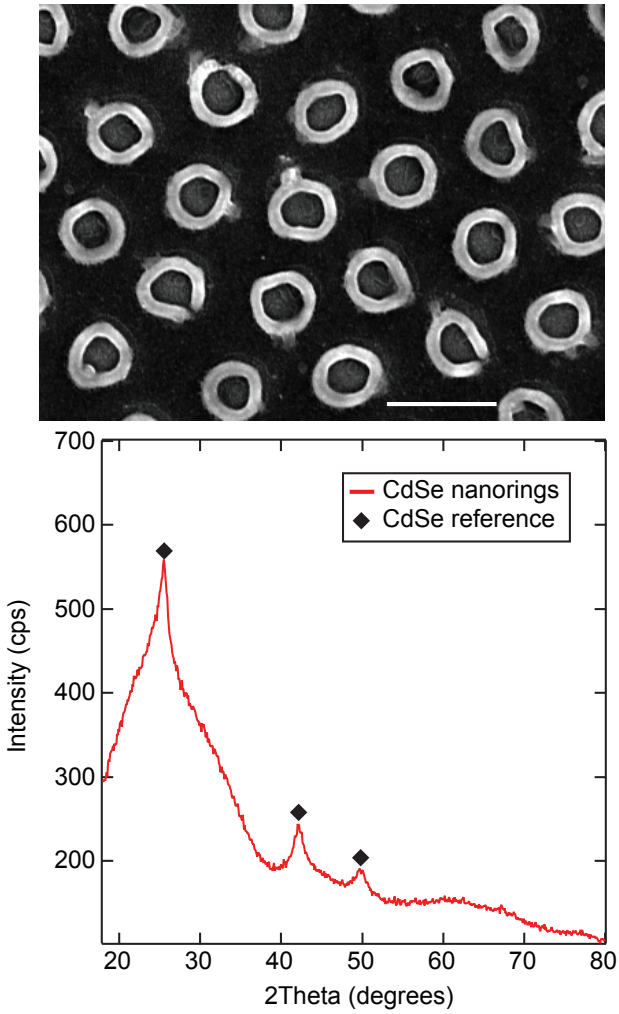

Figure 2.4: SEM image of CdSe nanorings and confirmation of CdSe electrodeposition by XRD. Scale bar: 1 μm.

Additionally, nanoring arrays of insulating materials have been fabricated using this process. We have recently reported the electrodeposition of polydopamine (PDA) thin films for patterning DNA microarray.[35] This deposition was performed by repeated cyclic voltammetry (CV) scans at a carefully controlled pH. Our nanoring fabrication strategy allows us to scale down PDA electrodeposition to the nanoscale. Figure 2.5a depicts SEM images of PDA nanorings at two magnifications. While we expect the thickness of these PDA rings to be around 3 nm,[35] we can see in the inset that the thickness appears to be much greater, which we attribute to the collapsing of the PDA structure upon removal of the sacrificial electrode. As expected, the cathodic and anodic currents in the cyclic voltammograms decrease with repeated cycle numbers as the surface becomes more coated with PDA and thus electrically passivated. As we have shown previously with macroscale films, these nanoscale PDA ring arrays will allow the development of nanoscale biosensing platforms.

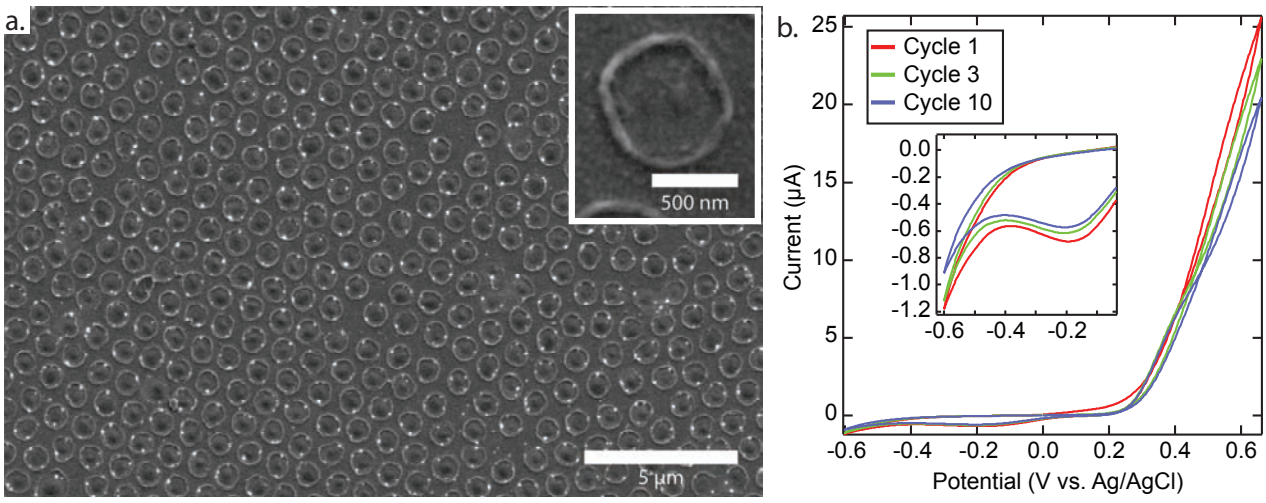

Figure 2.5: (a) SEM images of PDA nanorings at low and high (inset) magnifications. (b) Cyclic voltammograms of cycles 1, 3, and 10 during the growth of PDA nanorings.

2.3.4 Split Nanorings

In addition to forming nanorings of a multitude of materials, our fabrication strategy allows us to also produce split nanorings and control the ring opening size. Gold split nanoring arrays were characterized by a combination of SEM and polarized Fourier transform near infrared (FT-NIR) spectroscopy. As shown in the SEM image in Figure 2.6a, this angled photoexposure process creates an array where the openings are all on the same position on the nanorings. The size of the nanoring opening can be tuned by varying the exposure angle (θ) of the photoresist, as seen in the SEM images in Figures 2.6b – 2.6d. For a given exposure dosage, a smaller θ results in smaller ring openings. As seen in the SEM images, the ring opening can be controlled to be 50%, 20%, or 10% of the ring circumference by exposing at a θ of 45°, 40°, and 35°, respectively.

The NIR absorption spectra of these gold split nanoring arrays were characterized as a function of optical polarization with respect to the ring gap orientation. Transmission spectra were taken with light at normal incidence to the array surface. In this configuration, the split ring arrays exhibit strong infrared resonances that are dependent on the polarization of the incident light. As seen in Figure 2.7, two distinct resonances are apparent in the near to mid infrared region as the polarization of the light is varied from φ = 0° (perpendicular to the ring opening; red trace), φ = 30° (orange trace), φ = 60° (green trace), to φ = 90° (blue trace). Two bands are observed in the optical spectrum: one at 7400 cm^{-1} that dominates when φ = 0° and the other at 3800 cm^{-1} that dominates when φ = 90°.

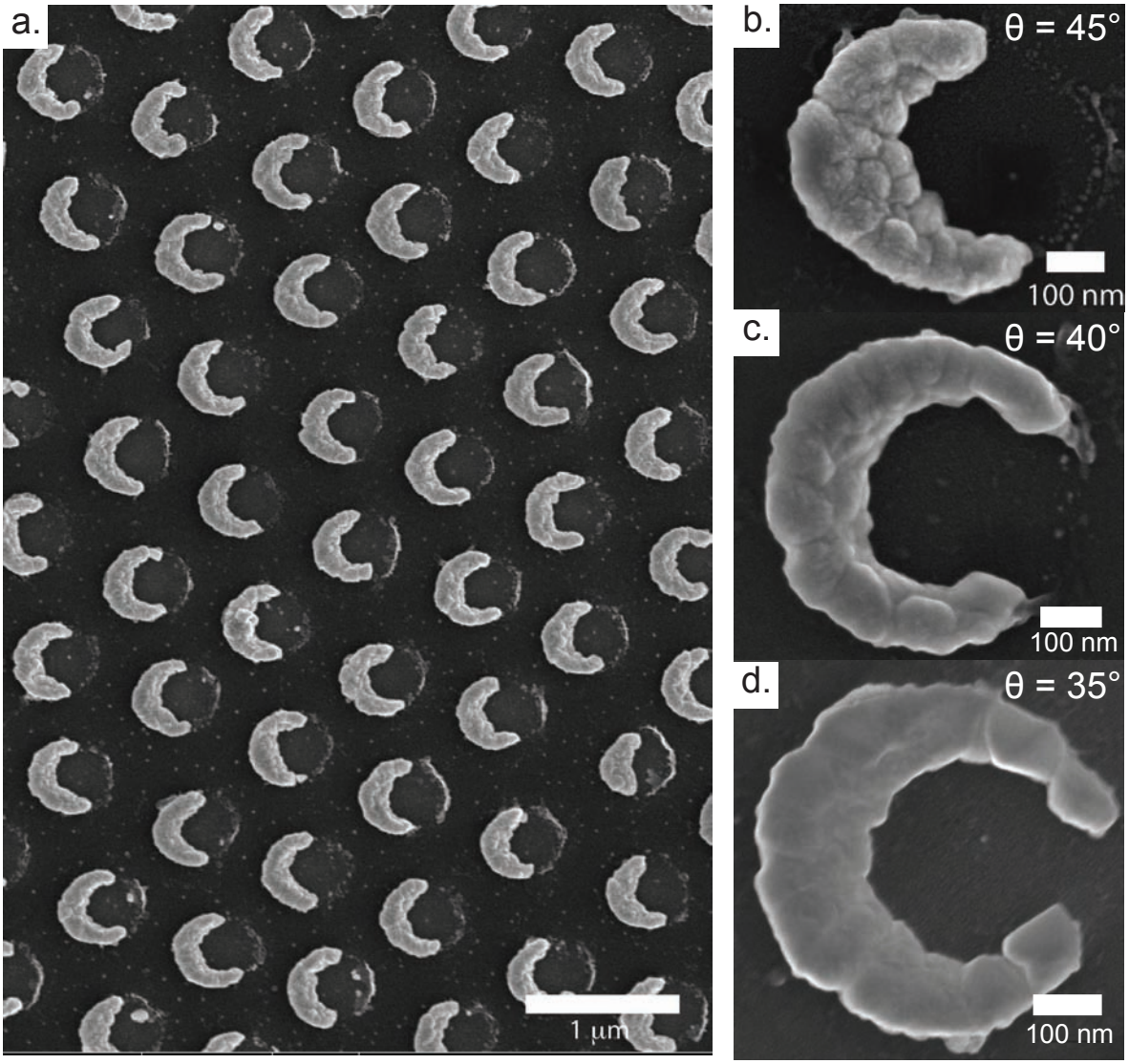

Figure 2.6: SEM images of nanocrescents and split nanorings. The size of the ring openings decreases with the angle of the backside UV exposure, θ: (a) and (b) θ = 45°, (c) θ = 40°, and (d) θ = 35°.

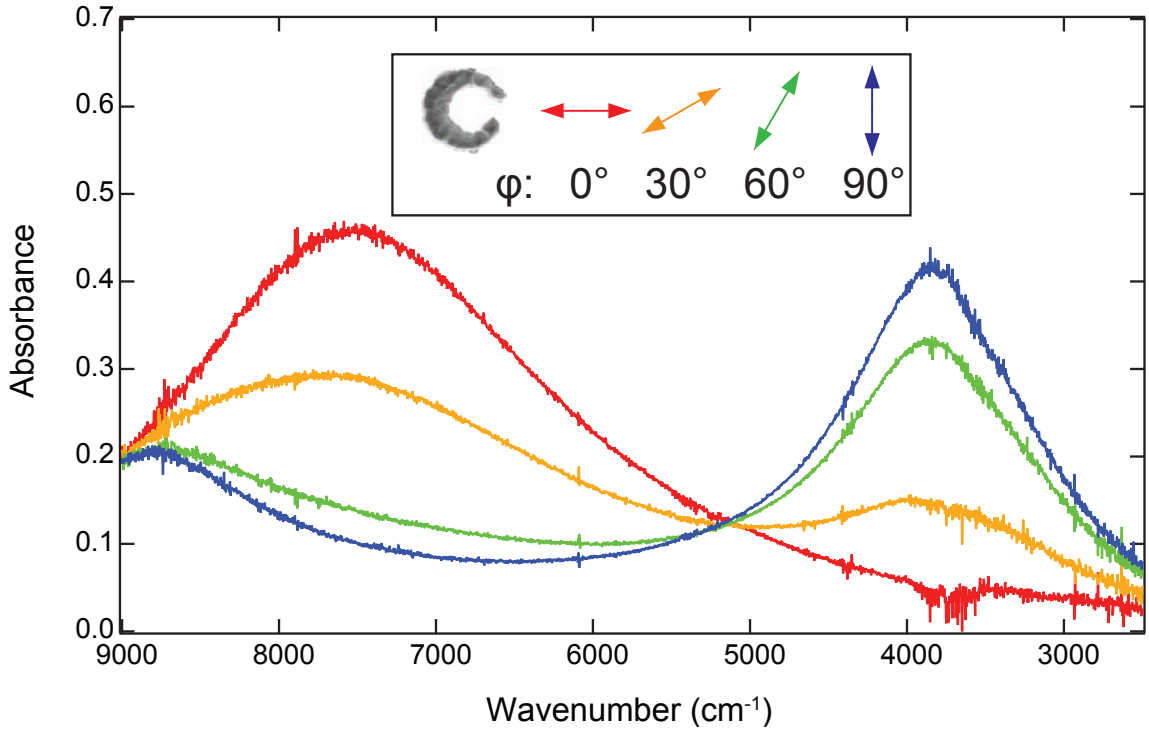

Figure 2.7: Polarization dependence of near-infrared absorbance for a split ring array. Polarization of the incident light was rotated in 30 degrees increments on the same spot of the same sample starting perpendicular to the ring openings (red, φ = 0) and continuing until parallel to the ring openings (blue, φ = 90).

These two NIR bands are plasmonic resonances of split nanoring arrays that have been observed previously.[27, 28, 36-38] The openings in the nanorings break the symmetry of the ring geometry and drastically change the surface charge distributions (and thus the optical responses) for different polarization states. The lower frequency resonance in Figure 2.7 (at 3800 cm^{-1}) that dominates when light is polarized across ring opening (φ = 90°) is commonly referred to as the LC resonance, in which the gap in the split ring acts as a capacitor. Following this analogy, decreased capacitance from larger gaps results in higher frequency resonances. The higher frequency resonance in Figure 2.7 (at 7400 cm^{-1}), which is strongest when light is polarized perpendicular to the ring opening (φ = 0°), corresponds to a plasmon mode that redshifts in

response to smaller ring openings. As expected, the LC resonance becomes dampened as the polarization is rotated and less of the electric field is directed across the ring opening; this resonance disappears completely after 90° rotation.

The position of the two resonances could be controlled by varying the size of the rings and the amount of nanoring opening. Figure 2.8 depicts the responses to light polarization along (8a, $\varphi = 0°$) and across (8b, $\varphi = 90°$) the ring openings for the three samples imaged in Figure 2.6 formed with back exposure angle $\theta = 45°$ (blue trace), $\theta = 40°$ (green trace), and $\theta = 35°$ (red trace). As noted above, all conditions other than θ were the same (i.e., the only difference between the three samples was the size of the ring openings). As the nanoring openings increase with increased exposure angle θ, both the higher and lower frequency resonances (corresponding to the resonances for the two polarizations) appear at higher wavenumbers. The blueshift of the higher frequency resonance with increasing ring opening in Figure 2.8a can be attributed to the decrease in the sides of the rings as the opening gets larger. The LC resonance (Figure 8b) also blueshifts with larger ring openings, as expected. For our split nanorings, the position of this LC resonance could be tuned to a range greater than 2000 cm^{-1} by simply changing the size of the ring opening. For comparison, the peak resonance position of fully closed nanorings (fabricated under the same conditions with normal incidence exposure of the photoresist) is indicated by the dotted lines in Figure 2.8. Predictably, the resonance position for fully closed rings does not change with polarization.

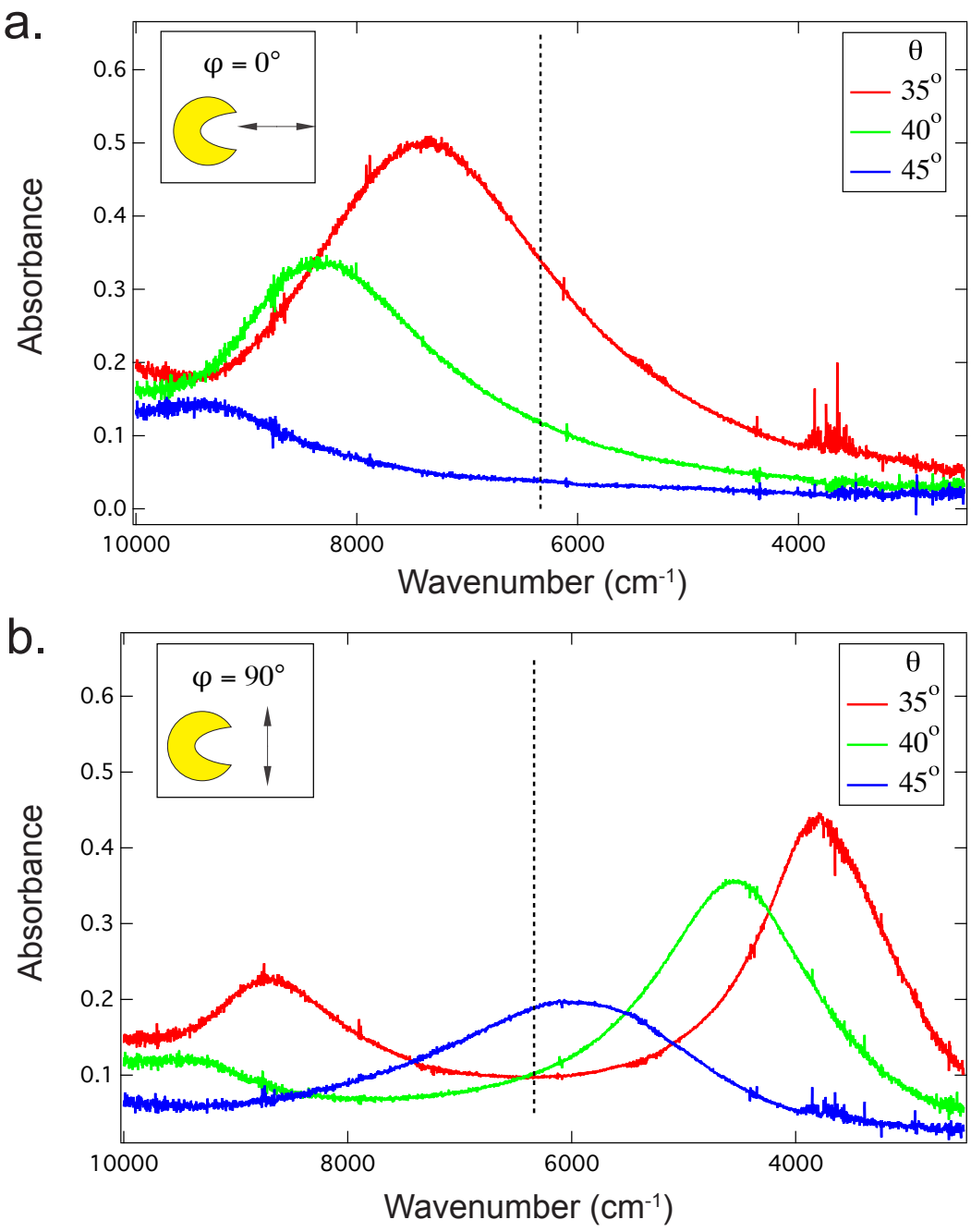

Figure 2.8: Effect of back exposure angle, θ, (i.e., ring opening size; same samples as depicted in Figure 6) on near-infrared absorbance for (a) polarization perpendicular to the opening and (b) polarization across the ring opening. The dotted line indicates the position of the polarization independent plasmonic resonance for an array of fully closed rings.

2.4 Conclusions

In summary, we have expanded the application of our method for fabricating densely packed and well-ordered nanoring arrays over large areas with a combination of colloidal lithography and LPNE to a variety of electrodeposited materials: magnetic (Ni and Co), semiconductor (CdSe), and insulator (PDA). Additionally, we have shown that this nanofabrication process can be modified to create unique asymmetric nanomushrooms, bimetallic core-shell nanorings, and split nanoring arrays. The plasmonic split gold nanoring arrays display polarization dependent absorbances over a broad frequency range (8000 cm^{-1}). By having complete control on the spacing, diameter, ring width, and gap size of these split ring resonators, we can tune the optical properties throughout the near infrared and create dichroic materials in the spectral range from 1 to 5 μm. In addition to their potential use as metamaterials, plasmonic split nanoring arrays can also be used as improved refractive index based biosensor surfaces for detecting nucleic acids and proteins.[9, 20, 22, 39] In the future, split magnetic nanoring can also be created with this fabrication method; split magnetic nanorings have been used to stabilize and alter the magnetic flux closure states of magnetic nanorings with potential applications in high-density magnetic memory storage.[40, 41]

2.5 References

(1) Vaz, C. A.; Klaui, M.; Heyderman, L. J.; David, C.; Nolting, F.; Bland, J. A. Multiplicity of Magnetic Domain States in Circular Elements Probed by Photoemission Electron Microscopy. *Phys. Rev. B* **2005**, *72*, 224426.

(2) Miller, M. M.; Prinz, G. A.; Cheng, S. F.; Bounnak, S. Detection of a Micron-Sized Magnetic Sphere Using a Ring-Shaped Anisotropic Magnetoresistance-Based Sensor: A Model for a Magnetoresistance-Based Biosensor. *Appl. Phys. Lett.* **2002**, *81*, 2211-2213.

(3) Klaui, M.; Vaz, C. A.; Bland, J. A.; Wernsdorfer, W.; Faini, G.; Cambril, E.; Heyderman, L. J. Domain Wall Motion Induced by Spin Polarized Currents in Ferromagnetic Ring Structures. *Appl. Phys. Lett.* **2003**, *83*, 105-107.

(4) Tang, Z.; Kotov, N. A.; Giersig, M. Spontaneous Organization of Single CdTe Nanoparticles into Luminescent Nanowires. *Science* **2002**, *297*, 237-240.

(5) Chen, P.; Chua, S. J.; Wang, Y. D.; Sander, M. D.; Fonstad, C. G. InGaN Nanorings and Nanodots by Selective Area Epitaxy. *Appl. Phys. Lett.* **2005**, *87*, 143111.

(6) Tian, Y.; Sakr, M. R.; Kinder, J. M.; Liang, D.; MacDonald, M. J.; Qiu, R. J.; Gao, H.; Gao, X. P. One-Dimensional Quantum Confinement Effect Modulated Thermoelectric Properties in InAs Nanowires. *Nano Lett.* **2012**, *12*, 6492-6497.

(7) Vayssieres, L.; Sathe, C.; Butorin, S. M.; Shuh, D. K.; Nordgren, J.; Guo, J. One-Dimensional Quantum-Confinement Effect in α-Fe_2O_3 Ultrafine Nanorod Arrays. *Adv. Mater.* **2005**, *17*, 2320-2323.

(8) Willets, K. A.; Van Duyne, R. P. Localized Surface Plasmon Resonance Spectroscopy and Sensing. *Annu. Rev. Phys. Chem.* **2007**, *58*, 267-297.

(9) Huang, C.; Ye, J.; Wang, S.; Stakenborg, T.; Lagae, L. Gold Nanoring as a Sensitive Plasmonic Biosensor for On-Chip DNA Detection. *Appl. Phys. Lett.* **2012**, *100*, 173114.

(10) Larsson, E. M.; Alegret, J.; Kall, M.; Sutherland, D. S. Sensing Characteristics of NIR Localized Surface Plasmon Resonances in Gold Nanorings for Application as Ultrasensitive Biosensors. *Nano Lett.* **2007**, *7*, 1256-1263.

(11) Alu, A.; Engheta, N. Plasmonic and Metamaterial Cloaking: Physical Mechanisms and Potentials. *J. Opt. A: Pure Appl. Opt.* **2008**, *10*, 093002.

(12) Cao, C.; Zhang, J.; Wen, X.; Dodson, S. L.; Dao, N. T.; Wong, L. M.; Wang, S.; Li, S.; Phan, A. T.; Xiong, Q. Metamaterials-Based Label-Free Nanosensor for Conformation and Affinity Biosensing. *ACS Nano* **2013**, *7*, 7583-7591.

(13) Anker, J. N.; Hall, W. P.; Lyandres, O.; Shah, N. C.; Zhao, J.; Van Duyne, R. P. Biosensing with Plasmonic Nanosensors. *Nat. Mater.* **2008**, *7*, 442-453.

(14) Wang, H.; Brandl, D. W.; Nordlander, P.; Halas, N. Plasmonic Nanostructures: Artificial Molecules. *Acc. Chem. Res.* **2007**, *40*, 53-62.

(15) Liu, N.; Weiss, T.; Mesch, M.; Langguth, L.; Eigenthaler, U.; Hirscher, M.; Sonnichsen, C.; Giessen, H. Planar Metamaterial Analogue of Electromagnetically Induced Transparency for Plasmonic Sensing. *Nano Lett.* **2010**, *10*, 1103-1107.

(16) Heyderman, L. J.; David, C.; Klaui, M.; Vaz, C. A.; Bland, J. Nanoscale Ferromagnetic Rings Fabricated by Electron-Beam Lithography. *J. Appl. Phys.* **2003**, *93*, 10011-10013.

(17) Shelby, R. A.; Smith, D. R.; Schultz, S. Experimental Verification of a Negative Index of Refraction. *Science* **2001**, *292*, 77-79.

(18) Linden, S.; Enkrich, C.; Wegener, M.; Zhou, J.; Koschny, T.; Soukoulis, C. M. Magnetic Response of Metamaterials at 100 Terahertz. *Science* **2004**, *306*, 1351-1353.

(19) Bochenkov, V. E.; Sutherland, D. S. From Rings to Crescents: A Novel Fabrication Technique Uncovers the Transition Details. *Nano Lett.* **2013**, *13*, 1216-1220.

(20) Clark, A. W.; Glidle, A.; Cumming, D. R.; Cooper, J. Plasmonic Split-Ring Resonators as Dichroic Nanophotonic DNA Biosensors. *J. Am. Chem. Soc.* **2009**, *131*, 17615-17619.

(21) Bukasov, R.; Ali, T. A.; Nordlander, P.; Shumaker-Parry, J. S. Probing the Plasmonic Near-Field of Gold Nanocrescent Antennas. *ACS Nano* **2010**, *4*, 6639-6650.

(22) Bukasov, R.; Shumaker-Parry, J. S. Highly Tunable Infrared Extinction Properties of Gold Nanocrescents. *Nano Lett.* **2007**, *7*, 1113-1118.

(23) Lewicka, Z. A.; Li, Y.; Bohloul, A.; Yu, W. Y.; Colvin, V. L. Nanorings and Nanocrescents Formed via Shaped Nanosphere Lithography: A Route Toward Large Areas of Infrared Metamaterials. *Nanotechnology* **2013**, *24*, 115303-115313.

(24) Cataldo, S.; Zhao, J.; Neubrech, F.; Frank, B.; Zhang, C.; Braun, P. V.; Giessen, H. Hole-Mask Colloidal Nano Lithography for Large-Area Low-Cost Metamaterials and Antenna-Assisted Surface-Enhanced Infrared Absorption Substrates. *ACS Nano* **2012**, *6*, 979-985.

(25) Bukasov, R.; Shumaker-Parry, J. S. Silver Nanocrescents with Infrared Plasmonic Properties as Tunable Substrates for Surface Enhanced Infrared Absorption Spectroscopy. *Anal. Chem.* **2009**, *81*, 4531-4535.

(26) Liu, G. L.; Lu, Y.; Kim, J.; Doll, J. C.; Lee, L. P. Magnetic Nanocrescents as Controllable Surface-Enhanced Raman Scattering Nanoprobes for Biomolecular Imaging. *Adv. Mater.* **2005**, *17*, 2683-2688.

(27) Clark, A. W.; Sheridan, A. K.; Glidle, A.; Cumming, D.; Cooper, J. Tuneable Visible Resonances in Crescent Shaped Nano-Split-Ring Resonators. *Appl. Phys. Lett.* **2007**, *91*, 093109.

(28) Rockstuhl, C.; Zentgraf, T.; Guo, H.; Liu, N.; Etrich, C.; Loa, I.; Syassen, K.; Kuhl, J.; Lederer, F.; Giessen, H. Resonances of Split-Ring Resonator Metamaterials in the Near Infrared. *Appl. Phys. B* **2006**, *84*, 219-227.

(29) Pearson, D. H.; Tonucci, R. J. Nanochannel Glass Replica Membranes. *Science* **1995**, *270*, 68-70.

(30) Pearson, D. H.; Tonucci, R. J. Parallel Patterning with Nanochannel Glass Replica Membranes. *Adv. Mater.* **1996**, *8*, 1031-1034.

(31) Zhang, G.; Wang, D. Colloidal Lithography-The Art of Nanochemical Patterning. *Chem. Asian J.* **2009**, *4*, 236-245.

(32) Lusker, K. L; Li, J. R.; Garno, J. C. Nanostructures of Functionalized Gold Nanoparticles Prepared by Particle Lithography with Organosilanes. *Langmuir* **2011**, *27*, 13269-13275.

(33) Halpern, A. R.; Corn, R. M. Lithographically Patterned Electrodeposition of Gold, Silver, and Nickel Nanoring Arrays with Widely Tunable Near-Infrared Plasmonic Resonances. *ACS Nano* **2013**, *7*, 1755-1762.

(34) Kumar, S.; Kumar, R.; Chakarvarti, S. K. Morphological and Magnetic Characterization of Electrodeposited Cobalt Nanowires. *J. Mater. Sci.* **2004**, *39*, 2951-2953.

(35) Loget, G.; Wood, J. B.; Cho, K.; Halpern, A. R.; Corn, R. M. Electrodeposition of Polydopamine Thin Films for DNA Patterning and Microarrays. *Anal. Chem.* **2013**, *85*, 9991-9995.

(36) Sheridan, A. K.; Clark, A. W.; Glidle, A.; Cooper, J. M.; Cumming, D. R. Multiple Plasmon Resonances from Gold Nanostructures. *Appl. Phys. Lett.* **2007**, *90*, 143105.

(37) Rockstuhl, C.; Lederer, F.; Etrich, C.; Zentgraf, T.; Kuhl, J.; Giessen, H. On the Reinterpretation of Resonances in Split-Ring-Resonators at Normal Incidence. *Opt. Express* **2006**, *14*, 8827-8836.

(38) Gwinner, M. C.; Koroknay, E.; Fu, L.; Patoka, P.; Kandulski, W.; Giersig, M.; Giessen, H. Periodic Large-Area Metallic Split-Ring Resonator Metamaterial Fabrication Based on Shadow Nanosphere Lithography. *Small* **2009**, *5*, 400-406.

(39) Liu, S. D.; Zhang, Z. S.; Wang, Q. Q. High Sensitivity and Large Field Enhancement of Symmetry Broken Au Nanorings: Effect of Multipolar Plasmon Resonance and Propagation. *Opt. Express* **2009**, *17*, 2906-2917.

(40) He, K.; Smith, D. J.; McCartney, M. R. Direct Visualization of Three-Step Magnetization Reversal of Nanopatterned Spin-Valve Elements Using Off-Axis Electron Holography. *Appl. Phys. Lett.* **2009**, *94*, 172503.

(41) Madami, M.; Bisero, D.; Gubbiotti, G.; Tacchi, S.; Carlotti, G.; Nakano, K.; Ono, T. Magnetization Configurations in NiFe Slotted Rings Studied by Magneto-Optical Kerr Effect and Magnetic Force Microscopy. *IEEE Trans. Magn.* **2012**, *48*, 1269-1272.

Chapter 3

Gold Nanoring Arrays for Near-Infrared Plasmonic Biosensing

3.1 Introduction

Surface plasmon resonance (SPR) measurement based on the excitation of propagating surface plasmon polaritons on planar metallic surfaces is a well-established and sensitive biosensing method for the detection of surface bioaffinity interactions and the quantitative analysis of target proteins and nucleic acids with applications to the fields of medical diagnostics, food safety, and environmental monitoring.[1, 2] Localized surface plasmon resonance (LSPR) measurement based on the excitation of localized surface plasmons on nanostructured metal surfaces is an alternative biosensing method that is easily incorporated into a simple

absorption spectroscopy format; LSPR measurements have been suggested as a potentially higher sensitivity detection method than SPR.[3, 4]

In a typical LSPR biosensor, the binding of target biomolecules onto metal nanostructured surfaces is detected as a shift in resonant wavelength in the absorption spectrum. The plasmonic properties which determine the sensitivity of LSPR biosensors highly depend on the geometry of the metal nanostructures;[4, 5] arrays of nanoparticles,[6, 7] nanocubes,[8, 9] nanopyramids,[10] nanodisks,[11, 12] nanorods,[13-15] and nanorings[16-18] have all been employed as LSPR biosensor surfaces. Metallic nanoring arrays have emerged as one of the most promising nanostructured surfaces due to their unique plasmonic properties and potential for enhanced refractive index sensitivity.[16, 19] Previous studies have revealed that the resonant wavelength and refractive index sensitivity of the nanoring LSPR biosensors depend critically on the spacing, diameter, and width of the nanorings.[16, 19, 20] A variety of sequential methods for fabricating metallic nanorings such as electron beam lithography[18] and nanoimprint lithography[19] have been explored. These methods offer excellent geometric control of the nanoring array dimensions but are limited in the total area that the nanostructures can be created. Methods that employ colloidal or nanosphere lithography have been used to create nanoring arrays over larger surface areas, but the geometric control of the diameter and width of the nanorings has been limited with these fabrication methods.[16, 17, 21]

Recently, we have developed a new method for fabricating metallic nanoring arrays over large surface areas that uses a combination of colloidal lithography and lithographically patterned nanoscale electrodeposition (LPNE), as shown schematically in Figure 3.1.[22] This new method can be used to create periodically ordered gold nanoring (Au nanoring) arrays over large surface areas with excellent control of the nanoring diameter, width, and spacing.[22] The Au

nanoring arrays created by this process exhibit strong and tunable LSPR absorption bands at the NIR wavelengths from 1.0 to 2.5 μm with narrow bandwidths that are potentially useful for refractive index biosensing measurements.

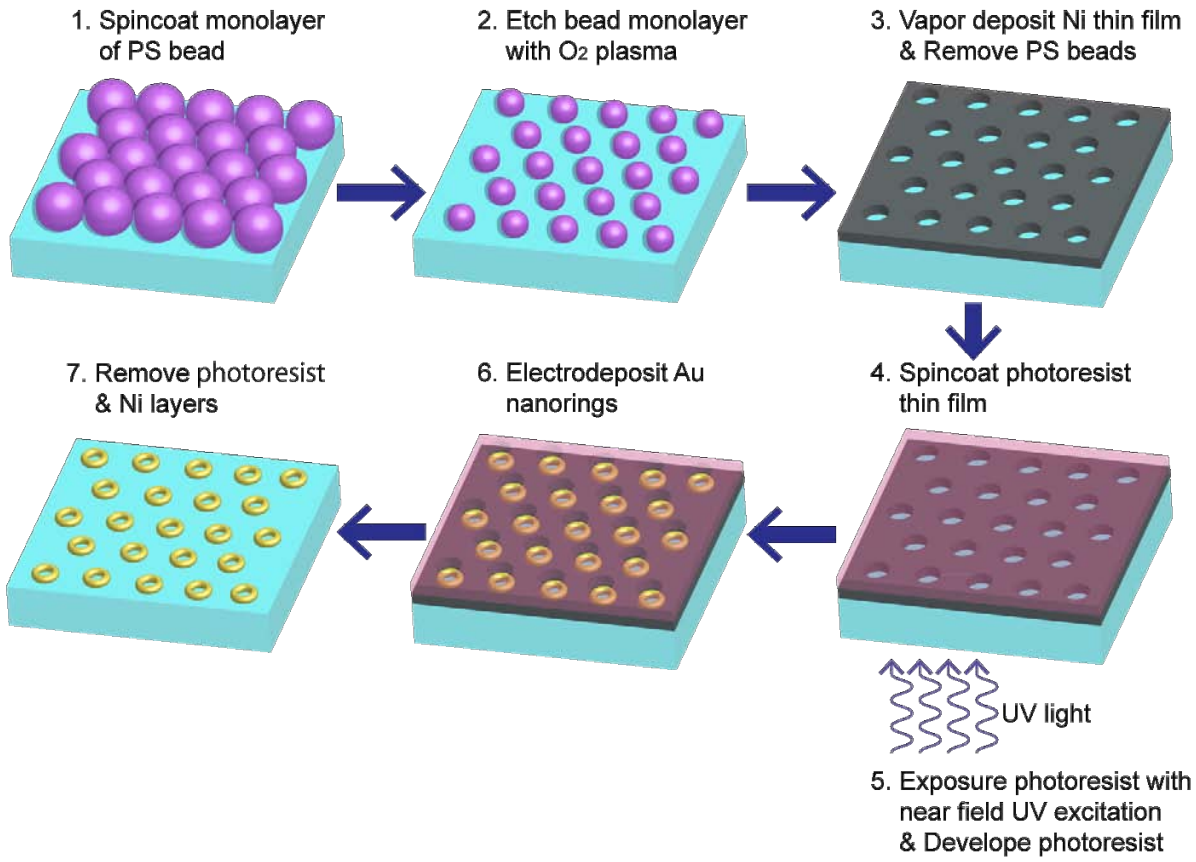

Figure 3.1: Fabrication process of lithographically patterned electrodeposition of Au nanoring arrays.

In this paper, the refractive index sensitivity of a series of Au nanoring arrays with various nanoring dimensions created by this LPNE process is reported. Real-time Fourier transform near infrared (FT-NIR) transmittance measurements were used to determine a bulk refractive index sensitivity of 3,780 cm^{-1}/refractive index unit (RIU) for LSPR measurements of nanoring arrays. A series of real-time, in situ FT-NIR transmittance measurements were then used to monitor the polymerization of dopamine to form a multilayer film of polydopamine on

the nanoring sensor surface. In a third LSPR experiment, the hybridization adsorption of DNA-functionalized gold nanoparticles (AuNPs) onto Au nanoring array surfaces modified with complementary DNA was characterized. The sensitivity of DNA detection with these nanoring arrays was estimated by monitoring the hybridization adsorption of DNA-functionalized AuNPs onto mixed DNA monolayers that only contain a small percentage of complementary DNA on the Au nanorings. The quantitative analysis of LSPR shifts induced by adsorption of DNA-modified AuNPs onto the nanorings revealed that the lowest detectable surface coverage of complementary DNA on Au nanoring arrays is 0.5% of a monolayer, which corresponds to the relative surface coverage of DNA that would be created by exposure to a 50 pM DNA solution.

3.2 Materials and Methods

3.2.1 Materials

Carboxylate-coated polystyrene (PS) beads solutions (2.6 % w/v, 1 μm or 0.75 μm diameter) were obtained from Polysciences. Shipley S1808 photoresist, Thinner P, and MF-319 developer were purchased from Microchem. Clean Earth Chemicals 24-K gold plating solution was obtained from Grobet USA. 11-amino-1-undecanethiol hydrochloride (MUAM) was purchased from Dojindo (Japan). 1-ethyl-3-(3-(dimethylamino)propyl)carbodiimide hydrochloride (EDC) and N-hydroxysulfosuccinimide (Sulfo-NHS) were obtained from Thermo Scientific. Poly(l-glutamic acid) sodium salt (pGlu) and dopamine hydrochloride were obtained from Sigma. Three single-stranded DNA (ssDNA) sequences were purchased from Integrated DNA Technologies. The sequences are denoted A, Ac, and B:

A = 5'-NH_2-$(CH_2)_{12}$-CGAAATCCAGACACATAAGCACGAACCGAA-3'

Ac = 5'-TTCGGTTCGTGCTTATGTGTCTGGATTTCG-$(CH_2)_{12}$-SH-3′

B = 5'-NH_2-$(CH_2)_{12}$-$(T)_{30}$-3'.

All the chemicals were used as received.

3.2.2 Preparation of DNA-modified Gold Nanoparticles

AuNPs with a diameter of 13 nm were synthesized by citrate reduction based on the Turkevich Method.[23] Briefly, $HAuCl_4$ (0.0223 g, 0.0656 mmol) was dissolved in 100 mL water. Sodium citrate dihydrate (0.0533 g, 0.1812 mmol, in 5 mL water) was then injected to the boiling solution. After a color change (from blue to red) was observed, the solution was allowed to react for 10 min. AuNPs solution (1 mL) was filtered (0.22 μm) prior to the addition of 1 mM thiol-terminated ssDNA (5 μL, in phosphate-buffered saline (PBS) buffer). After the mixture was kept at 37 °C for 24 h, 500 μL of PBS buffer was added to the solution. The solution was kept at 37 °C for another 24 h to complete the ligand exchange reaction. Two centrifugation cycles (13,000 rpm, 15 min) were applied to remove the excess ssDNA in the solution, followed by removal of supernatant and resuspension in PBS buffer. The concentration of AuNPs was measured by UV–vis spectroscopy with an extinction coefficient of 2.7×108 M^{-1} cm^{-1} at λ_{max} = 520 nm and adjusted to approximately 2.5 nM.

3.2.3 Preparation of Au Nanoring Arrays

The detailed process for lithographically patterned electrodeposition of Au nanoring arrays has been described in our previous work.[22] First, a solution containing PS beads (5 % w/v in mixture of water and MeOH with mix ratio of 1:3) was spin-coated on cleaned BK7 glass and close-packed colloidal monolayer was formed as the solvent dried, shown in Figure 3.1a. The size of PS beads was reduced by O_2 plasma treatment (South Bay Technologies) at 200 mTorr

and 50 W (Figure 3.1b). The etching time was set between 3.5 and 6 min to control the size of PS beads. The sacrificial electrode with nanohole arrays was created by deposition of a 70 nm thick Ni layer on top of the shrunk PS beads monolayer by a thermal evaporator (DV-502A, Denton Vacuum), followed by removal of PS beads with ultra-sonication in toluene for 10 min (Figure 3.1c). Shipley S1808 photoresist (diluted to 1:1 with Thinner P) was spin-coated on top of the substrate in order to protect the surface of the sacrificial Ni layer. After spin-coating photoresist, the substrate was baked in an oven for 15 min at 90 °C. Subsequently, the photoresist was exposed to the UV light from the backside with an exposure dose of 30 mW/cm^2 (see Figure 3d-e) and developed by MF-319 developer. Au nanorings were formed inside the Ni nanohole arrays by electrodeposition of Au using a potentiostat (PGSTAT12, Metrohm), shown in Figure 3.1f. The potential and plating time were set to −0.85 V and 450 to 650 s, respectively. The width of the ring was controlled by the plating time. Finally, the sacrificial Ni layer was removed by immersing the substrate in 0.8 M nitric acid for 10 min (Figure 3.1g). Before use, the substrates were annealed in a furnace for 45 min at 400 °C in order to smooth the surface of Au nanorings.

3.2.4 DNA Attachment onto Au Nanorings

ssDNA was attached onto the surface of Au nanorings by using pGlu attachment chemistry as described in our previous work.[24] Briefly, MUAM monolayer was formed on the Au nanorings by immersing the substrate in a 1 mM MUAM solution in ethanol overnight. The substrate was rinsed with ethanol followed by water and dried under nitrogen stream. The pGlu layer was formed by exposing the substrate to a 2 mg/ml pGlu solution in PBS for 1 h. Amino-terminated ssDNA was immobilized to pGlu monolayer by exposing the substrate to 250 μM

DNA in PBS containing 75 mM EDC and 15 mM Sulfo-NHS for 5 h. The substrate was then rinsed with water and dried under nitrogen stream after pGlu attachment and DNA immobilization.

3.2.5 FT-NIR Measurements

Near IR absorption spectra were taken by a Mattson RS-1 FT-IR spectrometer. Spectra in the near infrared region (3,000 – 12,000 cm^{-1}) were collected with 100 scans and 4 cm^{-1} resolution. For the in situ measurement, a flow cell with a volume of 30 µl was attached to the substrate and the sample solution was flowed over the sensor surface by using a peristaltic pump.

3.2.6 SEM Observation

The shape and density of Au nanoring arrays were characterized by SEM (Magellan400 XHR SEM or Phillips XL-30 FEG SEM). The image analysis was carried out by using ImageJ (US National Institutes of Health) and Mathematica to characterize the nanoring dimensions.[22]

3.3 Results and Discussion

3.3.1 Characterization of Au Nanoring Arrays

A set of Au nanoring arrays were prepared, and their plasmonic properties were investigated. Figure 3.2a is a typical photograph of an Au nanoring array on a glass substrate which shows that the Au nanoring arrays uniformly covered the surface of glass slides with the dimension of 2.5×2.5 cm^2. The SEM image shown in Figure 3.2b revealed that the Au nanoring arrays consisted of multiple domains of two-dimensional hexagonal close-packed crystalline Au nanorings. The size of a single domain was approximately 10 to 30 μm. Defects of the structure such as merged rings, vacancies, and disordered structures were sometimes observed at the border of the domains. The inserted picture in Figure 3.2b is the enlarged image of the single domain of the Au nanoring array. Figure 3.2c shows a schematic of the Au nanoring arrays. In the following, we define the structure of the Au nanoring arrays by the distance between the centers of the neighboring nanoring L, the diameter d, and the width w of the ring. The distance L is controlled by the size of the PS beads. The diameter is determined by the etching time of PS beads. The width and height can be varied by the plating time of Au.

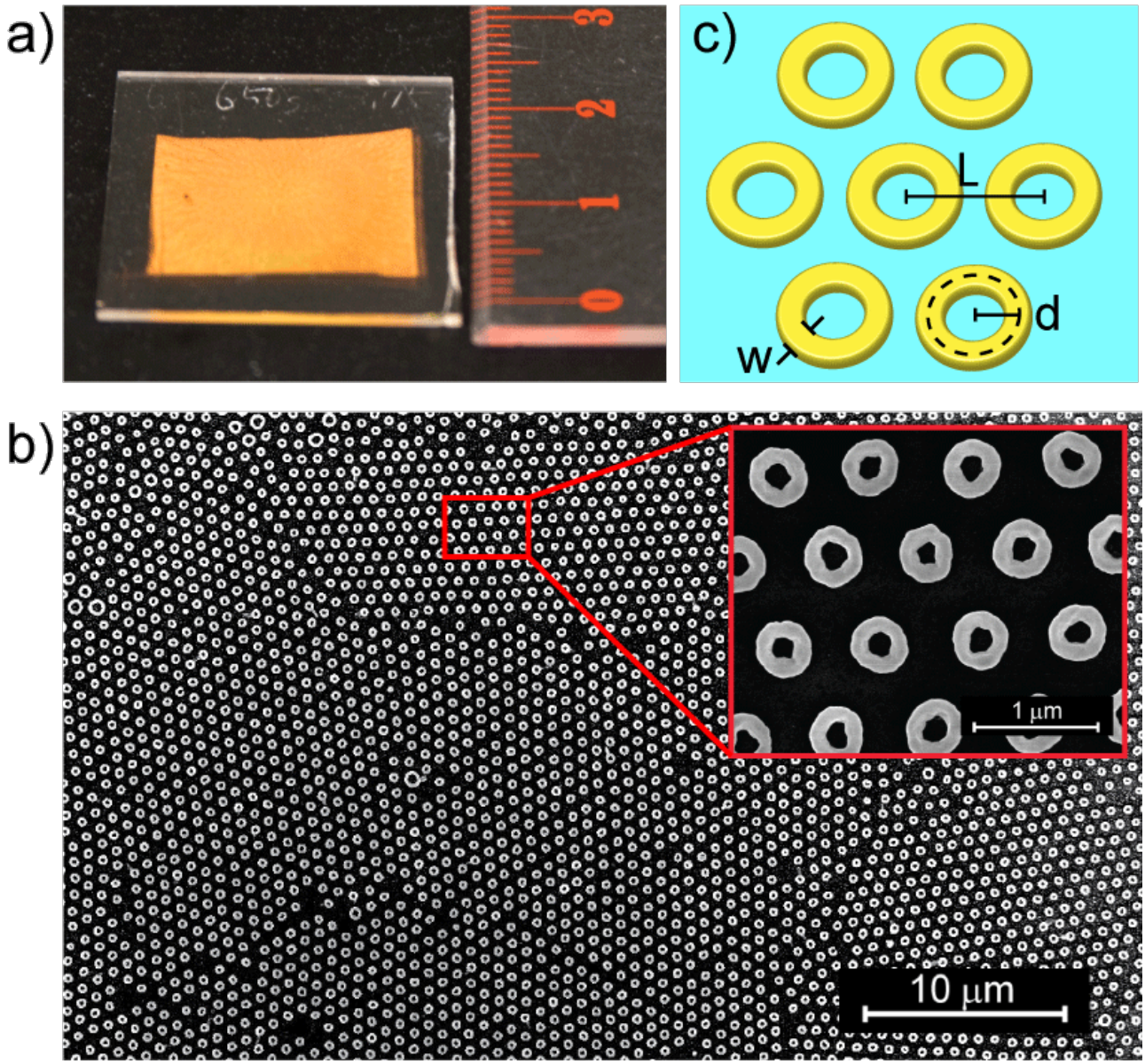

Figure 3.2: (a) A representative photograph and (b) a SEM image of Au nanoring arrays on glass substrate. The inserted picture in SEM image is the enlarged image. (c) Schematic of the Au nanoring arrays with period L, diameter d, and width w.

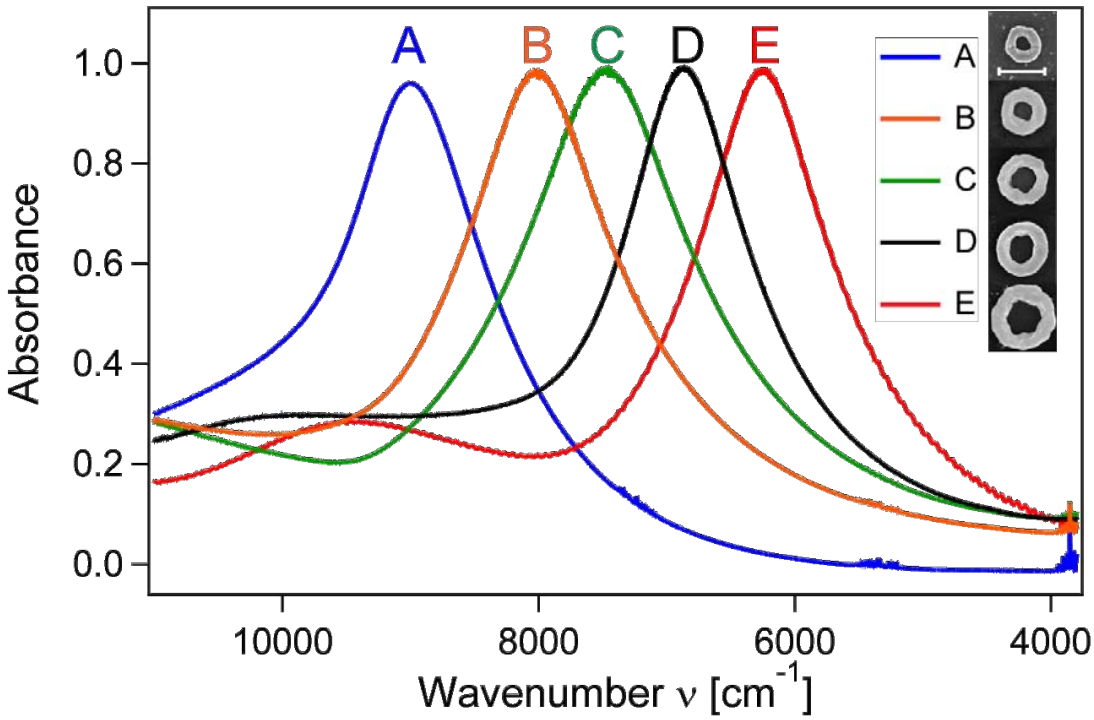

Figure 3.3: Near IR absorption spectra of Au nanoring arrays in air. The inserted SEM images show the typical Au nanorings observed from each sample. The scale bar is 500 nm.

The plasmonic properties of Au nanoring arrays with various diameter d and width w were characterized by FT-NIR spectroscopy. Figure 3.3 shows a set of near IR transmission absorption spectra of five Au nanoring arrays taken in air. The inserted pictures in the graph show typical SEM images of the nanorings. The absorption spectrum of sample E exhibited one strong absorption peak at 6,000 cm^{-1} and one weak absorption peak at 9,500 cm^{-1} associated with bonding mode and antibonding mode, respectively, in agreement with previous studies.[18, 20] In this paper, we have used the strong absorption peak of the bonding mode for the refractive index sensing. The prepared samples exhibited strong absorption peaks in the wide wavenumber range from 6,000 to 9,000 cm^{-1} with similar bandwidths. This wavenumber range corresponds to a wavelength range from 1.6 to 1.1 μm. The mean diameter and width of each sample were obtained from the average of over 100 nanorings in SEM pictures and were summarized in Table

3.1. The mean diameter of the nanoring was efficiently controlled over 100 nm by changing both plasma etching time and the size of PS beads. Samples A, B, and C were fabricated with 0.75 μm PS beads, and samples D and E were fabricated with 1 μm PS beads. The resonance absorption maximum shifted to higher wavenumber as the diameter of the nanoring was decreased. This trend agrees with theoretical and experimental results in previous studies.[21, 22]

Table 3.1 Dimensions, peak wavenumber, and bulk refractive index sensitivity of the samples shown in Figure 3.3

	Distance *L* [nm]	Diameter *d* [nm]	Width *w* [nm]	Peak wavenumber n_{max} [cm^{-1}]	Sensitivity [cm^{-1}/RIU(nm/RIU)]
A	750	146±8	124±6	8995	-3780 (805)
B	750	187±7	150±5	8015	-3447 (941)
C	750	204±-7	133±6	7472	-3238 (1023)
D	1000	213±10	150±6	6867	-2549 (960)
E	1000	262±10	172±7	6250	-2413 (1006)

3.3.2 Bulk Refractive Index Sensitivity Measurements

The sensitivity of LSPRs of the Au nanoring arrays to changes in bulk refractive index was characterized by measuring shifts in the LSPR absorption peaks upon exposure of the Au nanoring arrays to solutions with different refractive indexes. The refractive index of the solution was changed by mixing water and ethanol with different mixture ratio (H_2O/EtOH = 1:0, 3:1, 1:1, and 0:1). As the refractive indexes of water and ethanol exhibit a wavelength dependence,

the refractive index of the sample solution at the resonance wavenumber was calculated from the Cauchy's constants of water and ethanol.[25] In order to eliminate the strong absorption peaks from the water and ethanol in the near IR region, a reference spectrum was taken with the sample solution without Au nanoring arrays. Figure 3.4a shows the changes in the absorption spectra of sample A when the sample was in contact with air (red curve), water (light blue curve), and ethanol (blue curve). The resonance wavenumber exhibited a large shift to lower wave numbers as the bulk refractive index increased without dramatic changes in the shape and the peak absorbance of the resonance curve. The peak wavenumber was determined by fitting the absorption spectra with Lorentzian function. Figure 3.4b plots the relative peak shift against the refractive index of the sample solution for the nanorings with various sizes shown in Figure 3.3. All samples showed a linear dependence of the peak shift to bulk refractive indexes. The bulk refractive index sensitivity was obtained from the slope of the fitted curves. The sensitivities of sample A to E resulted in 3,780 to 2,700 cm^{-1}/RIU, respectively. As listed in Table 3.1, these sensitivities correspond to 805 to 1,020 nm/RIU in wavelength. The wavelength sensitivity agrees with the tendency that the sensitivity increases as resonance wavelength increases and relative width (w/d) decreases, as reported by Larsson et al.[16] Our nanoring arrays exhibited enhanced sensitivities as compared to other metallic nanoring reported previously.[16, 18] Furthermore, these sensitivities were comparable to the state of the art refractive index LSPR sensors with more complicated nanostructures.[26, 27]

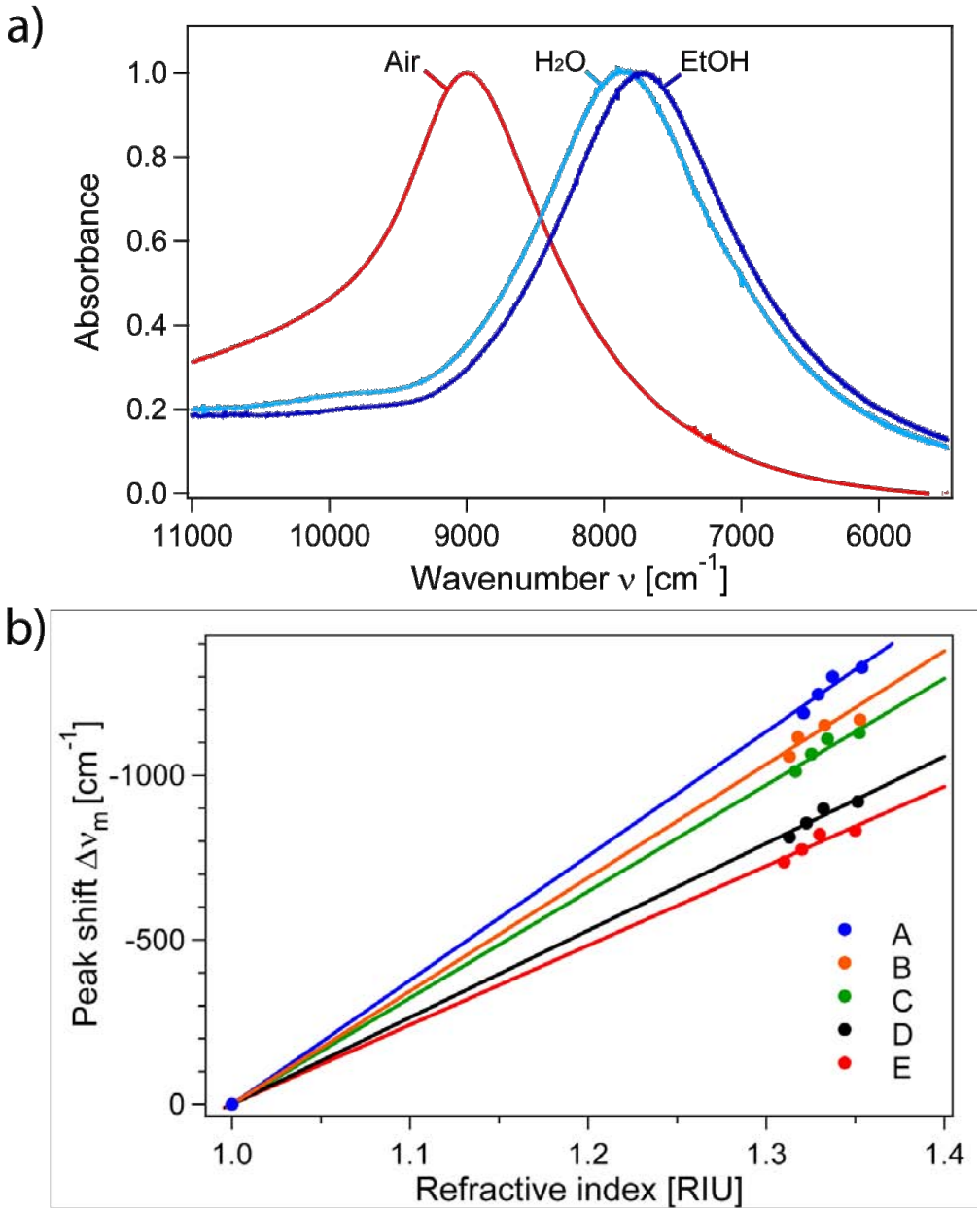

Figure 3.4: (a) Absorption spectra of sample A in contact with air (red curve), water (light blue curve), and ethanol (blue curve). (b) Correlation curves between the peak shifts Δν m and bulk refractive indexes.

3.3.3 Real-time Observation of Surface Polymerization of Dopamine

The polymerization process of dopamine at the surface of Au nanorings was monitored by real-time, in situ measurements of LSPR peak shifts. Polydopamine is a biomimetic adhesive

polymer inspired by marine mussel foot proteins.[28] Polydopamine coating methods have attracted great attention due to the fact that they can be applied to any kind of surface by exposure to an alkaline dopamine solution. The coated thin polydopamine layer can serve as binding agent for biomolecules containing amino or thiol functional groups.[29] Characterization of polymerization process of dopamine is one of the key aspects requiring for the control of surface functionalization with polydopamine.[30] In this experiment, a sample solution containing 5 mg/ml dopamine in PBS buffer at pH 7.4 was used to create a polydopamine layer onto Au nanoring sensor surface as schematically illustrated in Figure 3.5a. The dopamine solution was flowed over the sensor surface for 30 min, and then the surface was rinsed with PBS for 10 min. This cycle was repeated three times. A series of FT-NIR absorption spectra were taken every 3 min, and the LSPR peak wavenumber ν m was plotted as a function of time (see Figure 3.5b). First, a baseline was obtained with the sensor surface in contact with PBS solution. When the dopamine solution was introduced, the peak wavenumber jumped to lower wavenumber, which is attributed to a bulk refractive index change around the Au nanorings. Subsequently, the peak wavenumber exhibited a constant shift to lower wavenumbers, indicating that dopamine molecules were polymerizing and adsorbing to form a polydopamine layer at the sensor surface. After the sensor surface was rinsed with PBS buffer, the peak wavenumber increased slightly and reached a plateau. This decrease in peak wavenumber is attributed to the increase of local refractive index by accumulation of polydopamine layers on the sensor surface.

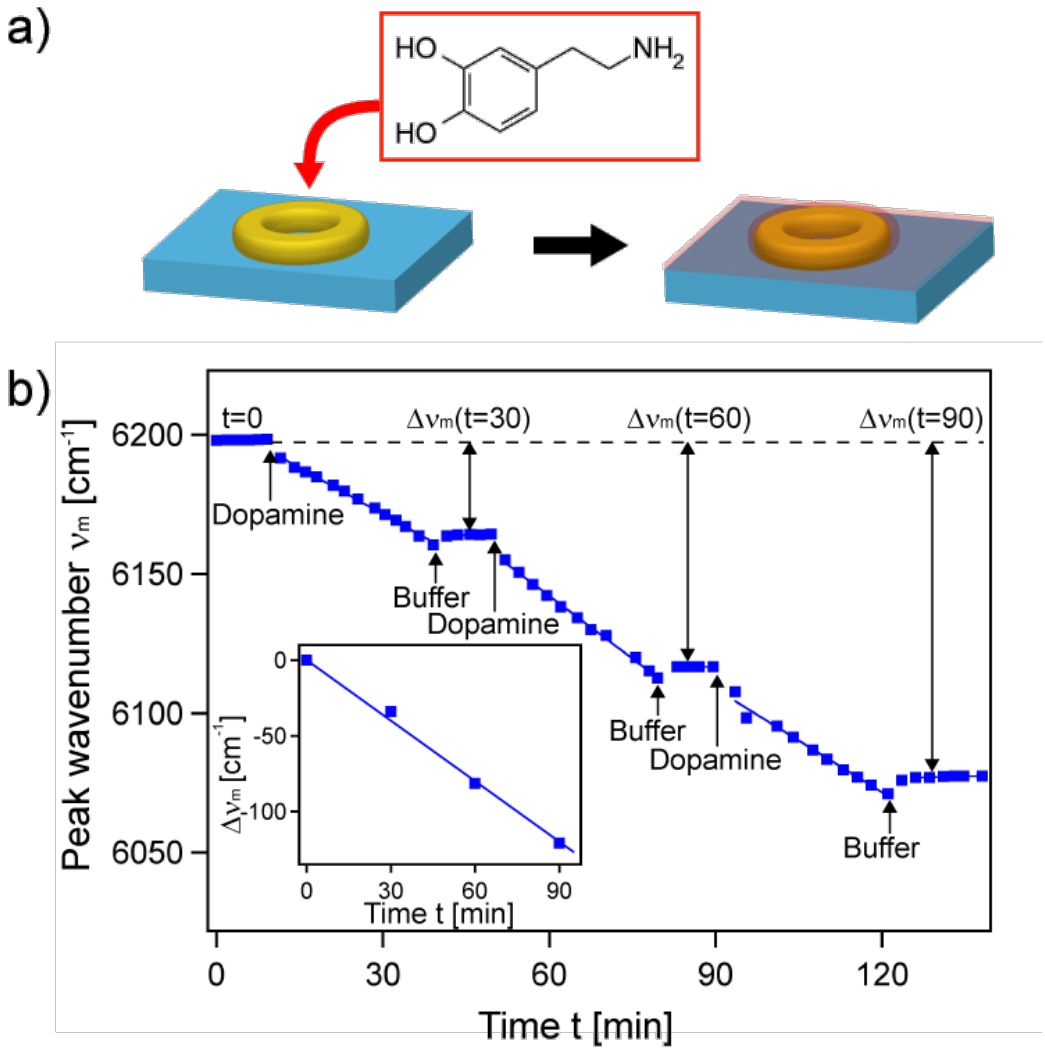

Figure 3.5: (a) Schematic of adsorption of polydopamine multilayers onto Au nanorings. (b) Real-time in situ measurement of peak wavenumber ν m upon polymerization of dopamine in a solution and its accumulation onto the Au nanoring arrays. The inserted graph shows the linear correlation between the peak shift Δν m and film growth time.

The inserted figure in Figure 3.5b plots the peak shifts Δν m observed in PBS after multiple exposures to dopamine solutions. The peak shifts due to the polydopamine multilayer growth were increased linearly with time and were reached as large as 120 cm^{-1} after 90 min exposure. This observation agrees well with our recent SPR imaging study of the polymerization of dopamine on flat Au thin films.[30] These results indicate that these near IR LSPR nanoring

sensors are suitable for in situ monitoring of the adsorption of multilayer polymer films onto the sensor surfaces in real time.

3.3.4 Detection of DNA Hybridization Adsorption

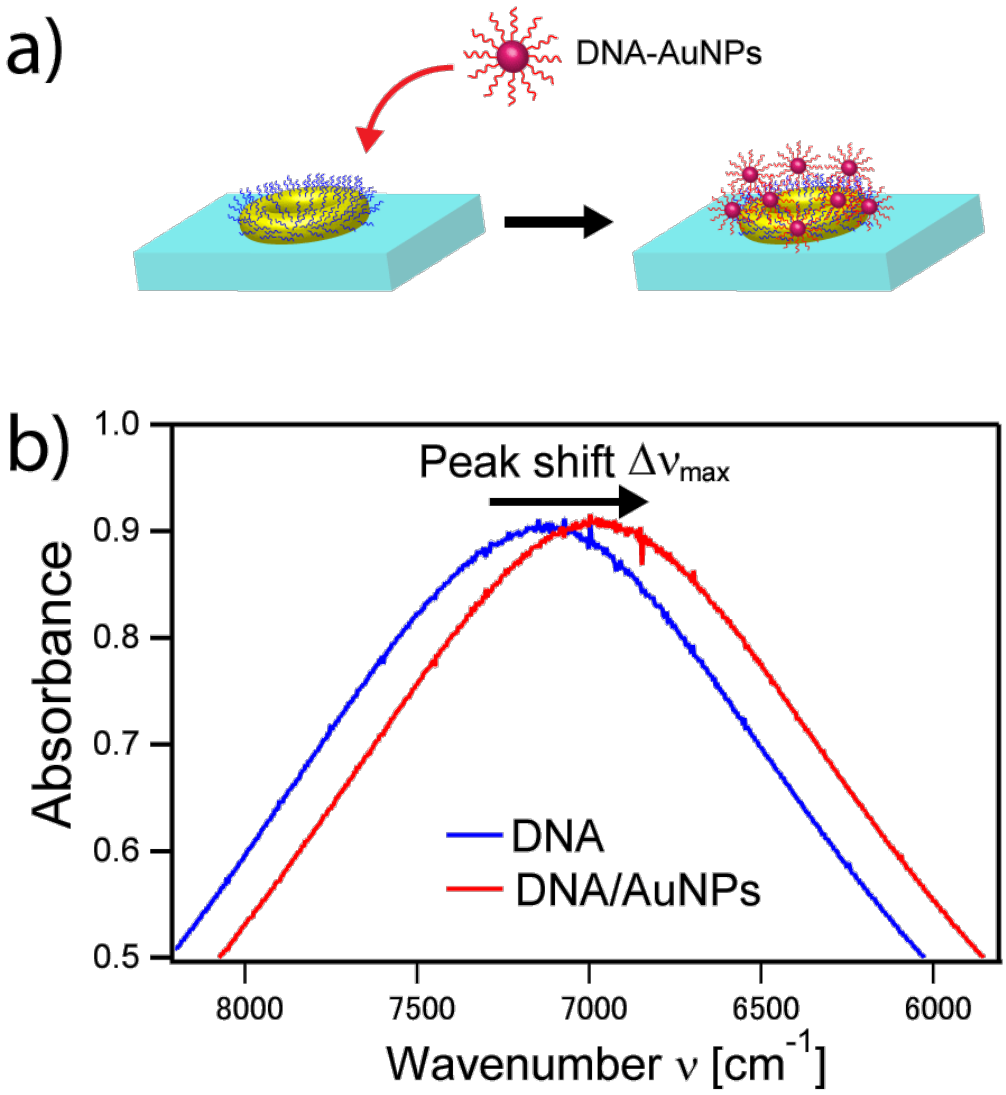

Figure 3.6: Detection of DNA hybridization adsorption of AuNPs modified with ssDNA onto Au nanoring surface. (a) Schematic image of the sample. AuNPs functionalized with ssDNA (sequence Ac) bind to Au nanorings modified with a complementary DNA (sequence A) monolayer through DNA hybridization adsorption. (b) FT-NIR absorption spectra before (blue curve) and after (red curve) DNA–AuNPs adsorption.

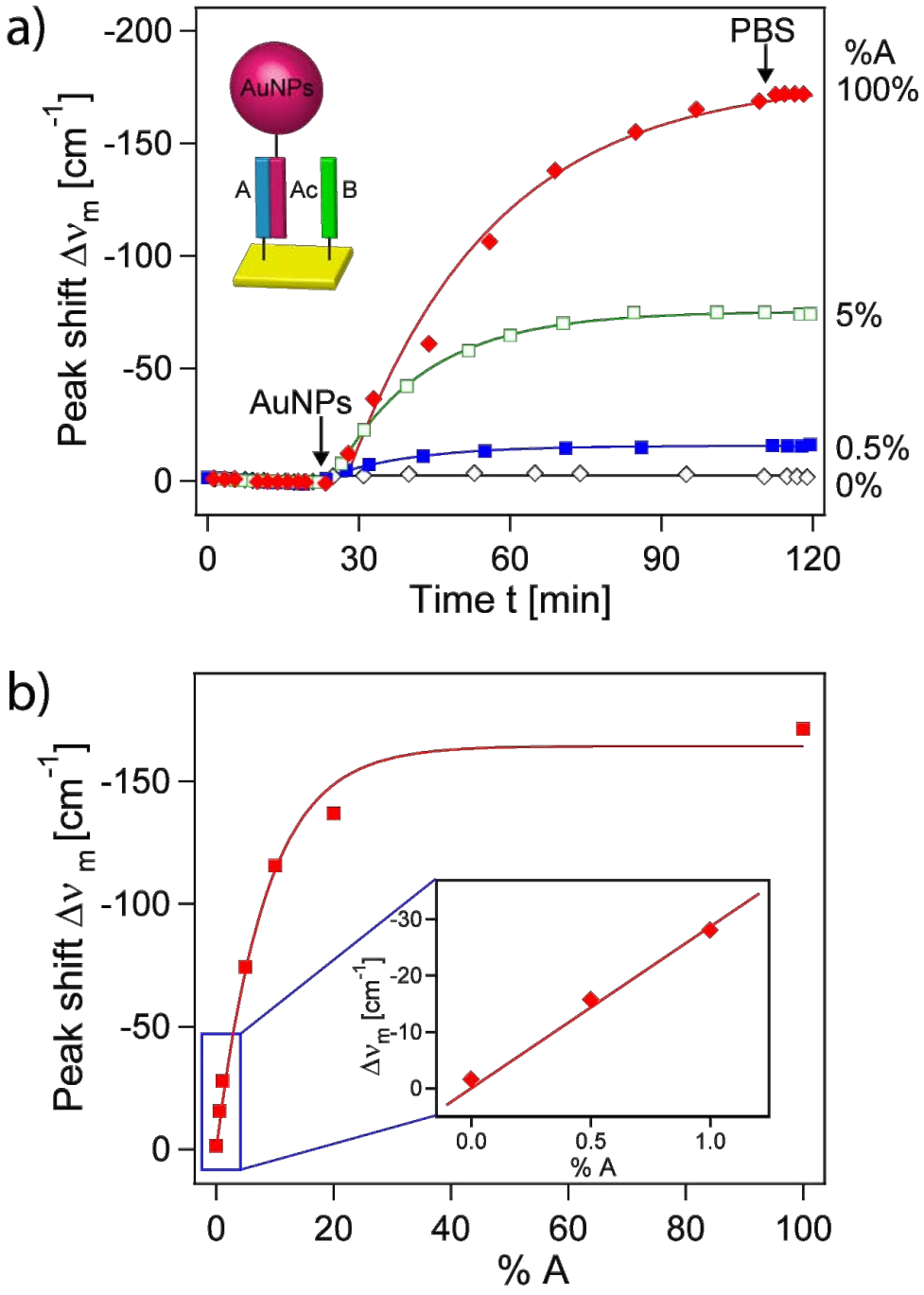

Figure 3.7: (a) Real-time, in situ measurement of adsorption of DNA–AuNPs onto Au nanorings functionalized with complementary ssDNA with different relative surface coverage (%A = 100, 5, 0.5, and 0 %). (b) Quantitative plot of peak shift Δν m as a function of %A. The peak shifts were obtained after the surface was rinsed with PBS buffer. The inserted figure is the enlarged plot where %A is below 1 %.

In a third set of experiments, the DNA hybridization of AuNPs modified with ssDNA onto the Au nanoring arrays were detected with the near IR LSPR shift measurements.[30 31] In this experiment, the surfaces of Au nanorings were functionalized with ssDNA by using pGlu attachment chemistry used previously.[24] The adsorption of AuNPs modified with complementary DNA (DNA–AuNPs) was monitored as the shift in resonance wavenumber as schematically illustrated in Figure 3.6a. Figure 3.6b shows the FT-NIR spectra of the Au nanorings in PBS before and after binding of DNA–AuNPs to the DNA monolayer attached on the Au nanorings. The peak wavenumber exhibited a large shift of over 150 cm^{-1} after AuNPs adsorption.

A series of measurements of the hydridization adsorption of AuNPs onto partially complementary ssDNA monolayer was used to estimate the detection limit of ssDNA with LSPR on these nanoring arrays. In this experiment, Au nanoring arrays were functionalized with a mixture of two amino-terminated ssDNA (sequences A and B) at various A/B percentages of 100:0, 20:80, 10:90, 5:95, 1:99, 0.5:99.5, and 0:100. By assuming an equivalent surface reactivity of both ssDNA, the percentage of sequence A at the surface was controlled by the mixture ratio of A and B in the solution. In order to minimize the differences in sensitivity among samples, Au nanoring arrays with similar LSPR absorption peaks were used ($8{,}180 \pm 50$ cm^{-1} in air). A solution containing 2.5 nM AuNPs modified with complementary DNA of sequence A (denoted Ac) was flowed over the sensor surface for 90 min and the shift in resonance wavenumber was monitored (see Figure 3.7a). When the surface coverage of sequence A was 100 %, the resonance wavenumber of Au nanorings immediately shifted to lower wavenumber after the injection of AuNPs solution. Upon hybridization, the resonance wavenumber shifted by as much as 170 cm^{-1}. In contrast, for the surface modified entirely with noncomplementary DNA (100 % covered with sequence B), the shift in resonance wavenumber

was negligible, indicating the high selectivity of DNA hybridization onto Au nanoring arrays and the lack nonspecific adsorption. Figure 3.7a also shows the adsorption curves observed for 5 and 0.5 % complementary ssDNA monolayer. A full set of steady state LSPR peak shifts as a function of percentage of sequence A (%A) is shown in Figure 3.7b. The lowest %A surface coverage θ that could be measured was 0.5 %. This surface coverage θ corresponds to that can be created by a DNA concentration C min of 50 pM, assuming a Langmuir adsorption coefficient K_{ads} of 1.0×10^8 M^{-1} ($C_{min} = \theta / K_{ads}$).[30]

3.4 Conclusions

In this study, Au nanoring array surfaces exhibiting strong localized surface plasmon resonances at near infrared wavelengths were employed for refractive index biosensing by using FT-NIR transmittance spectroscopy. The Au nanoring arrays were fabricated by a simple bottom up process based on lithographically patterned nanoscale electrodeposition of Au nanorings, which enabled fabrication of Au nanoring arrays over large surface area with excellent control of the nanoring spacing, diameter, and width. The plasmonic absorption bands of Au nanoring arrays could be tuned from 1.1 to 1.6 μm in the NIR region by controlling the size and width of the nanorings. Real-time FT-NIR measurements were performed to detect changes in the bulk refractive index of solutions. The results revealed that the Au nanoring arrays exhibit a high bulk refractive index sensitivity up to 3,780 cm^{-1}/RIU, which is comparable to that of the state of the art of LSPR sensors with more complicated structures. Two examples of LSPR sensing with these Au nanoring arrays were performed: (1) the polymerization of dopamine to create polydopamine multilayers onto the nanoring sensor surface was monitored in real time, and (2) the hybridization adsorption of DNA-functionalized AuNPs onto Au nanoring arrays modified

with complementary DNA was characterized. Using two component mixed DNA monolayers, relative surface coverages of complementary DNA as low as 0.5% were detected, which corresponded to the detection of DNA by hybridization adsorption from a 50 pM solution. Our future work will include the fabrication of asymmetric nanoring structures such as split rings[32] and nanomushrooms[33] for further advanced sensitivities by using Fano type plasmon resonances.

3.5 Acknowledgments

The authors thank the laboratory for electron and X-ray instrumentation (LEXI) for the use of the SEM and the plasma cleaner as well as Dr. JY Kim and Prof. R. M. Penner for the use of the furnace. This work was funded by NSF CHE-1057638.

3.6 References

(1) Brolo, A. G., Plasmonics for Future Biosensors. *Nat Photon* **2012,** 6, (11), 709-713.

(2) Homola, J., Surface Plasmon Resonance Sensors for Detection of Chemical and Biological Species. *Chem. Rev.* **2008,** 108, (2), 462-493.

(3) Mayer, K. M.; Hafner, J. H., Localized Surface Plasmon Resonance Sensors. *Chem. Rev.* **2011,** 111, (6), 3828-3857.

(4) Anker, J. N.; Hall, W. P.; Lyandres, O.; Shah, N. C.; Zhao, J.; Van Duyne, R. P., Biosensing with Plasmonic Nanosensors. *Nat Mater* **2008,** 7, (6), 442-453.

(5) Stewart, M. E.; Anderton, C. R.; Thompson, L. B.; Maria, J.; Gray, S. K.; Rogers, J. A.; Nuzzo, R. G., Nanostructured Plasmonic Sensors. *Chem. Rev.* **2008,** 108, (2), 494-521.

(6) Willets, K. A.; Van Duyne, R. P., Localized Surface Plasmon Resonance Spectroscopy and Sensing. In *Annual Review of Physical Chemistry*, 2007; Vol. 58, pp 267-297.

(7) Haes, A. J.; Van Duyne, R. P., A Nanoscale Optical Biosensor: Sensitivity and Selectivity of an Approach Based on the Localized Surface Plasmon Resonance Spectroscopy of Triangular Silver Nanoparticles. *J. Am. Chem. Soc.* **2002,** 124, (35), 10596-10604.

(8) Sherry, L. J.; Chang, S. H.; Schatz, G. C.; Van Duyne, R. P.; Wiley, B. J.; Xia, Y. N., Localized Surface Plasmon Resonance Spectroscopy of Single Silver Nanocubes. *Nano Lett.* **2005,** 5, (10), 2034-2038.

(9) Mahmoud, M. A.; Chamanzar, M.; Adibi, A.; El-Sayed, M. A., Effect of the Dielectric Constant of the Surrounding Medium and the Substrate on the Surface Plasmon Resonance Spectrum and Sensitivity Factors of Highly Symmetric Systems: Silver Nanocubes. *J. Am. Chem. Soc.* **2012,** 134, (14), 6434-6442.

(10) Kathryn, M. M.; Feng, H.; Seunghyun, L.; Peter, N.; Jason, H. H., A Single Molecule Immunoassay by Localized Surface Plasmon Resonance. *Nanotech.* **2010,** 21, (25), 255503.

(11) Lee, S.-W.; Lee, K.-S.; Ahn, J.; Lee, J.-J.; Kim, M.-G.; Shin, Y.-B., Highly Sensitive Biosensing Using Arrays of Plasmonic Au Nanodisks Realized by Nanoimprint Lithography. *ACS Nano* **2011,** 5, (2), 897-904.

(12) Hao, J.; Tingjie, L.; Ertorer, E.; Jun, Y.; Sabarinathan, J.; Mittler, S., A Biosensor Based on Periodic Arrays of Gold Nanodisks under Normal Transmission. *Sensors and Actuators A (Phys.)* **2013,** 189, 474-80.

(13) Marinakos, S. M.; Chen, S. H.; Chilkoti, A., Plasmonic Detection of a Model Analyte in Serum by a Gold Nanorod Sensor. *Anal. Chem.* **2007,** 79, (14), 5278-5283.

(14) Piliarik, M.; Sipova, H.; Kvasnicka, P.; Galler, N.; Krenn, J. R.; Homola, J., High-Resolution Biosensor Based on Localized Surface Plasmons. *Opt. Express* **2012,** 20, (1), 672-680.

(15) Mayer, K. M.; Lee, S.; Liao, H.; Rostro, B. C.; Fuentes, A.; Scully, P. T.; Nehl, C. L.; Hafner, J. H., A Label-Free Immunoassay Based upon Localized Surface Plasmon Resonance of Gold Nanorods. *ACS Nano* **2008,** 2, (4), 687-692.

(16) Larsson, E. M.; Alegret, J.; Käll, M.; Sutherland, D. S., Sensing Characteristics of NIR Localized Surface Plasmon Resonances in Gold Nanorings for Application as Ultrasensitive Biosensors. *Nano Lett.* **2007,** 7, (5), 1256-1263.

(17) Chengjun, H.; Jian, Y.; Shuo, W.; Stakenborg, T.; Lagae, L., Gold Nanoring as a Sensitive Plasmonic Biosensor for On-Chip DNA Detection. *Appl. Phys. Lett.* **2012,** 100, (17), 173114 (4 pp.)-173114 (4 pp.).

(18) Tsai, C.-Y.; Lu, S.-P.; Lin, J.-W.; Lee, P.-T., High Sensitivity Plasmonic Index Sensor Using Slablike Gold Nanoring Arrays. *App. Phys. Lett.* **2011,** 98, (15).

(19) Kim, S.; Jung, J.-M.; Choi, D.-G.; Jung, H.-T.; Yang, S.-M., Patterned Arrays of Au Rings for Localized Surface Plasmon Resonance. *Langmuir* **2006,** 22, (17), 7109-7112.

(20) Ye, J.; Van Dorpe, P.; Lagae, L.; Maes, G.; Borghs, G., Observation of Plasmonic Dipolar Anti-Bonding Mode in Silver Nanoring Structures. *Nanotech.* **2009,** 20, (46).

(21) Aizpurua, J.; Hanarp, P.; Sutherland, D. S.; Kall, M.; Bryant, G. W.; de Abajo, F. J. G., Optical Properties of Gold Nanorings. *Phys. Rev. Lett.* **2003,** 90, (5).

(22) Halpern, A. R.; Corn, R. M., Lithographically Patterned Electrodeposition of Gold, Silver, and Nickel Nanoring Arrays with Widely Tunable Near-Infrared Plasmonic Resonances. *ACS Nano* **2013,** 7, (2), 1755-1762.

(23) Sendroiu, I. E.; Gifford, L. K.; Lupt $\bar{\tau}_{\circ}$k, A.; Corn, R. M., Ultrasensitive DNA Microarray Biosensing via in Situ RNA Transcription-Based Amplification and Nanoparticle-Enhanced SPR Imaging. *J. Am. Chem. Soc.* **2011,** 133, (12), 4271-4273.

(24) Wood, J. B.; Szyndler, M. W.; Halpern, A. R.; Cho, K.; Corn, R. M., Fabrication of DNA Microarrays on Polydopamine-Modified Gold Thin Films for SPR Imaging Measurements. *Langmuir* **2013,** 29, (34), 10868-10873.

(25) Turkevich, J.; Stevenson, P. C.; Hillier, J., A Study of the Nucleation and Growth Processes in the Synthesis of Colloidal Gold. *Disc. Faraday Soc.* **1951,** 11, (0), 55-75.

(26) Chen, Y.; Nguyen, A.; Niu, L.; Corn, R. M., Fabrication of DNA Microarrays with Poly(L-glutamic acid) Monolayers on Gold Substrates for SPR Imaging Measurements. *Langmuir* **2009,** 25, (9), 5054-5060.

(27) Kedenburg, S.; Vieweg, M.; Gissibl, T.; Giessen, H., Linear Refractive Index and Absorption Measurements of Nonlinear Optical Liquids in the Visible and Near-Infrared Spectral Region. *Opt. Mat. Exp.* **2012,** 2, (11), 1588-1611.

(28) Kubo, W.; Fujikawa, S., Au Double Nanopillars with Nanogap for Plasmonic Sensor. *Nano Lett.* **2011,** 11, (1), 8-15.

(29) Verellen, N.; Van Dorpe, P.; Huang, C.; Lodewijks, K.; Vandenbosch, G. A. E.; Lagae, L.; Moshchalkov, V. V., Plasmon Line Shaping Using Nanocrosses for High Sensitivity Localized Surface Plasmon Resonance Sensing. *Nano Lett.* **2011,** 11, (2), 391-397.

(30) Lee, H.; Dellatore, S. M.; Miller, W. M.; Messersmith, P. B., Mussel-Inspired Surface Chemistry for Multifunctional Coatings. *Science* **2007,** 318, (5849), 426-430.

(31) Lynge, M. E.; van der Westen, R.; Postma, A.; Stadler, B., Polydopamine-a Nature-Inspired Polymer Coating for Biomedical Science. *Nanoscale* **2011,** 3, (12), 4916-4928.

(32) Chen, C.-Y.; Un, I.-W.; Tai, N.-H.; Yen, T.-J., Asymmetric Coupling Between Subradiant and Superradiant Plasmonic Resonances and Its Enhanced Sensing Performance. *Opt. Exp.* **2009,** 17, (17), 15372-15380.

(33) Shen, Y.; Zhou, J.; Liu, T.; Tao, Y.; Jiang, R.; Liu, M.; Xiao, G.; Zhu, J.; Zhou, Z.-K.; Wang, X.; Jin, C.; Wang, J., Plasmonic Gold Mushroom Arrays with Refractive Index Sensing Figures of Merit Approaching the Theoretical Limit. *Nat Comm.* **2013,** 4.

Chapter 4

Measuring Melittin Uptake into Hydrogel Nanoparticles with Near-Infrared Single Nanoparticle Surface Plasmon Resonance Microscopy

4.1 Introduction

Among the numerous nanoscale drug delivery systems that are currently being developed, hydrogel nanoparticles (HNPs) have become an increasingly popular vehicle for the controlled uptake, localization, and release of bioactive compounds.[1-6] These polymeric nanoparticles can be engineered to respond to external stimuli by switching their physical properties, making them ideal candidates for the targeted delivery of therapeutics. For example,

small changes in solvent pH, ionic strength, temperature, or light can drastically change an HNP's physical or chemical properties, and these changes can be used for the uptake and release of drugs, genes, peptides, or proteins.[7-11]

In addition to engineering HNPs to be sensitive to environmental changes, the polymer makeup of the nanoparticles can be tailored to uptake specific target compounds. Previously, temperature responsive HNPs were shown to reversibly switch affinity to a host of target compounds including short peptides, proteins, and drug molecules such as doxorubicin.[12-16] The affinity of HNPs to specific compounds can be controlled by reacting *N*-isopropylacrylamide (NIPAm) with polymers containing complimentary functional groups. Figure 4.1a depicts NIPAm-based HNPs that incorporate hydrophobic groups (*N*-*tert*-butylacrylamide, TBAm), negatively charged groups (acrylic acid, AAc), and cross linkers (*N,N'*-methylenebisacrylamide, BIS). These HNPs were designed to have a high uptake affinity for melittin, the principal component of bee venom and a molecule that has shown promise in the treatment of HIV infections and epilepsy.[17,18] Melittin is a short peptide composed of 26 amino acids (GIGAVLKVLT-TGLPALISWIKRKRQQ) with mostly nonpolar or positively charged residues (illustrated in Figure 2b), and thus is expected to specifically absorb into the HNPs via hydrophobic and electrostatic interactions.

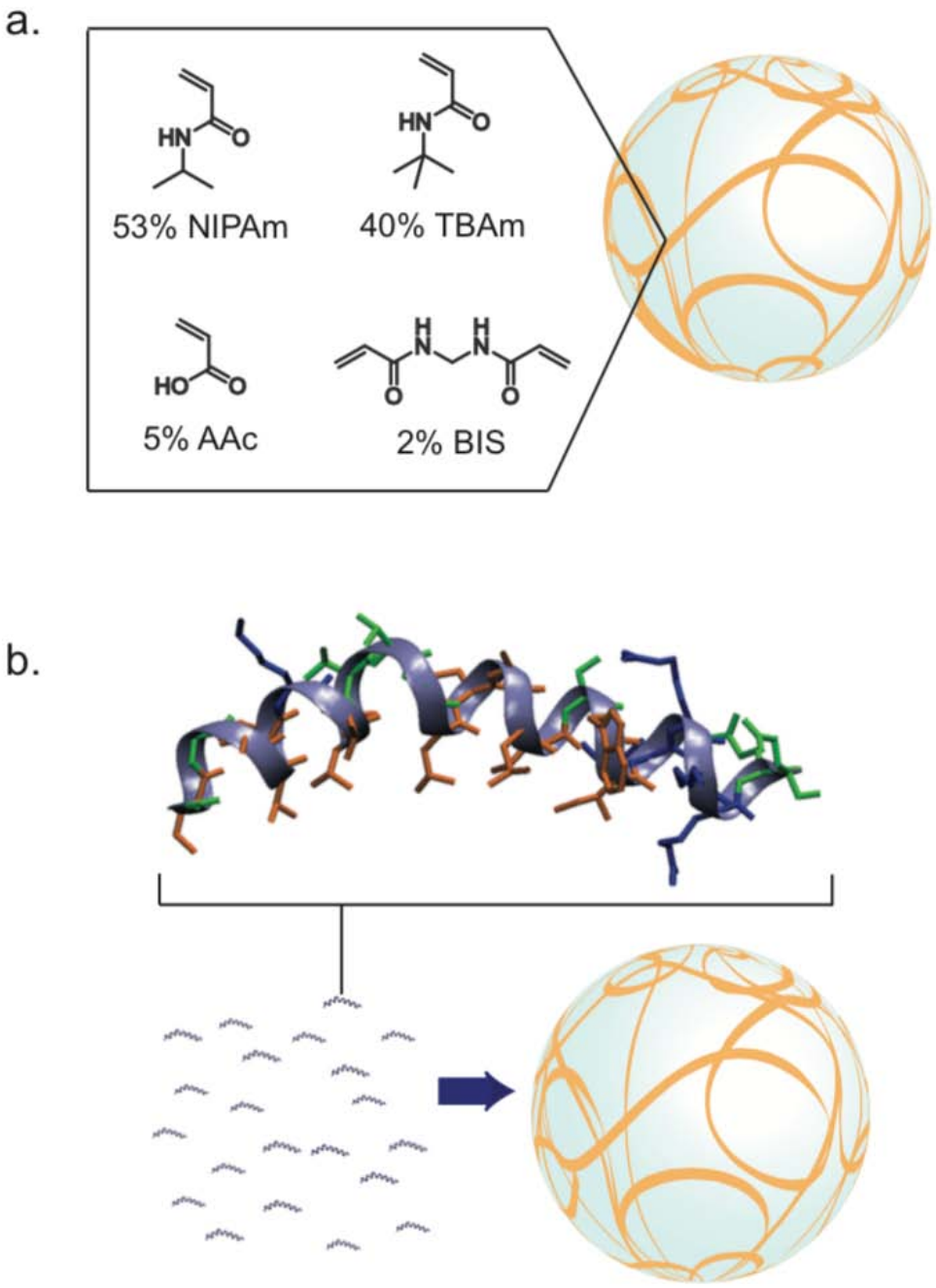

Figure 4.1: (a) Hydrogel nanoparticles (HNPs) were composed of *N*-isopropylacrylamide (NIPAm), *N*-*tert*-butylacrylamide (TBAm), acrylic acid (AAc), and *N,N'*-methylenebisacrylamide (BIS) in a molar ratio of NIPAm:TBAm:AAc:BIS :: 53:40:5:2. (b) Illustration of melittin with nonpolar side chains in orange, polar side chains in green, and positively charged side chains in blue. Melittin is bound by HNPs via hydrophobic and electrostatic interactions (melittin structure obtained from the Research Collaboratory for Structural Bioinformatics).

The characterization of HNPs can be challenging given their pliable and solvent swollen internal structure. Cryo-transmission electron microscopy (cryo-TEM) can be used to examine hydrogel size and morphology,[19,20] but the *in situ* measurement of the uptake of small organic molecules or peptides into individual nanoparticles poses greater challenges. Dynamic light scattering (DLS) can be used to determine mean hydrodynamic diameters of HNPs,[21] but the effect of the uptake of molecules into nanoparticles on the DLS is difficult to quantify. Multi-angle light scattering (MALS) measurements have been used to estimate molecular weight changes upon protein loading by hydrogels,[22] but both DLS and MALS provide only average results for any change upon HNP loading. In addition, HNP affinity to proteins have been estimated by size exclusion chromatography,[23] but the interpretation of elution data is nontrivial.

Single nanoparticle surface plasmon resonance microscopy (SPRM) is a relatively new technique that uses surface plasmon polariton (SPP) point diffraction patterns to monitor in real-time the adsorption of single nanoparticles onto a gold surface.[24-26] In addition to single nanoparticles, SPRM has been employed to study a variety of nanostructures, membrane proteins, intracellular processes, cell-substrate interactions, and viruses.[27-34] In a recent paper, we showed that near-infrared (NIR, 814 nm) SPRM is highly sensitive and can be used to track the adsorption of individual gold and polystyrene nanoparticles onto chemically modified gold thin film surfaces in real-time.[35] Upon adsorption of a nanoparticle, a large SPP point diffraction pattern on the order of 10^2 μm^2 is generated; the magnitude of the response depends on the size and composition of the nanoparticle, and has been observed for both gold nanoparticles as small as 20 nm and polystyrene nanoparticles as small as 85 nm.

In this chapter, the uptake of the bioactive peptide melittin into NIPAm-based HNPs is directly measured with NIR SPRM. As noted above, the NIPAm-based HNPs contain a mixture

of hydrophobic and negatively charged side chains that provide a specific affinity for the peptide melittin. The adsorption of single 220 nm HNPs from picomolar nanoparticle solutions onto a hydrophobic alkanethiol-modified gold surface is detected in real-time from the appearance of point diffraction patterns in sequential SPR differential reflectivity images; these point diffraction patterns are counted to create a digital adsorption binding curve. The intensities of the point diffraction patterns observed in the sequential SPR differential reflectivity images used to create this digital adsorption binding curve are quantitated, and the average of these intensity values, denoted as $<\Delta\%R_{NP}>$, is obtained. When melittin is mixed at micromolar concentrations with the HNPs, the value of $<\Delta\%R_{NP}>$ is found to increase linearly with melittin concentration. This increase is attributed to an increase in the refractive index of the HNPs due to the incorporation of melittin into the hydrogel nanoparticle. DLS measurements confirm that no change in mean HNP hydrodynamic diameter is observed in the presence of melittin over this entire concentration range, indicating that the increase of the SPRM response is not from a volume increase. The specific uptake affinity of melittin for these HNPs is confirmed as no increase in $<\Delta\%R_{NP}>$ is observed in the presence of micromolar solutions of either FLAG octapeptide or bovine serum albumin (BSA). Additional bulk fluorescence measurements that measure the loss of melittin in solution when mixed with HNPs are used to estimate that a 1% increase in $<\Delta\%R_{NP}>$ corresponds to the uptake of approximately 65,000 molecules into the 220 nm HNP, corresponding to roughly 4% of its volume.

4.2 Experimental Considerations

4.2.1 Hydrogel Nanoparticle Materials

All chemicals were obtained from commercial sources: *N*-isopropylacrylamide (NIPAm), ammonium persulfate (APS), and melittin (from honey-bee venom), were from Sigma-Aldrich, Inc. (St. Louis, MO); Acrylic acid (AAc) and sodium dodecyl sulfate (SDS) were from Aldrich Chemical Co.; *N,N′*-methylenebisacrylamide (BIS) was from Fluka; *N*-*tert*-butylacrylamide (TBAm) was from Acros Organics (Geel, Belgium). **Hydrogel Nanoparticle Synthesis.** The procedure reported by Debord and Lyon was adapted to synthesize HNPs.[36] AAc (5 mol %), TBAm (40 mol %), NIPAm (53 mol %), BIS (2 mol %) and SDS (2.5 mg) were dissolved in water (50 mL) and the resulting solutions were filtered through a no. 2 Whatman filter paper. TBAm was dissolved in ethanol (1 mL) before addition to the monomer solution. The total monomer concentration was 65 mM. Nitrogen gas was bubbled through the reaction mixtures for 30 min. Following the addition of 500 μL of aqueous solution containing 30 mg of APS, the pre-polymerization mixture was sealed under nitrogen gas. Polymerization was carried out by inserting the round bottle flask containing pre-polymerization mixture in an oil bath pre-set to 60 °C for 3 h. The polymerized solutions were purified by dialysis using a 12-14 kDa molecular weight cut off (MWCO) membrane against an excess amount of pure water (changed more than twice a day) for 4 days. The yield and concentration of HNPs were determined by gravimetric analysis of lyophilized polymers.

4.2.2 Dynamic Light Scattering Measurements

The hydrodynamic diameter of HNPs was determined in aqueous solutions (25 ± 0.1 °C) by a dynamic light scattering (DLS) instrument equipped with Zetasizer Software Ver. 6.12 (Zetasizer Nano ZS, Malvern Instruments Ltd, Worcestershire, U.K.). All the results of DLS data fitting met the quality criteria set by Malvern (see Supporting Information in the Appendix for DLS results).

4.2.3 d*n*/d*c* and MALS Measurements

The average molar mass of the HNPs was determined by a combination of d*n*/d*c* and multi angle light scattering (MALS) measurements using Optilab rEX (Wyatt Technology Corporation, Santa Barbara, CA) and DAWN HELEOS (Wyatt Technology Corporation), respectively (see Supporting Information in the Appendix for details).

4.2.4 Surface Plasmon Resonance Microscope Optical Setup

The SPR microscope setup was discussed in a recent publication and diagrammed in Chapter 1 of this dissertation.[35] Briefly, the microscope was built into the frame of an IX51 inverted microscope (Olympus, Tokyo, Japan). A 1 mW 814 nm diode laser (Melles Griot, Carlsbad, CA) was expanded and collimated using a spatial filter (Newport Corp., Newport Beach, CA). The beam was then polarized and focused with a lens (f = 200 mm) onto the back focal plane of a 100x 1.49 NA oil objective (Olympus). The focused beam was directed up to the objective using a gold-coated knife-edge mirror (Thorlabs, Newton, NJ). The reflected image was passed to an Andor Neo sCMOS (South Windsor, CT). Images were acquired by accumulating 30 11-bit exposures.

4.2.5 Substrate Preparation

Substrates were borosilicate No. 1.5 coverslips (Fisherbrand, Pittsburgh, PA) coated with 1 nm Cr adhesion layer and 45 nm Au by thermal evaporation. The Au surface was functionalized by undecanethiol (C11) by overnight immersion of the substrate in a 1 mM ethanolic solution of 1-undecanethiol (Sigma-Aldrich). The imaging surface was partitioned using adhesive silicone isolation wells (Electron Microscopy Sciences, Hatfield, PA).

4.2.6 SPRM Analysis

HNP solutions were prepared by a 50-fold dilution in 1x PBS (11.9 mM phosphates, 137 mM sodium chloride, 2.7 mM potassium chloride, pH 7.4, Fisher). For SPRM measurements, the HNPs were further diluted by 3/10 with 1x PBS and the appropriate amount of 9 μM melittin (Sigma-Aldrich), FLAG peptide (DYKDDDDK, Sigma-Aldrich), or bovine serum albumin (Sigma-Aldrich) in PBS, which yielded a solution with a final HNP concentration of 30 pM. Images were acquired after 5 minutes of mixing the HNP and melittin. 10 μL of HNP solution was pipetted into the isolation well for imaging. In this work, the Δ%R from the adsorption of a nanoparticle was calculated by multiplying the quotient of the difference image and raw image by 30% (the incidence angle was set to 30% reflectivity).

4.2.7 Bulk Melittin Fluorescence Measurements

The intrinsic fluorescence of melittin from its sole tryptophan residue[37] was measured for bulk uptake measurements. Duplicate 5 mL samples were prepared with and without HNPs in the same concentrations as for SPRM analysis. All samples were ultracentrifuged (50,000 rpm,

1h) using a Beckman Coulter Optima LE-80K Ultracentrifuge (Beckman Coulter, Inc., Brea, CA) with a NVT90 rotor (Beckman Coulter). The supernatant was then removed for fluorescence measurements using a JASCO FP-6300 Spectrofluorometer (JASCO Analytical Instruments, Easton, MD). Fluorescence was measured for samples with and without melittin to determine a percent loss of melittin upon mixing with HNPs. For 0.5 μM melittin samples, the supernatant was removed upon ultracentrifugation and lyophilized using FreeZone 4.5 (Labconco, Kansas City, MO); these samples were then dissolved in 1/10 of the original volume to obtain 10x concentrated samples. Fluorescence measurements are detailed in the Supporting Information in the Appendix.

4.3 Results and Discussion

4.3.1 Synthesis of 220 nm NIPAm-Based HNPs for Melittin Uptake

As depicted in Figure 4.1a, HNPs were synthesized by the copolymerization of four monomers: *N*-isopropylacrylamide (NIPAm), *N*-*tert*-butylacrylamide (TBAm), acrylic acid (AAc), and *N,N'*-methylenebisacrylamide with molar percentages of 53%, 40%, 5%, and 2%, respectively. The mean hydrodynamic diameter of these HNPs in phosphate buffered saline (PBS) solution was determined by DLS measurements to be 220 nm. Additional d*n*/d*c* and multi-angle light scattering measurements were used to obtain an estimate of 1.24 x 10^9 g/mol for the average molecular weight of the HNPs (see Supporting Information in the Appendix for the details of these measurements). Using this average molecular weight and an approximate dry polymer density of 1.1 g/mL (which is equivalent to the density of NIPAm),[38] we estimate that the HNPs contain approximately ~65% solvent (in this case, PBS) by volume. The high

percentage TBAm incorporated into the HNPs makes them very nonpolar, and the inclusion of AAc residues gives the HNPs a net negative charge in PBS. These HNPs are expected to have a specific uptake affinity for melittin, which has 16 nonpolar, five polar, and five charged amino acid residues with a net charge of +6 in PBS,[39,40] via a combination of hydrophobic and electrostatic interactions.[12,13]

4.3.2 Irreversible Adsorption of Single 220 nm HNPs onto a Hydrophobic Surface

Because of their significant nonpolar nature, the HNPs were found to irreversibly adsorb from PBS solutions onto gold surfaces that had been previously modified with hydrophobic undecanethiol (C11) monolayers. Real-time single nanoparticle SPRM measurements were employed to monitor the adsorption of 220 nm HNPs onto C11-functionalized gold surfaces. Specifically, 10 μL of a 15, 30, or 60 pM HNP solution was pipetted onto a C11-functionalized gold thin film and SPRM reflectivity images were recorded every three seconds for a total of 10 minutes. For each SPRM reflectivity image, the SPRM reflectivity image from the immediately previous time frame was subtracted in order to create a time course series of SPRM **differential** reflectivity images. An example of one of these SPRM differential reflectivity images for adsorption from a 30 pM HNP solution is shown in Figure 4.2a.

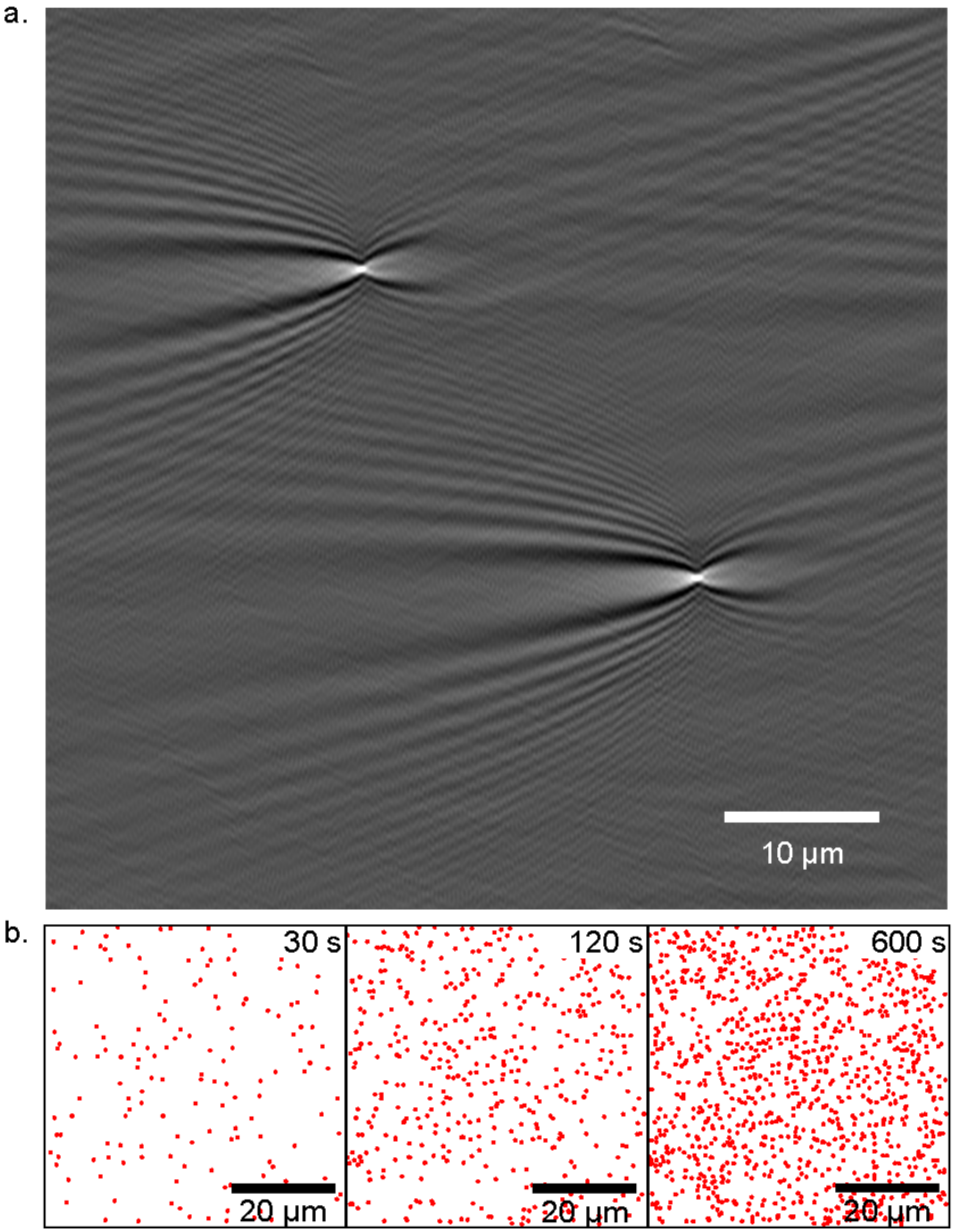

Figure 4.2: (a) A 58.5 µm x 58.5 µm Fourier filtered SPRM three second differential reflectivity image showing the adsorption of two individual 220 nm diameter HNPs onto a C11-functionalized gold thin film from a 30 pM HNP PBS solution. (b) Three 2-D cumulative adsorption maps tracking the locations of adsorbed HNPs after 30, 120, and 600 seconds in the same imaging area. Each red point corresponds to the adsorption of a single HNP. The total cumulative number of adsorbed HNPs after 30, 120, and 600 seconds is 152, 448, and 1051 nanoparticles, respectively.

As reported previously by a number of research groups,[24-26,35] the adsorption of single metal, semiconductor, and polymer nanoparticles onto a gold thin film can appear in the SPRM differential reflectivity image as point diffraction patterns of the surface plasmon polaritons (SPPs) travelling across the surface. In Figure 4.2a, two point diffraction patterns are clearly visible due to the adsorption of single HNPs. These diffraction patterns are very similar to those we have seen previously with gold nanoparticles and polystyrene nanoparticles, and are due to constructive and destructive interferences created in the 814 nm travelling SPP waves by the change in local refractive index due to the adsorption of a 220 nm nanoparticle. The total size of the image in Figure 4.2a is 58.5 μm x 58.5 μm, and remarkably, the signal created from one low density 220 nm nanoparticle can span more than a 10 μm x 10 μm area in this image. The two distinct diffraction patterns in Figure 2a signify that two HNPs have adsorbed onto the imaging area in this three second time frame. SPRM differential reflectivity images have also been used to monitor the desorption of nanoparticles from the surface, which appear as negative images in these diffraction patterns.[35] However, no desorption events were observed in the differential reflectivity images for HNP adsorption onto C11-functionalized surfaces, indicating that the hydrophobicity of the HNPs was sufficient to irreversibly adsorb the nanoparticles over the time frame of 10 minutes.

The number and locations of adsorbed nanoparticles were recorded for each SPRM differential reflectivity image in the time course series. Figure 4.2b displays three 2-D cumulative adsorption maps which plot with red points the locations of all of the 220 nm HNPs that have been adsorbed in the imaging area from a 30 pM HNP solution after 30, 120, and 600 seconds. These 2-D maps show that the adsorption of the HNPs onto C11-functionalized surfaces is fairly uniform and that there is no surface aggregation of the HNPs. The total cumulative

number of nanoparticles adsorbed to the surface after 30, 120, and 600 seconds was 152, 448, and 1051 nanoparticles, respectively.

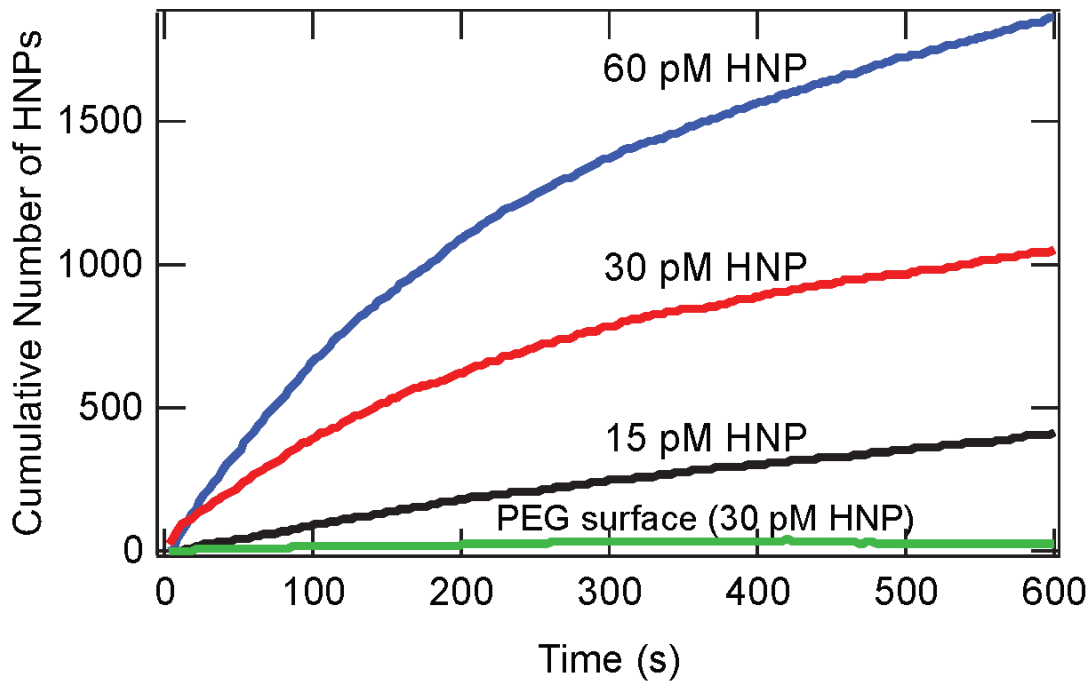

Figure 4.3: Real-time digital adsorption curves of the cumulative number of HNPs adsorbed onto a C11-functionalized gold surface over 10 minutes from 15, 30 and 60 pM HNP solutions (black, red and blue curves, respectively). The initial adsorption rates (the slopes of these curves at zero time) varied linearly with HNP concentration. Also shown in the Figure is a negative control, the adsorption of HNPs from a 30 pM solution onto a PEG-functionalized gold surface (green curve) that resulted in a cumulative adsorption of less than 20 HNPs in 10 minutes.

By tallying this total cumulative number of adsorbed nanoparticles on a frame-by-frame basis, we are able to create "digital adsorption curves" for the adsorption of HNPs onto C11-functionalized surfaces. Figure 4.3 plots the cumulative number of adsorbed 220 nm HNPs of 15, 30, and 60 pM concentrations over the course of 10 minutes. As seen in the Figure, the initial adsorption rate (the slope at zero time of the adsorption curves) roughly doubles as the solution concentration doubles, as expected.[35] Also shown in the Figure is the digital adsorption curve

obtained after exposure of a polyethylene glycol (PEG)-functionalized gold thin film to a 30 pM HNP solution. Almost no HNP adsorption (less than 20 HNPs in 10 minutes) was observed onto this surface, verifying that it is a hydrophobic interaction that drives the HNPs to the C11-functionalized surface.

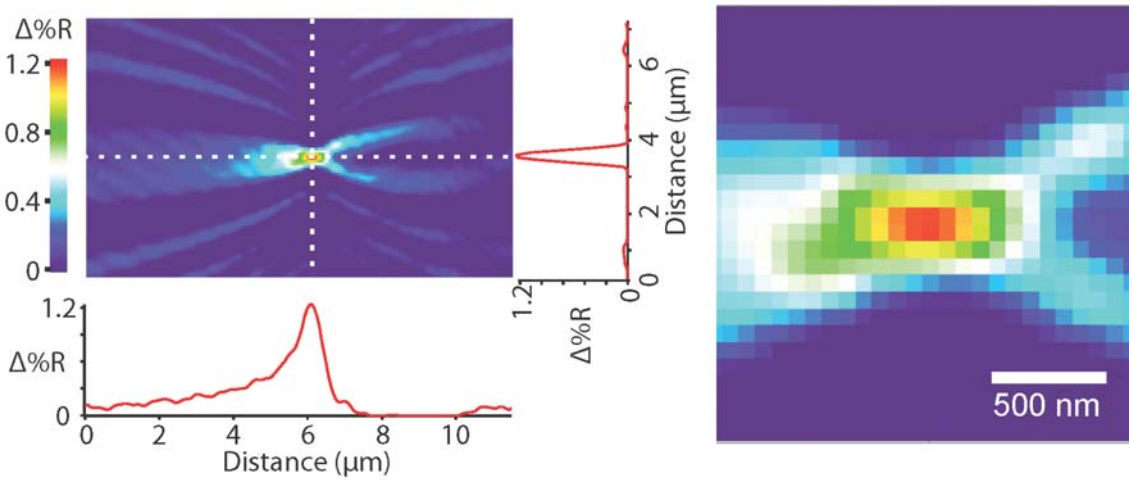

Figure 4.4: Determination of the single nanoparticle SPRM reflectivity change, $\Delta\%R_{NP}$, from an HNP point diffraction pattern in the SPRM three second differential reflectivity image. A sharp central feature is observed in the image at the intersection of the two white dashed lines; a blow up of that intersection is shown on the right. We define $\Delta\%R_{NP}$ as the average of the Δ%R values for the nine pixels in the image at and around the pixel with the maximum Δ%R intensity.

4.3.3 Quantitation of the Average Single Nanoparticle SPRM Reflectivity Change ($<\Delta\%R_{NP}>$) for HNPs

In addition to counting the number of adsorbed HNPs with our digital binding curves, we are also able to quantitate the average intensity of the point diffraction patterns in the SPRM differential reflectivity images due to the adsorption of single HNPs onto the C11-functionalized surface. A false colored enlargement of one of these point diffraction images is shown in Figure 4.4. The signal is composed of an SPP diffraction pattern of alternating bright and dark tails and

an intense central spike in the differential reflectivity (Δ%R) at the intersection of the two white dotted lines. On the right hand side of Figure 4.4 is a blow up of this feature; we define the "single nanoparticle SPRM reflectivity change" ($\Delta\%R_{NP}$) as the average of the Δ%R values for the nine pixels (a 3 x 3 array) in the image at and around the pixel with the maximum Δ%R intensity.

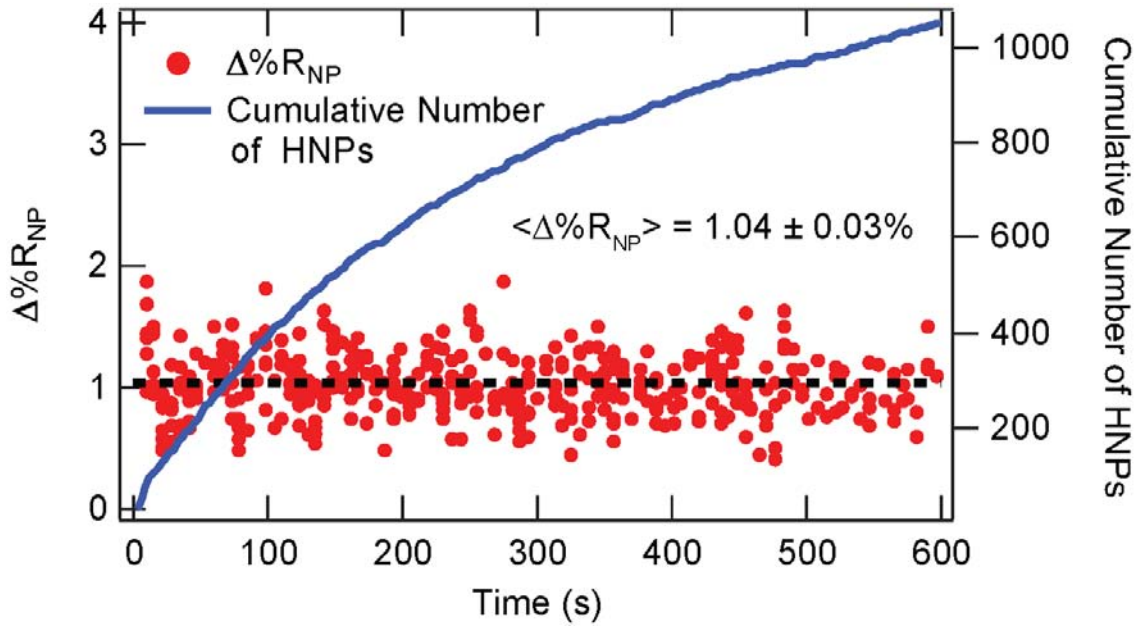

Figure 4.5: The determination of $\langle\Delta\%R_{NP}\rangle$ for the adsorption of 220 nm HNPs onto a C11-functionalized surface from a 30 pM HNP solution. Each red point in the plot is a $\Delta\%R_{NP}$ for a single adsorbed HNP obtained from one of the sequential SPRM differential reflectivity images. For this experiment, a total of 422 $\Delta\%R_{NP}$ values were obtained over ten minutes. The black dashed line is the value of $\langle\Delta\%R_{NP}\rangle$ obtained from this data, 1.04 ± 0.03% where ± 0.03% is the 95% confidence interval. Also plotted in the Figure is the digital adsorption curve of the cumulative number of adsorbed HNPs (solid blue line).

To determine the **average** value of $\Delta\%R_{NP}$ during an HNP adsorption experiment, which we denote as $\langle\Delta\%R_{NP}\rangle$, we measured the individual $\Delta\%R_{NP}$ values for a large number of the adsorbed HNPs observed in the time course series of SPRM three second differential reflectivity

images. An example of this data for the adsorption of HNPs onto a C11-functionalized surface from a 30 pM HNP solution is plotted in Figure 5 along with the digital adsorption curve of the cumulative number of adsorbed HNPs. For these experiments, we chose to work with 30 pM HNP solutions because the HNP adsorption rate at this concentration produced many images with a small number of non-overlapping diffraction patterns. Each red dot in Figure 4.5 represents a $\Delta\%R_{NP}$ value obtained from a single HNP point diffraction pattern; we often obtained multiple $\Delta\%R_{NP}$ values from each differential reflectivity image. After ten minutes, we measured $\Delta\%R_{NP}$ for 422 nanoparticles to obtain a $<\Delta\%R_{NP}>$ of 1.04 ± 0.03% where 0.03% is the value of the 95% confidence interval ($\pm 2\sigma/(422)^{1/2}$) with a standard deviation σ = 0.3%. As discussed in a previous paper,[35] the distribution in $\Delta\%R_{NP}$ values is the result of the combination of the distribution of nanoparticle sizes and any instrumental noise artifacts introduced by the SPR microscope. This measurement of $<\Delta\%R_{NP}>$ was repeated three times, all of which yielded $<\Delta\%R_{NP}>$ values within the confidence interval (1.04 ± 0.03%). This Δ%R is well within the range of Δ%R values that are regularly measured in standard SPR imaging measurements.[41-43]

4.3.4 Measurement of Melittin Uptake into HNPs via the Increase $<\Delta\%R_{NP}>$

The NIPAm-based HNPs used in the single nanoparticle SPRM measurements have been specifically designed for the selective uptake of the bioactive 26-residue peptide melittin, and the affinity of melittin to these HNPs has been documented previously.[44] We show here that quantitative measurements of $<\Delta\%R_{NP}>$ from single nanoparticle SPRM measurements of HNPs can be used to (i) demonstrate the specificity of melittin binding to these HNPs and (ii) quantify the amount of peptide uptake into HNPs.

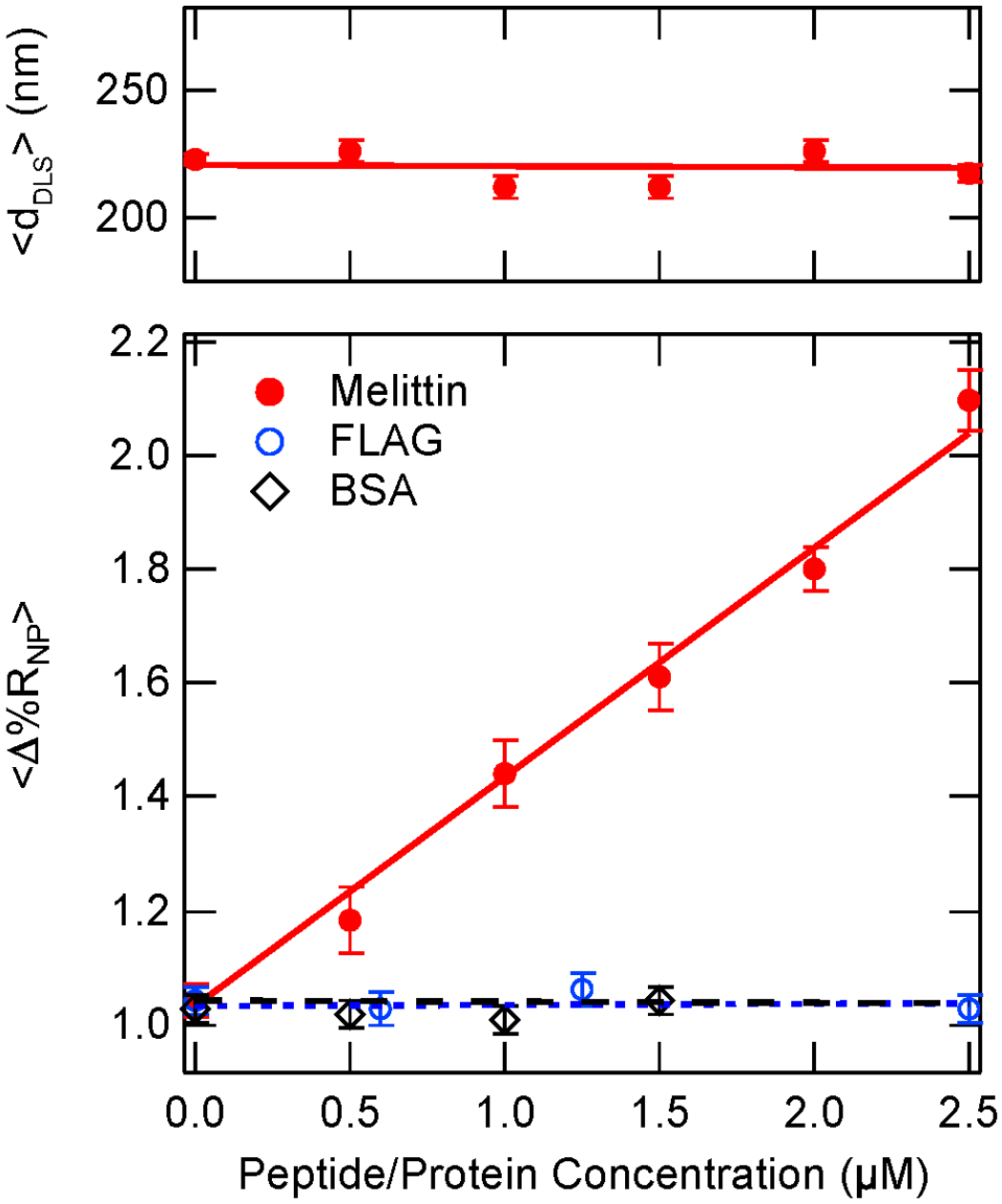

Figure 4.6: Lower Panel: Average single nanoparticle SPRM reflectivity values, $<\Delta\%R_{NP}>$, obtained from single nanoparticle SPRM measurements of the adsorption of 220 nm HNPs onto C11-functionalized gold surfaces in the presence of melittin (red solid circles), FLAG peptide (blue open circles) and BSA (black open diamonds). For all measurements, the HNP concentration was fixed at 30 pM. Error bars are the 95% confidence intervals for the $<\Delta\%R_{NP}>$ values. Upper Panel: Mean hydrodynamic diameter ($<d_{DLS}>$) obtained from DLS measurements in the presence of melittin. The observation of no change in $<d_{DLS}>$ in the presence of melittin confirms that the increase in $<\Delta\%R_{NP}>$ in the presence of melittin is the result of an increase in the refractive index of the NIPAm-based HNPs due to the specific uptake of peptide molecules.

The lower panel of Figure 4.6 plots the values of $<\Delta\%R_{NP}>$ obtained from single nanoparticle SPRM measurements of the adsorption of 220 nm HNPs onto C11-functionalized gold surfaces in the presence of melittin in solution (red solid circles). The solution concentration of the HNPs was fixed at 30 pM for all of these measurements, and the melittin concentration was varied from zero to 2.5 μM. Above 3 μM, the NIPAm-based HNPs begin to aggregate; this aggregation is evident in DLS measurements[45] and also leads to large standard deviations in the single nanoparticle $\Delta\%R_{NP}$ values (please see the Supporting Information in the Appendix for more details). As seen in the Figure, below 3 μM, the $<\Delta\%R_{NP}>$ values increase linearly with the concentration of melittin. The error bars on the $<\Delta\%R_{NP}>$ values in Figure 4.6 are the 95% confidence intervals; all of these $<\Delta\%R_{NP}>$ values, standard deviations and confidence levels are listed in Table S-1 in the Supporting Information (Appendix A).

Also plotted in the lower panel of Figure 4.6 are the values of $<\Delta\%R_{NP}>$ obtained from single nanoparticle SPRM measurements in the presence of micromolar concentrations of FLAG octapeptide (blue open circles) and BSA (black open diamonds). No change is observed in $<\Delta\%R_{NP}>$ in the presence of either of these molecules. The lack of interaction of the NIPAm-based HNPs with BSA has been shown previously HNPs.[44] These two additional measurements demonstrate the specificity of the melittin uptake into these HNPs.

The upper panel in Figure 4.6 plots the mean hydrodynamic diameters ($<d_{DLS}>$) obtained from separate DLS measurements of the HNPs in micromolar melittin solutions (same concentrations as those used in SPRM measurements). It is clear from the Figure that $<d_{DLS}>$ does not change in the presence of melittin. Using these results, we conclude that the linear increase of $<\Delta\%R_{NP}>$ with melittin concentration observed for the HNPs in the single

nanoparticle SPRM measurements is due to an increase in the refractive index of NIPAm-based HNPs created by the uptake of melittin peptides which replace the lower refractive index PBS.

4.3.5 Quantitation of the Single Nanoparticle SPRM Response with Bulk Solution Loss Fluorescence Measurements

In order to estimate the sensitivity of the single nanoparticle SPRM measurements towards melittin uptake into HNPs, we also performed a set of "solution loss" measurements to roughly measure the average number of melittin molecules absorbed per nanoparticle. In these experiments, the total amount of melittin removed from solution after mixing with HNPs is measured by the decrease in the intrinsic fluorescence of the melittin in solution.[37] The same concentrations of HNPs and melittin that were used in SPRM experiments were also used for these fluorescence experiments, but in a greater total solution volume of 5.0 mL. These measurements require ultracentrifugation to separate the HNPs from the supernatant; in addition, lower concentrations of melittin required a lyophilization and concentration step to detect a quantifiable fluorescence signal. Nevertheless, in these solution loss experiments, a measureable decrease in fluorescence signal was observed, and, from the calculated concentration changes and the total solution volume, the number of moles of melittin removed from the solution by absorption into the HNPs in the bulk measurements could be estimated (please see Supporing Information in the Appendix). Dividing this number by the number of moles of HNPs in these solutions (30 pM x 5.0 mL = 150 fmol) yields an approximate value for the average number of melittin molecules absorbed per HNP. These values are plotted in Figure 4.7 (open blue circles) as a function of melittin concentration along with the $<\Delta\%R_{NP}>$ values from the single

nanoparticle SPRM measurements from Figure 4.6 (filled red circles). Both plots are linear with melittin concentration from zero to 2.5 μM.

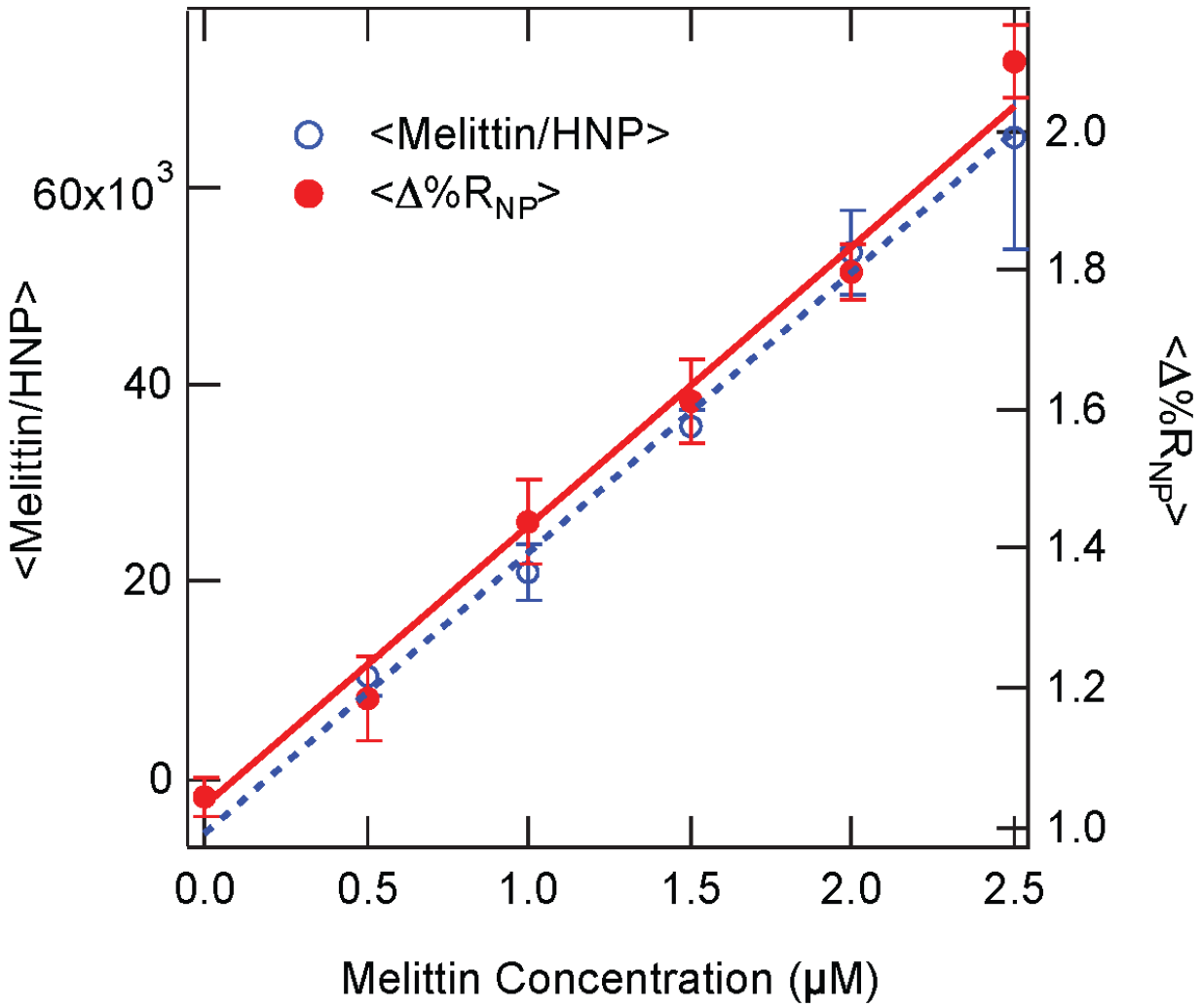

Figure 4.7: Average number of melittin molecules absorbed per HNP as determined from solution loss fluorescence measurements (open blue circles) and $<\Delta\%R_{NP}>$ values from single nanoparticle SPRM measurements (solid red circles) as a function of melittin concentration in solution. The HNP concentration in these measurements was fixed at 30 pM. Using these measurements, a 1% increase in $<\Delta\%R_{NP}>$ corresponds to the loading of 65,000 melittin molecules into each HNP. The lowest detected amount of melittin loading with single nanoparticle SPRM measurements was an increase in $<\Delta\%R_{NP}>$ of 0.15% or approximately 10,000 melittin molecules.

Using the two sets of measurements plotted in Figure 4.7, the sensitivity of the single nanoparticle SPRM response can be quantitated. A 1% increase in $<\Delta\%R_{NP}>$ roughly corresponds to the maximum loading of 65,000 melittin molecules into each 220 nm HNP. If we estimate the volume occupied by a melittin molecule to be 3.445 nm^3,[46] then 65,000 molecules is approximately 4% of the total volume of the 220 nm diameter HNP. Using the molecular weight of melittin (2846.5 g/mol) and the molecular weight of the HNPs estimated from d*n*/d*c* and MALS measurements (1.24×10^9 g/mol), the maximum mass ratio of melittin to polymer observed in these 220 nm HNPs is 15%.

The lowest detected amount of melittin loading observed in the single nanoparticle SPRM measurements is an increase in $<\Delta\%R_{NP}>$ of 0.15% or approximately 10,000 melittin molecules per HNP. This corresponds to 0.6% of the volume of the 220 nm HNP and a melittin/polymer mass ratio of 2.0%. As mentioned above, these bulk solution estimates assume that no melittin is lost to cell walls during ultracentrifugation and lyophilization and that the ultracentrifugation process does not alter the melittin uptake equilibrium. Despite these caveats, the ability to detect the incorporation of 10,000 melittin molecules into a single 220 nm nanoparticle attests to the high sensitivity of these unique SPRM measurements that only rely on the refractive index of the analyte.

4.4 Conclusions and Future Directions

In this chapter, we have demonstrated that quantitative single nanoparticle SPRM measurements can be used to measure *in situ* the uptake of the bioactive peptide melittin into single HNPs. The average single nanoparticle SPRM reflectivity change $<\Delta\%R_{NP}>$ is measured during the adsorption of 220 nm NIPAm-based HNPs onto C11-functionalized gold surfaces from the quantitative analysis of hundreds of single nanoparticle point diffraction patterns in sequential SPRM differential reflectivity images that are collected in real-time during the adsorption process. The value of $<\Delta\%R_{NP}>$ increases linearly with melittin concentrations up to 2.5 μM due to the uptake of peptide molecules into the HNPs that results in an increased nanoparticle refractive index. The SPRM response can be roughly calibrated using bulk fluorescence solution loss measurements; the maximum loading into the 220 nm HNPs that we observe with the single nanoparticle SPRM measurements corresponds to the uptake of approximately 65,000 melittin molecules or 4% of the nanoparticle volume. The minimum change in $<\Delta\%R_{NP}>$ that we detect corresponds to approximately 10,000 melittin molecules, or 0.6% of the nanoparticle volume.

In the future, in addition to quantitating the specific uptake of melittin into the HNPs, these digital SPRM measurements can also be used to study the real-time adsorption of HNPs to bioactive surfaces, and also potentially to monitor melittin release from adsorbed monolayers of HNPs. As our SPRM measurements of single nanoparticle point diffraction patterns improve, we will also begin to examine the single $\Delta\%R_{NP}$ values in order to obtain additional information about the distribution characteristics of single HNPs. These single nanoparticle SPRM measurements are a direct measure of peptide uptake into the soft hydrogel nanoparticle via the refractive index of the molecule and potentially can be applied to the uptake of other peptides,

proteins, and drug molecules into various porous nanoparticles and mesoparticles such as dendrimers, porous silica nanoparticles, and liposomes.

4.5 Acknowledgments

This work was supported by the National Institutes of Health through grant GM059622 (RMC) and the National Science Foundation through grant DMR-1308363 (KJS). The authors thank Dr. Aaron Halpern for guidance and helpful discussions on the use of SPRM and Dr. Kotaro Azuma, Dr. Takashige Kawakami, and the Blumberg group at UC Irvine for use of their ultracentrifuge.

4.6 References

(1) Agarwal, R.; Singh, V.; Jurney, P.; Shi, L.; Sreenivasan, S. V.; Roy, K. *ACS Nano* **2012**, *6*, 2524-2531.

(2) Hamidi, M.; Azadi, A.; Rafiei, P. *Adv. Drug Deliv. Rev.* **2008**, *60*, 1638-1649.

(3) Soppimath, K. S.; Aminabhavi, T. M.; Kulkarni, A. R.; Rudzinski, W. E. *J. Control. Release* **2001**, *70*, 1-20.

(4) Peppas, N. A.; Hilt, J. Z.; Khademhosseini, A.; Langer, R. *Adv. Mater.* **2006**, 18, 1345-1360.

(5) Kabanov, A. V.; Vinogradov, S. V. *Angew. Chem. Int. Ed.* **2009**, *48*, 5418-5429.

(6) Vermonden, T.; Censi, R.; Hennink, W. E. *Chem. Rev.* **2012**, *112*, 2853-2888.

(7) Seliktar, D. *Science* **2012**, 336, 1124-1128.

(8) Kang, H.; Liu, H.; Zhang, X.; Yan, J.; Zhu, Z.; Peng, L.; Yang, H.; Kim, Y.; Tan, W. *Langmuir* **2011**, *27*, 399-408.

(9) Raemdonck, K.; Demeester, J.; De Smedt, S. *Soft Matter* **2009**, *5*, 707-715.

(10) Smith, M. H.; Lyon, L. A. *Acc. Chem. Res.* **2012**, *45*, 985-993.

(11) Nayak, S.; Lyon, L. A. *Angew. Chem. Int. Ed.* **2005**, *44*, 7686-7708.

(12) Hoshino, Y.; Koide, H.; Urakami, T.; Kanazawa, H.; Kodama, T.; Oku, N.; Shea, K. J. *J. Am. Chem. Soc.* **2010**, *132*, 6644-6645.

(13) Hoshino Y, Urakami T, Kodama T, et al. Design of Synthetic Polymer Nanoparticles that Capture and Neutralize a Toxic Peptide. *Small* **2009**, *13*, 1562-1568.

(14) Lee, S. -H; Hoshino, Y.; Randall, A.; Zeng, Z.; Baldi, P.; Doong, R.; Shea, K. J. *J. Am. Chem. Soc.* **2012**, *134*, 15765-15772.

(15) Missirlis, D.; Kawamura, R.; Tirelli, N.; Hubbell, J. A. *Eur. J. Pharm. Sci.* **2006**, *29*, 120-129.

(16) Yoshimatsu, K.; Lesel, B. K.; Yonamine, Y.; Beierle, J. M.; Hoshino, Y.; Shea, K. J. *Angew. Chem. Int. Ed.* **2012**, *51*, 2405-2408.

(17) Soman, N. R.; Lanza, G. M.; Heuser, J. M.; Schlesinger, P. H.; Wickline, S. A. *Nano Lett.* **2008**, *8*, 1131-1136.

(18) Hood, J. L.; Jallouk, A. P.; Campbell, N.; Ratner, L.; Wickline, S. A. *Antivir. Ther.* **2013**, *18*, 95-103.

(19) Ballauff, M.; Lu, Y. *Polymer* **2007**, *48*, 1815-1823.

(20) Karg, M.; Hellweg, T. *Curr. Opin. Colloid Interface Sci.* **2009**, *14*, 438-450.

(21) Griset, A. P.; Walpole, J.; Liu, R.; Gaffey, A.; Colson, Y. L.; Grinstaff, M. W. *J. Am. Chem. Soc.* **2009**, *131*, 2469-2471.

(22) Smith, M. H.; Lyon, L. A. *Macromolecules* **2011**, *44*, 8154-8160.

(23) Cedervall, T.; Lynch, I.; Lindman, S.; Berggard, T.; Thulin, E.; Nilsson, H.; Dawson, K. A.; Linse, S. *Proc. Natl. Acad. Sci. U.S.A.* **2007**, *104*, 2050-2055.

(24) Zybin, A.; Kuritsyn, Y. A.; Gurevich, E. L.; Temchura, V. V.; Uberla, K.; Niemax, K. *Plasmonics* **2010**, *5*, 31-35.

(25) Weichert, F.; Gaspar, M.; Timm, C.; Zybin, A.; Gurevich, E. L.; Engel, M.; Muller, H.; Marwedel, P. *Sens. Actuators, B* **2010**, *151*, 281-290.

(26) Wang, S.; Shan, X.; Patel, U.; Huang, X.; Lu, J.; Li, J.; Tao, N. *Proc. Natl. Acad. Sci. U.S.A.* **2010**, *107*, 16028-16032.

(27) Rothenhausler, B.; Knoll, W. *Nature* **1988**, *332*, 615-617.

(28) Jamil, M. M.; Youseffi, M.; Twigg, P. C.; Britland, S. T.; Liu, S.; See, C. W.; Zhang, J.; Somekh, M. G.; Denyer, M. C. *Sens. Actuators, B* **2008**, *129*, 566-574.

(29) Wang, W.; Foley, K.; Shan, X.; Wang, S.; Eaton, S.; Nagaraj, V. J.; Wiktor, P.; Patel, U.; Tao, N. *Nat. Chem.* **2011**, *3*, 249-255.

(30) Wang, W.; Wang, S.; Liu, Q.; Wu, J.; Tao, N. *Langmuir* **2012**, *28*, 13373-13379.

(31) Giebel, K. -F.; Bechinger, C.; Herminghaus, S.; Riedel, M.; Leiderer, P.; Weiland, U.; Bastmeyer, M. *Biophys. J.* **1999**, *76*, 509-516.

(32) Wang, W.; Tao, N. *Anal. Chem.* **2014**, *86*, 2-14.

(33) Yu, H.; Shan, X.; Wang, S.; Chen, H.; Tao, N. *ACS Nano.* **2014**, *8*, 3427-3433.

(34) Shan, X.; Díez-Pérez, I.; Wang, L.; Wiktor, P.; Gu, Y.; Zhang, L.; Wang, W.; Lu, J.; Wang, S.; Gong, Q.; Li, J.; Tao, N. *Nat. Nanotechnol.* **2012**, *7*, 668-672.

(35) Halpern, A. R.; Wood, J. B.; Wang, Y.; Corn, R. M. *ACS Nano* **2014**, *8*, 1022-1030.

(36) Debord, J. D.; Lyon, L. A. *Langmuir* **2003**, *19*, 7662-7664.

(37) Raghuraman, H.; Chattopadhyay, A. *Biophys. J*. **2004**, *87*, 2419–2432.

(38) Bae, Y.H.; Okano, T.; Kim, S.W. *J. Polym. Sci. Part B Polym. Phys*. **1990**, *28*, 923-936.

(39) Matsuzaki, K.; Yoneyama, S.; Miyajima, K. *Biophys. J*. **1997**, *73*, 831-838.

(40) Glättli, A.; Chandrasekhar, I.; Gunsteren, W. F.; *Eur. Biophys. J.* **2006**, *35*, 255-267.

(41) Chen, Y.; Nguyen, A.; Niu, L.; Corn, R.M. *Langmuir* **2009**, *25*, 5054-5060.

(42) Nelson, B.P.; Grimsrud, T.E.; Liles, M.R.; Goodman, R.M.; Corn, R.M. *Anal. Chem.* **2001**, *73*, 1-7.

(43) Guedon, P.; Livache, T.; Martin, F.; Lesbre, F.; Roget, A.; Bidan, G.; Levy, Y. *Anal. Chem.* **2000**, *72*, 6003-6009.

(44) Hoshino, Y.; Koide, H.; Furuya, K.; Haberaecker, W. W.; Lee, S. -H.; Kodama, T.; Kanazawa, H.; Oku, N.; Shea, K. J. *Proc. Natl. Acad. Sci. U.S.A.* **2012**, *109*, 33-38.

(45) Driskell, J.D.; Jones, C.A.; Tompkins, S.M.; Tripp, R.A. *Analyst* **2011**, *136*, 3083-3090.

(46) Center for Biotechnology, Northwestern University. Peptide Properties Calculator. http://www.basic.northwestern.edu/biotools/proteincalc.html (accessed Feb. 20, 2015).

Appendix A

Supporting Information for Chapter 4: Measuring Melittin Uptake into Hydrogel Nanoparticles with Near-Infrared Single Nanoparticle Surface Plasmon Resonance Microscopy

A.1 DLS Analysis of Synthesized Hydrogel Nanoparticles

The mean hydrodynamic diameter of the hydrogel nanoparticles (HNPs) as measured by dynamic light scattering (DLS, measured by Zetasizer Nano ZS at 25 °C) was 220 nm in PBS. As detailed in the main text, the monomer feed ratios of the HNPs were 5 mol% AAc, 40 mol% TBAm, 2 mol% BIS, 53 mol% NIPAm. 2.5 mg/50 mL of SDS was used for the synthesis. The HNP synthesis yield was 89%

A.2 d*n*/d*c* and MALS Measurements to Determine Mean HNP Molar Mass

To determine the refractive index increment (d*n*/d*c*) value of hydrogel particles, differential refractive indexes of aqueous solutions containing 15.6, 31.3, 62.5, 125, 250, and 500 μg/mL of hydrogel particles were measured by using Optilab rEX equipped with a syringe pump. Multi-angle light scattering (MALS) of aqueous solutions containing 1.60, 2.40, 3.60, 5.40, 7.20, 9.60, and 12.8 μg/mL of hydrogel particles were measured by using DAWN HELEOS equipped with a syringe pump. Both differential refractive index and multi-angle light scattering measurements were performed under a flow condition (0.38 mL min^{-1}). Data collection and subsequent data analysis were performed by using the Astra software Version 5.3.4.20 (Wyatt Technology Corporation, Santa Barbara, CA). The principles employed in multi-angle light scattering date analysis have been described in detail elsewhere.[1]

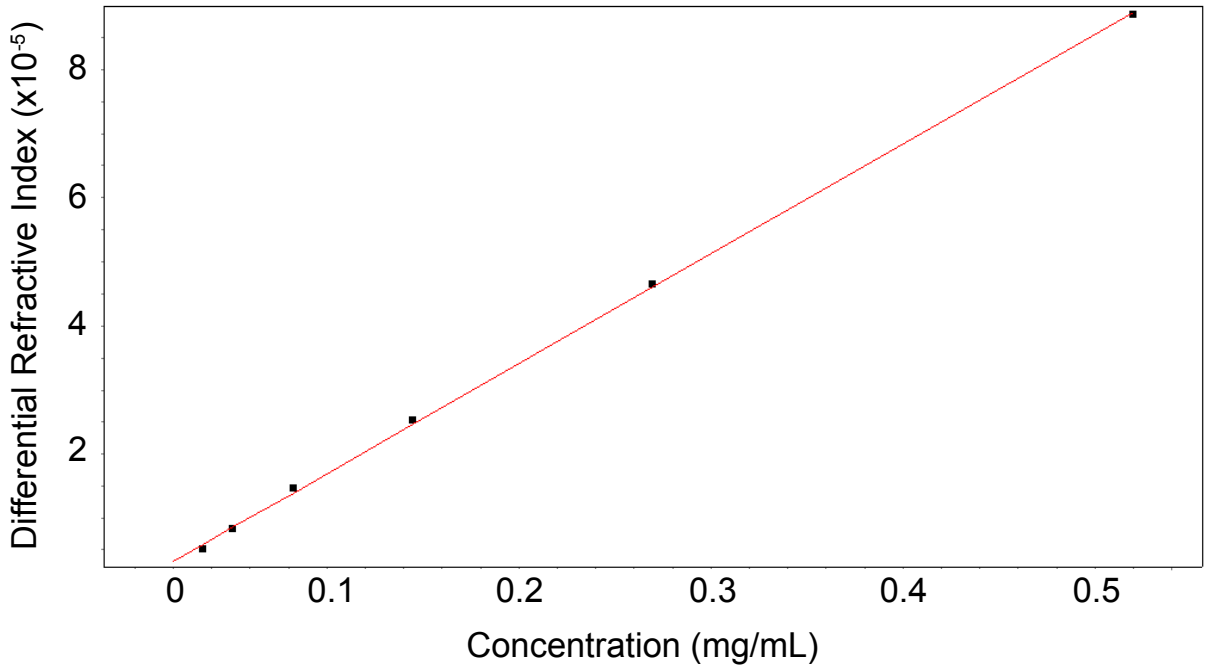

Figure A.1: d*n*/d*c* determination from differential refractive index measurements.

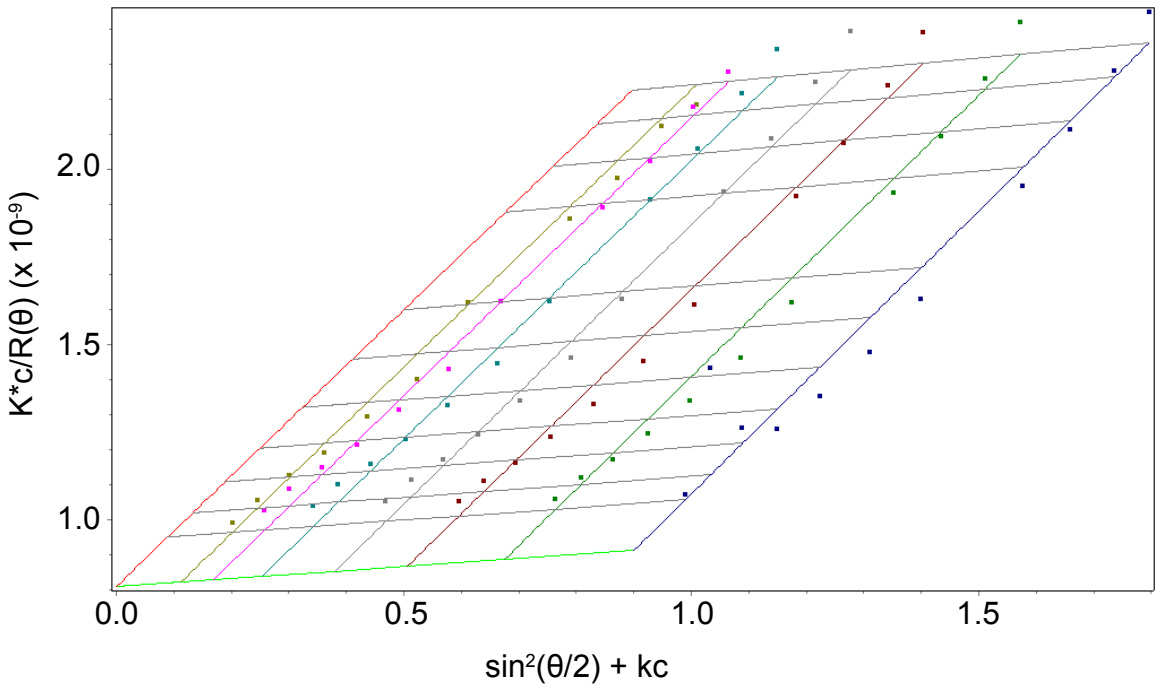

Figure A.2 Zimm plot generated from HNP concentrations noted above.

Results of static light scattering experiments:

Refractive index increment (dn/dc): 0.1714 ± 0.0016 mL g^{-1}

Radius of gyration (R_g): 95.2 ± 2.0 nm

Second Virial Coefficient (A_2): $(4.020 \pm 1.756) \times 10^{-6}$ mol mL g^{-2}

Molar mass (MW): $(1.235 \pm 0.038) \times 10^{9}$ g mol^{-1}

A.3 Tabulated Average Single Nanoparticle SPRM Reflectivity Change $<\Delta\%R_{NP}>$

Table A.1. SPRM response to melittin loading.

Melittin concentration (μM)	**$<\Delta\%R_{NP}>$**	**Standard deviation (Δ%R)**	**95% Confidence interval (Δ%R)**	**N**
0	1.04	0.30	0.03	443
0.5	1.19	0.52	0.06	314
1.0	1.44	0.50	0.06	304
1.5	1.61	0.52	0.06	300
2.0	1.80	0.41	0.04	392
2.5	2.10	0.50	0.05	355

A.4 Fluorescence Measurements

The intrinsic fluorescence of melittin due to its sole tryptophan residue has been documented previously.[2,3] Samples were excited at 280 nm and their fluorescence emission measured at 349 nm. Measured fluorescence values were converted to concentration from standard curves generated from melittin solutions of varying concentrations in PBS.

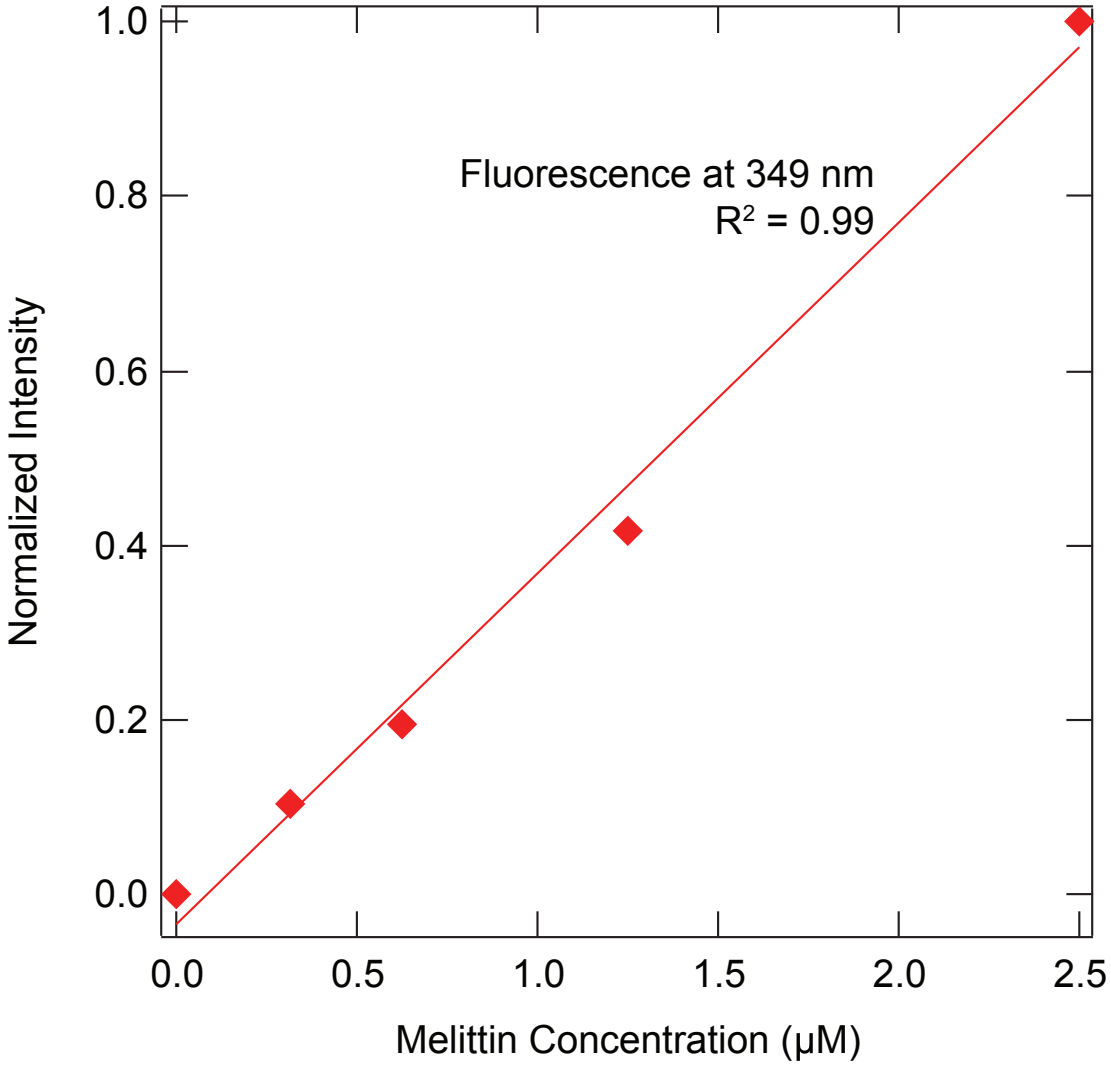

Figure A.3: Melittin fluorescence standard curve for measured emission at 349 nm.

Table A.2. Fluorescence Characterization of Melittin Uptake by HNPs

Concentration (μM)	Concentration Measured by Fluorescence (μM)		Melittin Absorbed by HNPs (%)	Melittin Molecules/HNP
	With HNPs	Without HNPs		
0	0.05 ± 0.08	0.05 ± 0.09	n/a	n/a
0.5	0.18 ± 0.01	0.46 ± 0.06	62	10,000
1	0.27 ± 0.03	0.72 ± 0.08	63	21,000
1.5	0.46 ± 0.01	1.60 ± 0.05	71	36,000
2	0.42 ± 0.02	2.14 ± 0.13	80	53,000
2.5	0.54 ± 0.06	2.48 ± 0.33	78	65,000

The moles of melittin (from the initial concentration and the percentage of melittin absorbed as measured by fluorescence) and moles of HNPs (from 30 pM) in the ultracentrifuged volume of 5 mL were first calculated (e.g., at 2.5 μM melittin, 78% of melittin was absorbed by HNPs; 0.78 x 2.5 μM x 5 mL = 9.75 nmol melittin; 30 pM HNPs x 5 mL = 150 fmol HNP). Their molar ratio is the estimated melittin molecules/HNP that is reported.

A.5 HNP Aggregation at High Melittin Concentrations Observed by SPRM

For melittin concentrations up to 2.5 μM, we see a linear increase in $<\Delta\%R_{NP}>$ proportional to peptide concentration. When HNPs are mixed into higher concentrations of melittin, we see evidence of HNP aggregation in very large diffraction features with large $\Delta\%R_{NP}$ values ($\Delta\%R_{NP} > 4\%$). This aggregation is likely the due to charge neutralization of the HNPs by melittin. As a result of these aggregates, the standard deviation of the $\Delta\%R_{NP}$ distribution increases significantly. For example, a solution of 5.4 μM melittin and 30 pM HNPs results in a $\Delta\%R_{NP}$ distribution with a standard deviation of 1%, as seen in Figure S-5. This observation is corroborated by DLS, which also detects the presence of aggregates, but analysis by SPRM gives deeper insight into the nature of this aggregation. For example, for the 5.4 μM melittin solution mentioned above, roughly 6% of the signal observed were greater than 4% in $\Delta\%R_{NP}$ and deemed as aggregates. We are also able to visualize and track in real time the formation of HNP aggregates as they adsorb onto the surface.

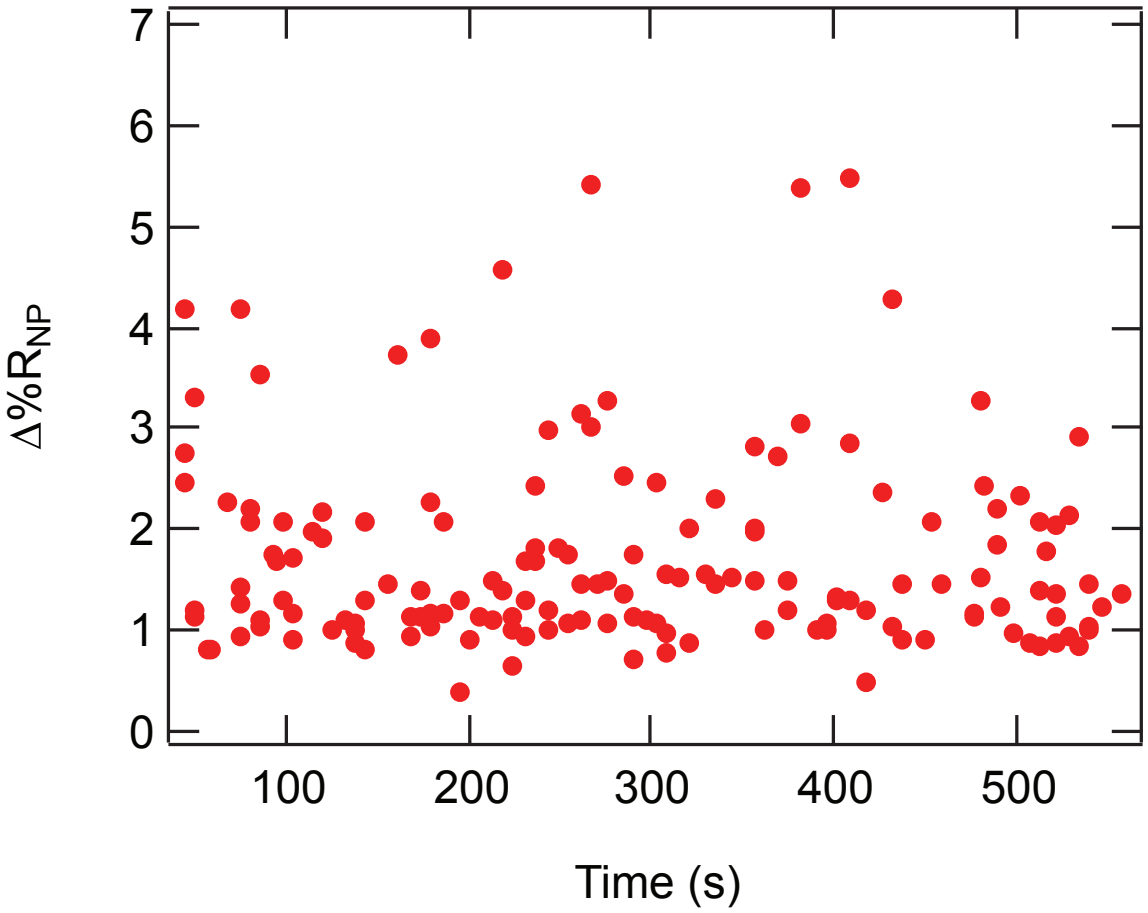

Figure A.4: $\Delta\%R_{NP}$ distributions over time for a solution containing 5.4 μM melittin and 30 pM HNPs in PBS. HNP aggregates appeared as very large signals ($\Delta\%R_{NP} > 4\%$) and made up ~6% of the all $\Delta\%R_{NP}$ calculated. The standard deviation of the $\Delta\%R_{NP}$ distribution increased to 1% for this experiment, which is much larger than without HNP aggregation. HNP aggregation was also detected by DLS.

A.6 Supporting Information References:

(1) Andersson, M.; Wittgren, B.; Wahlund, K.-G. *Anal. Chem.* **2003**, *75*, 4279.

(2) Raghuraman, H.; Chattopadhyay, A. *Biophys. J*. **2004**, *87*, 2419–2432.

(3) Tran, C.D.; Beddard, G.S. *Eur. Biophys. J*. **1985**, *13*, 59-64.